P-13-46

Äspö Task Force on modelling of groundwater flow and transport of solutes

Task 7 – Groundwater flow and transport modelling of fracture system at regional, block, and single-fracture scale flow and transport, Olkiluoto

Atsushi Sawada, Hiromitsu Saegusa, Shinji Takeuchi,
Japan Atomic Energy Agency

Kazuhiko Sakamoto, Inspection Development Company Ltd.

William S. Dershowitz, Golder Associates Inc.

December 2015

Svensk Kärnbränslehantering AB
Swedish Nuclear Fuel
and Waste Management Co

Box 250, SE-101 24 Stockholm
Phone +46 8 459 84 00

ISSN 1651-4416
SKB P-13-46
ID 1413260
December 2015

Äspö Task Force on modelling of groundwater flow and transport of solutes

Task 7 – Groundwater flow and transport modelling of fracture system at regional, block, and single-fracture scale flow and transport, Olkiluoto

Atsushi Sawada, Hiromitsu Saegusa, Shinji Takeuchi,
Japan Atomic Energy Agency

Kazuhiko Sakamoto, Inspection Development Company Ltd.

William S. Dershowitz, Golder Associates Inc.

This report concerns a study which was conducted for Svensk Kärnbränslehantering AB (SKB). The conclusions and viewpoints presented in the report are those of the authors. SKB may draw modified conclusions, based on additional literature sources and/or expert opinions.

Data in SKB's database can be changed for different reasons. Minor changes in SKB's database will not necessarily result in a revised report. Data revisions may also be presented as supplements, available at www.skb.se.

A pdf version of this document can be downloaded from www.skb.se.

© 2015 Svensk Kärnbränslehantering AB

Abstract

This report summarises the progresses of Äspö Task Force on Groundwater Flow and Transport of Solutes "Task 7" groundwater flow and transport modelling studies. The task force also proposes, reviews, evaluates and contributes to specific experimental methodologies for investigation of the site. Since the task force has organised in 1991, six major subjects, Task 1 through Task 6, have been studied; these tasks have mainly focused on the experiments at or around the Äspö Hard Rock Laboratory (HRL). Japan Atomic Energy Agency (JAEA) has participated in this task force, to contribute to JAEA's mission to provide a technical basis for repository site characterization, safety assessment, and regulation in Japan.

The specified "Task 7" concerns the uncertainties of the hydrogeological model developed from the Olikiluoto site characterization dataset, and aims to provide a bridge between the information derived from site characterisation (SC) and performance assessment (PA). Task 7 has a specific object: how information from the new flow-logging tools (so-called POSIVA Flow Log: PFL) can be used to maximum benefit, to reduce key uncertainties for modelling hydrogeological structure, and PA relevant groundwater flow behaviour.

The overall strategy of Task 7 is to progress from the large scale (Olkiluoto site-scale with focus on regional scale of fracture zones) to the much smaller scale, that of the tunnel scale of the host rock. At each scale, specific goals are defined within the context of the overall Task 7 goal, and modelling tasks are defined to support those goals:

- Task 7A considers a region of approximately 20 km^2 on Olkiluoto Island, focusing on the detailed area around the deep borehole KR24, which was drilled from the ground surface. In addition to constraints provided by steady-state PFL measurements at KR24 and surrounding boreholes, transient measures also constrain the model. These include pressure drawdown and PFL measurements during a long-term pumping test at KR24.
- Task 7B considers a localized near-field scale (50 m by 50 m by 50 m) volume within an approximately 500 m by 500 m region surrounding boreholes KR14–18 at the Olkiluoto site. Specific pressure response and flow response data measured during a series of pressure interference tests are applied to constrain the model.
- Task 7C focused on single fractures, intersected by the shafts at ONKALO in Olkiluoto site. Other constraints for the model include PFL flow data during interference tests at the pilot boreholes along the shafts (measured before excavating the shafts), and inflow distribution to the shaft wall measured by "Nappy tests".

Task 7 studies were very useful for advancing the concept of hydrostructural modelling. They were also useful for demonstrating the power of steady-state and transient hydraulic data to improve and condition the geometry and properties of water conducting structure at each modelling scale. Key hydraulic data constraining the hydrostructural model were PFL measurements from steady state and transient (pumping interference tests) phases. The main conclusions are listed below:

- Task 7A: Uncertainty of transmissivity values of regional scale (several kilometres) of fault zones were examined by comparing with steady state PFL data and pressure / flow response during pumping phase. The results indicate that the major response can be reproduced by models constrained by PFL data, although the opening borehole for measuring PFL has a disadvantage for homogenising head values along the borehole. In order to constrain both major fault zones and minor water conducting features, an advanced method discriminating major pressure or flow response zones from other minor zones during the PFL investigations might be required. This discrimination should be consistent with conceptualisation of the hydrogeological model of major fault zones at the study area.
- Task 7B: Major pressure and flow response could be reproduced by the conceptualisation of major water conducting features (fault zones: several hundred metres scale) based on the derivative plot analysis of transient pressure interference test data. The unified value, residual sum of square (RSS), for evaluating model plausibility in the comparison between measured and

simulated values could be useful for checking reproducibility of major flowing zones (pressure and flow respond zone), but would be limited in reproducing minor zone flow behaviour.

- Task 7C: In-plane heterogeneous fracture roughness structure and / or aperture distribution model was examined by comparing with flow response measured by PFL at the pilot boreholes drilled along shaft walls before excavating the shafts. Average transmissivity evaluated by standard PFL data could constrain flow behaviour to reproduce most of PFL flow response data measured at pilot boreholes. However, PFL flow response data could not fully constrain small scale structure in a single fracture affected by various scale of geological structures, varying from several millimetres to several metres. The small scale structure might strongly control transport behaviour in a fracture, judging from a sensitivity study by varying spatial resolution of heterogeneous model in a single fracture.

Contents

1 Introduction and objectives

1.1 Background

The Äspö Task Force on modelling of groundwater flow and transport of solutes is an organization supporting the modelling and development of evaluation methodology for models of groundwater flow and solute transport in fractured rock. The task force also proposes, reviews, evaluates and contributes to specific experimental methodologies for investigation of the site. Since the task force was first formed in 1991, six major subjects, Task 1 through Task 6, have been studied (ex. Hodgkinson 2007). These tasks mainly focus on experiments at/around the Äspö Hard Rock Laboratory (HRL).

Japan Atomic Energy Agency (JAEA) has participated in this task force, to contribute to JAEA's mission of providing a technical basis for repository site characterisation, safety assessment, and regulation of repository in Japan.

Task 7 concerns a hydrogeological model at the Olikiluoto site, using a characterization dataset focusing on new flow-logging tools (POSIVA Flow Log: PFL; Öhberg and Rouhiainen 2000), conducted by Posiva. This report summarises the evaluation results through the hydrogeological modelling and simulation conducted by JAEA.

1.2 Scope and objectives of Task 7

Task 7 aims to provide a bridge between the information derived from site characterisation (SC) and performance assessment (PA). Task 7 has a specific object: determine how information from the new flow-logging tools (i.e., PFL) can be used to maximum benefit, to reduce key uncertainties for modelling hydrogeological structure and PA-relevant groundwater flow behaviour.

The overall strategy of Task 7 is to progress from the large scale (i.e., the site-scale of Olkiluoto with focus on regional-scale fracture zones) to the much smaller scale (i.e., the tunnel scale of the host rock). At each scale, specific goals are defined within the context of the overall Task 7 goal, and modelling tasks were defined to support those goals (Vidstrand et al. 2012):

- Task 7A considers a region of approximately 20 km^2 on Olkiluoto Island, focusing on the detailed area around the deep borehole KR24, which was drilled from the ground surface. Both steady-state PFL measurements at KR24 and surrounding boreholes, and transient pressure drawdown and change of PFL measures during a long-term pumping test at KR24 are included in the Task 7A dataset.
- Task 7B considers a localized near-field scale (50 m by 50 m by 50 m) volume within an approximately 500 m by 500 m region surrounding boreholes KR14–18 at the Olkiluoto site. Specific data of pressure response and flow response during a series of pressure interference tests are applied to constrain the model.
- Task 7C focused on single fractures, intersected by the shafts at ONKALO in Olkiluoto site. Other constraints for the model include PFL flow data during interference tests at the pilot boreholes along the shafts (measured before excavating the shafts), and inflow distribution to the shaft wall measured by "Nappy tests".

2 Task Specifications

2.1 Task 7A – Regional scale

The aim and scope of Task 7A is to simulate the performance of the groundwater system and its response to long-term pumping in the presence of open and sealed-off boreholes. The task involves building numerical groundwater flow models of the Olkiluoto Island site (Figure 2-1) and testing their robustness. An important aspect of the data from the site is the use of the PFL to measure flow into/out of the boreholes during both "undisturbed" and pumped conditions.

The hydrostructural model and reference dataset are provided by the task specification (Vidstrand et al. 2012). It also suggests the options for the boundary conditions, modelling surface layer, modelling boreholes, etc. The main modelling and simulation target is the KR24 pumping test. KR24 was drilled as one of pilot boreholes of the ONKALO shaft (KU1). The pumping from KR24 was conducted for about two months (Vaittinen and Ahokas 2005) and pressure drawdown and flow responses were observed at the existing boreholes around KR24, with PFL under the open borehole conditions. The models constructed based on the task specification (Vidstrand et al. 2012) are evaluated and calibrated by comparing with the measured head values and/or inflow distribution along the boreholes, through the following simulation procedure:

1. Steady state flow simulations without borehole and pumping.
2. Steady state flow simulations with open boreholes, which are free to cross-flow.
3. Steady state and transient flow simulation for KR24 pumping without other boreholes.
4. Steady state and transient flow simulation for KR24 pumping with monitoring of open boreholes.

Once developed, the model is applied to quantify uncertainty on the advective travel time from reference points in borehole KR24 through the fracture zones to a discharge point (or model boundary). The simulations should be conducted under assumed PA-relevant boundary conditions: steady state condition without any disturbance of boreholes, pumping and excavation of tunnels and/or shaft.

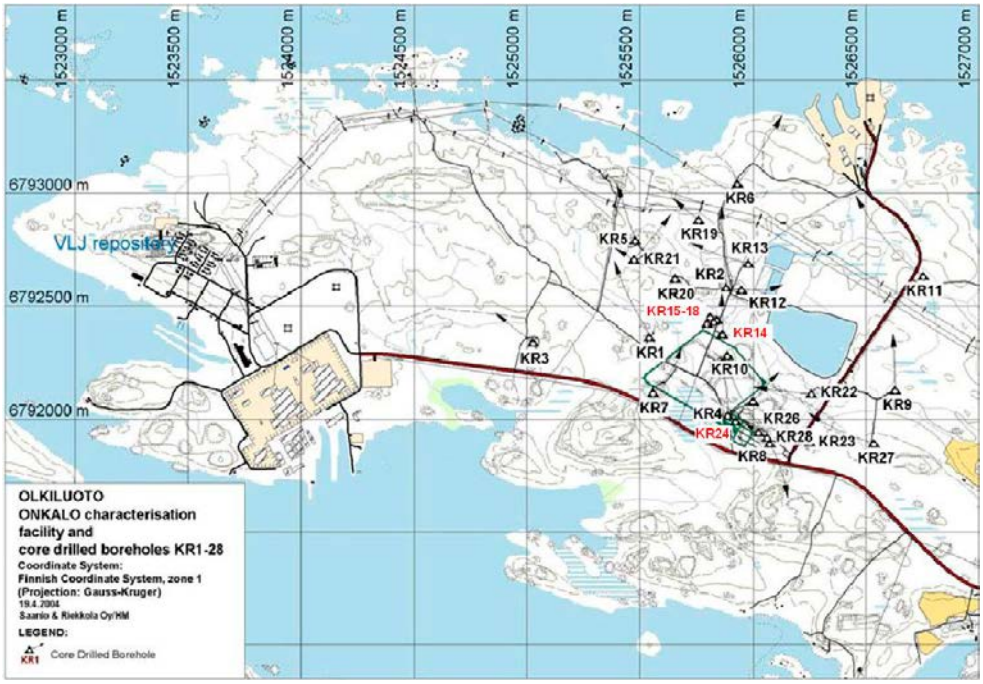

Figure 2-1. *The island of Olkiluoto showing the location of boreholes KR1–KR28 and the ONKALO facility.*

The results are given as statistical values, such as mean values for the calculated travel time and travel length, together with justification of the bounds and discussion of key uncertainties associated with the calculations.

2.2 Task 7B – Block scale

The aim and scope of Task 7B is to simulate the performance of the groundwater system, by building and testing the sensitivity of numerical groundwater flow models of the KR14–18 region of the Olkiluoto site (Figure 2-1, 2-2). An important aspect of the data from the site is the use of the PFL to measure flow into/out of the boreholes during both "undisturbed" and pumped conditions. Another important aspect is the possibility of comparing this kind of "flow response" data to "pressure response" data (see Figure 2-3) in the same boreholes. The hydrostructural models and reference dataset are provided by the task specification (Vidstrand et al. 2012), which specifies detailed conceptualisation and modelling procedures, and also suggests alternatives for the hydrogeological model, boundary conditions, modelling boreholes, etc. Boundary conditions over a block scale volume plausibly bounded by structure HZ19A or the surface and structure HZ20A should be derived. Background fractures in the model region including structure HZ19C from Task 7A (that is structure HZ19C is part of the background fractures in this sub-task) is estimated from a dataset of water conducting features measure by PFL at single borehole information, fracture logging, and generic correlations. HZ19C has generally been treated as a homogenous and extensive major feature in Task 7A. Within Task 7B, HZ19C may need to be treated as a patchy "minor feature" or be limited in size or connectivity to explain the observed drawdown during the KR14 pumping test. The models that are constructed based on the task specification (Vidstrand et al. 2012) should be used during the following analyses:

1. Model evaluations and calibrations based on comparing with head values and PFL flow distribution along the boreholes, under the natural conditions (without pumping).
2. Model evaluations and calibrations based on comparing with pressure response and flow response, under the pumping conditions (e.g., interference tests among KR14–18 boreholes).

To meet the task goal of providing support for both site characterization and safety assessment, the study also attempted to determine how well safety related indicators such as "f-factor" (SKB 2011), along the pathways from specified points in the model region under the natural condition can be constrained.

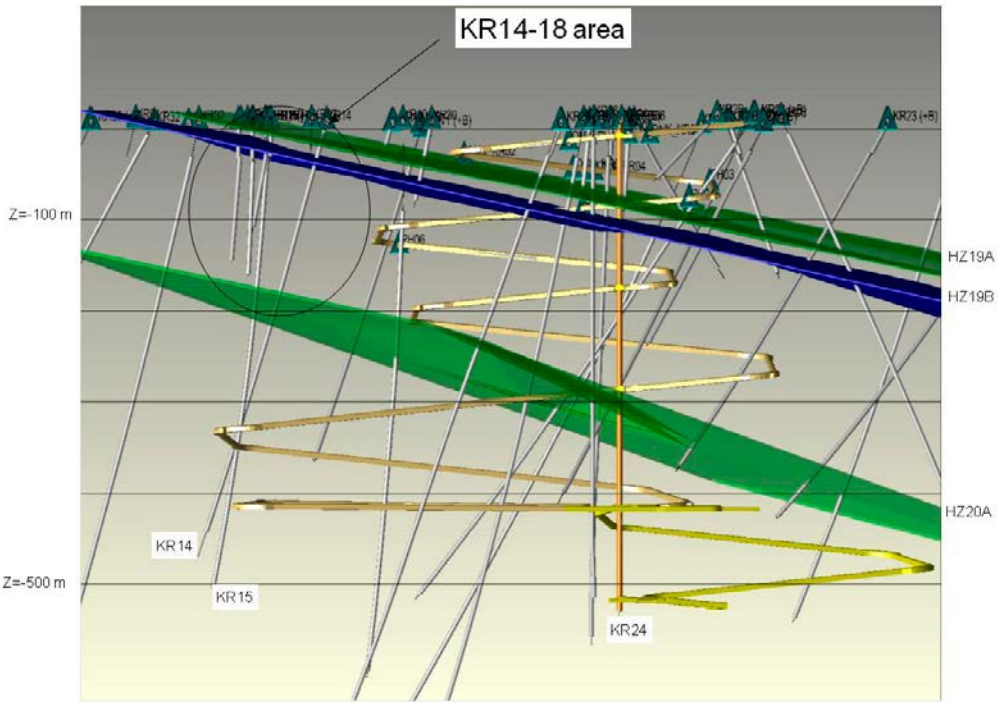

Figure 2-2. *The cross-sectional image KR14 – KR18 boreholes at the ONKALO area.*

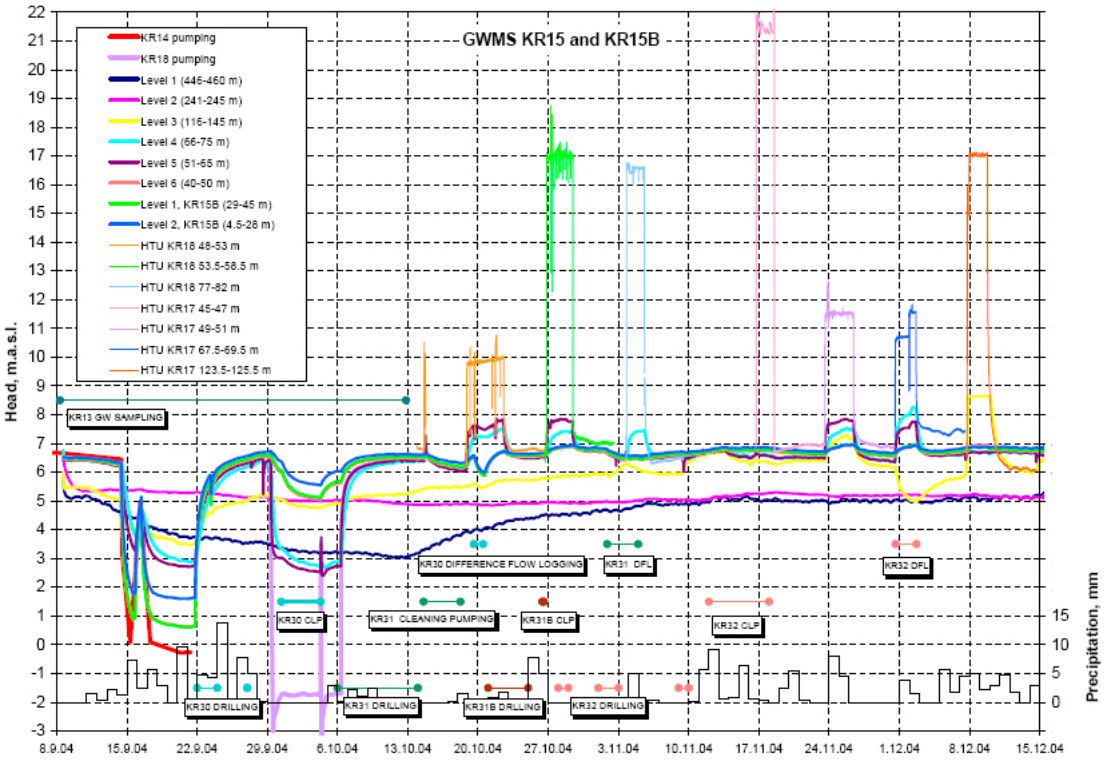

Figure 2-3. *Illustration of results of the KR14-18 pressure interference tests.*

2.3 Task 7C – Single-fracture scale

Task 7C focuses on single fractures, based on single-fracture characteristics from the characterisation of the shafts, KU1 along KR24 borehole, KU2 along KR38 borehole and KU3 along KR48 (Figure 2-4), which are excavated by raise-bore from a –290 m level at the ONKALO tunnel (Vidstrand et al. 2012). The three fractures were selected because they represent a class of low transmissivity fractures that are important for performance assessment, yet have only limited characterization using conventional hydrogeological test methods. The Task 7C fractures are estimated to have transmissivity values of approximately $1 \cdot 10^{-9}$, $1 \cdot 10^{-10}$, and $1 \cdot 10^{-11}$ m^2/s.

The intention is to develop a single-fracture scale model near the drift incorporating essential microstructural information in order to better understand flow and transport pathways. By matching the measured flow pattern on a section of shaft wall, it is hoped that the task will improve assessment of transport characteristics such as the f-factor predictions and the flow wetted surface area. The task is not focused specifically on understanding the effects of the shaft wall excavation damage zone (EDZ) and unsaturated conditions, nor effects due to the grouting of investigation boreholes. Consequently, the three fractures selected were chosen in the region that is considered least disturbed by grouting and construction.

The three fractures are characterized by borehole investigations (including PFL and hydraulic testing) and shaft mapping. These data include information that can be processed in a number of ways to build a microstructural model for fracture roughness and aperture distributions. Task 7C is intended to provide advances in the characterisation and understanding of flow in low-transmissivity single fractures, with particular emphasis on patterns of aperture, including fracture minerals and infillings, channelling, and fracture intersection effects. The hydrogeological modelling procedure should be developed and be justified for parameterising the microstructural model of the three fractures. It is anticipated that this will include the use of generic approaches based on roughness and aperture studies at other sites, as well as access to the database for the fractures in particular.

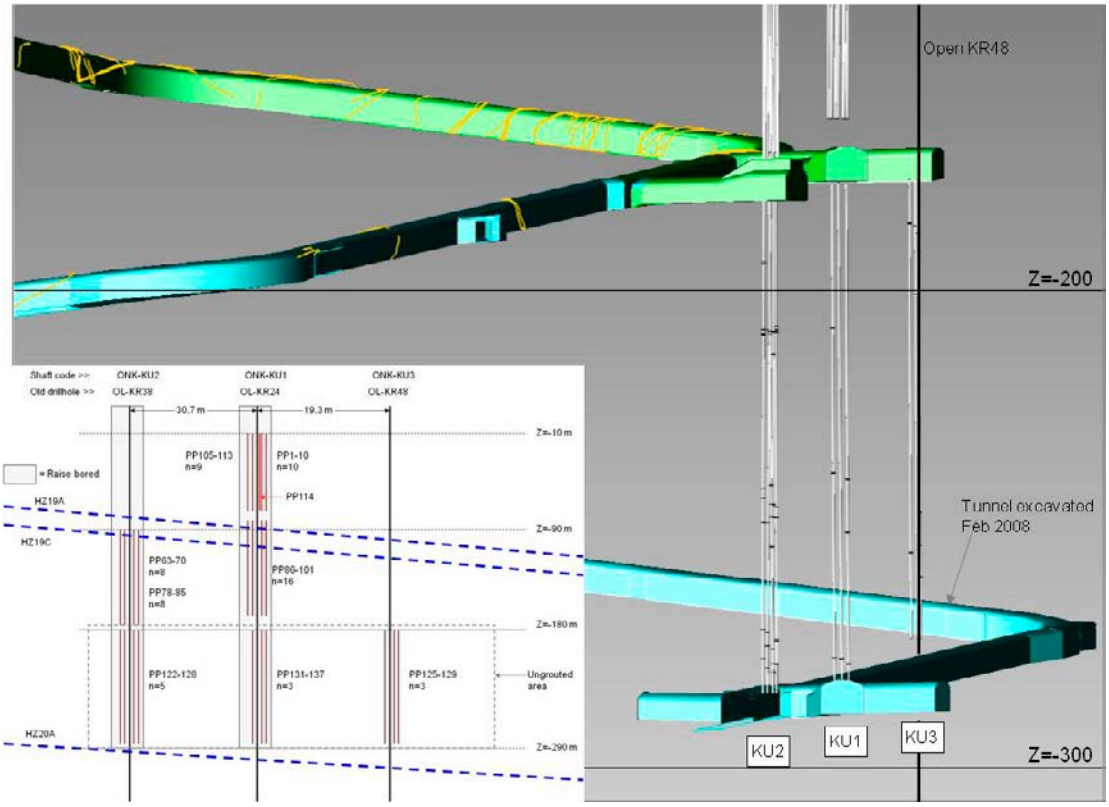

Figure 2-4. *Conceptual illustration of borehole layout around the shafts KU1, KU2, and KU3, in Task 7C study area.*

The models constructed based on the task specification (Vidstrand et al. 2012) should be used in the following model simulations:

1. Model evaluations comparing 11 single borehole PFL representations, and 12 special PFL tests with adjacent open holes (“cross-hole” PFL).
2. F-factor calculations.

The f-factor should be calculated for each defined single-fracture model for a natural gradient of 0.1 in two orthogonal directions (north-south and east-west). Starting and ending points for each location should be at the location of the shaft wall.

Task 7C also includes an optional task for simulating inflow distribution to the excavated shaft walls. The groundwater inflow distribution was measured by “Nappy tests”, measured by placing nappies on these fractures where they intersect the shaft wall. This experiment is complicated by mechanical disturbance, boundary condition, and multiphase flow effects, but it is hoped that the use of nappies to collect inflow is sufficiently robust to provide a usable measure of the inflow, and the spatial pattern of inflow.

3 Model descriptions

3.1 Task 7A – Regional scale

3.1.1 Modelling approach

The primary assumptions for modelling Task 7A hydrogeological structure are as follows. The model concepts are summarised in Figure 3-1.

1. Fracture zones are assumed to be represented by tessellated, homogenous, non-planar zones, according to the geometric specification (Vidstrand et al. 2012). Although it is understood that fracture zones are heterogeneous in thickness, permeability, and porosity, an unique value of transmissivity was used for each fracture zone. Fracture zones were tessellated to a triangular mesh of scale 20 to 100 metres (m).
2. Surface topography (Figure 3-2) was decimated to a 20 m scale triangulated surface, covering both the island of Olkiluoto and the portion of the sea floor within the model region.
3. Surface layers were represented by a grid of 20 m scale block elements, which was modelled by equivalent porous medium (EPM). This mesh conforms to the 20 m mesh at the surface, and extends to Elevation – 70 m under both Olkiluoto and the Baltic Sea. The mesh was modelled as EPM at a grid discretization of 20 m × 20 m × ~20 m (Figure 3-1).
4. The block element was discretized to tetrahedral mesh for finite element flow and particle tracking calculations in MAFIC (Miller et al. 2001).
5. Vadose zone flow (between the topographic surface and the groundwater table) is assumed to occur according to assumptions of Bear (1972). A vertical gradient of one is assumed in the vadose zone.
6. Open boreholes and packed off sections of monitoring boreholes are represented by a "group flux" boundary condition, in which flow is allowed to occur through the well to obtain a single steady-state head throughout the well, with a net flow out of the well of zero (see Figure 3-4).
7. All fluids are assumed to be fresh water, with a constant density of 1 g/cc and a temperature of 20°C. The effect of the freshwater-saltwater interface and variations in water density and temperatures (particularly near the Baltic Sea) was ignored in this modelling.
8. Aperture values are not used for groundwater flow calculations, since each fracture zone is assigned a value of transmissivity T (m^2/s). However, for solute transport calculations, the transport aperture e_t is needed to determine the advective velocity. These values are calculated from transmissivity using the empirical equation $e_t = a\ T^b$, where a=0.5, and b=0.5 (Vidstrand et al. 2012).

3.1.2 Data usage and interpretation

The Olkiluoto hydrostructural model was constructed based on the Task 7A specification (Vidstrand et al. 2012). The fault zone structure, specified by CAD format (SmallFace4.dxf and LargeFace4.dxf) was represented by the discrete fracture network (DFN) approach (see also Figure 3-1 and 3-3). Surface topography was also modelled by using provided surface topography data. Transmissivity and hydraulic conductivity of the modelled structure, the DFN model and the surface layer EPM model, respectively, were set by specified value (Vidstrand et al. 2012).

3.1.3 Geometrical description

The horizontal extent of the modelling region is about 6 km by 4 km as shown in Figure 3-2. The vertical extent is from the ground surface of Olkiluoto and the surface of the Baltic Sea down to 1,000 m below ground surface (bgs). The structure of the fault zone was modelled by using CAD format files as provided and was discretized to a triangular mesh according to the specifications required by the finite element flow program MAFIC (Miller et al. 2001), a component of FracMan. The surface extent of the fault zones was truncated by the bottom of the surface layer EPM. As a consequence, any preferential transport pathways which include fault zones discharge to the base of the EPM layer, and then travel through the EPM according to the EPM cell properties.

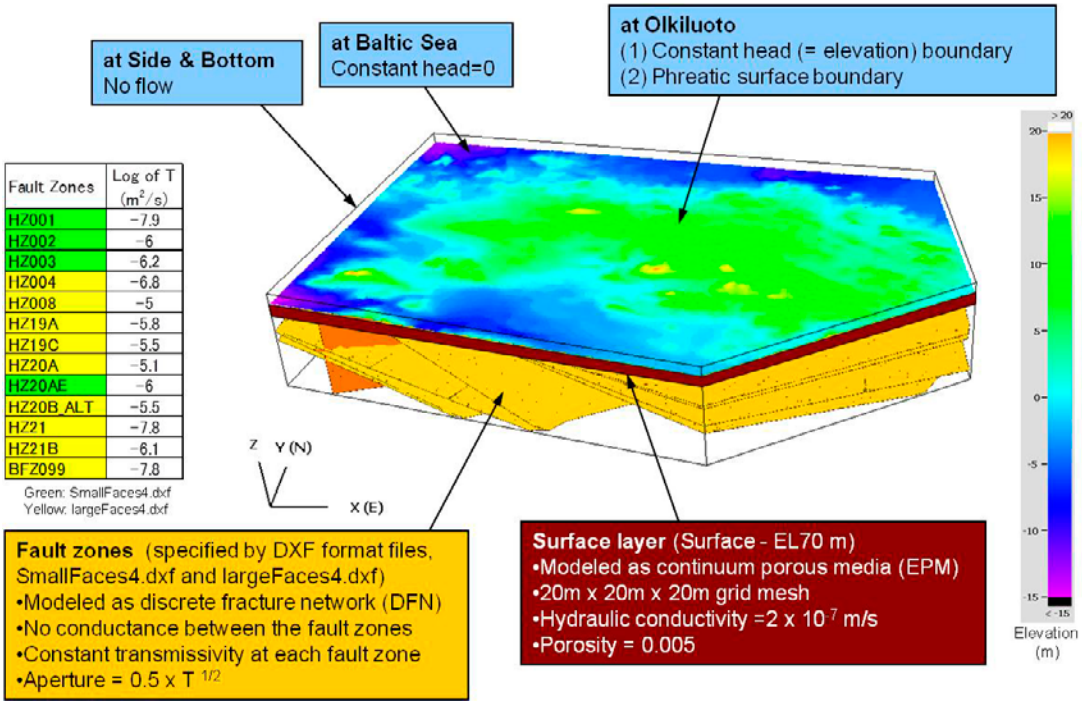

Figure 3-1. *Summary of Task 7A modelling concepts.*

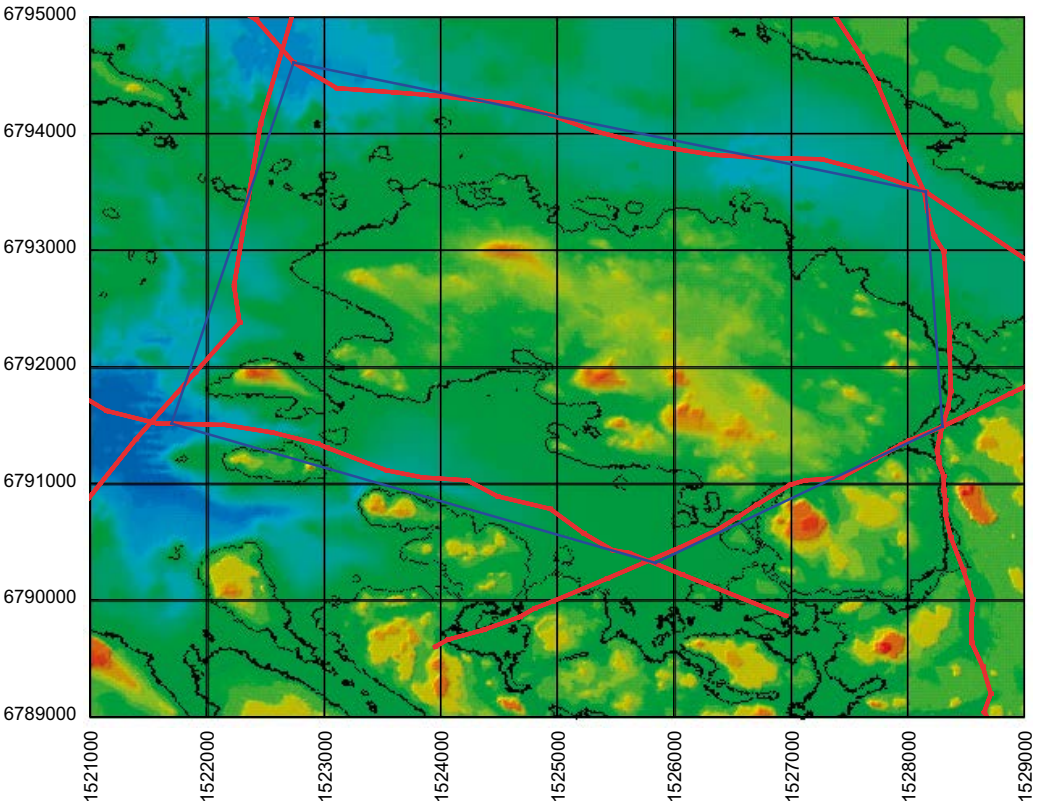

Figure 3-2. *Horizontal spatial extent of the model. X and Y axis are the specified coordinate system in meters. Red line: regional scale of fault zone defined by Task 7A specification. Blue line: simplified pentagon shape of boundary used in Task 7A model.*

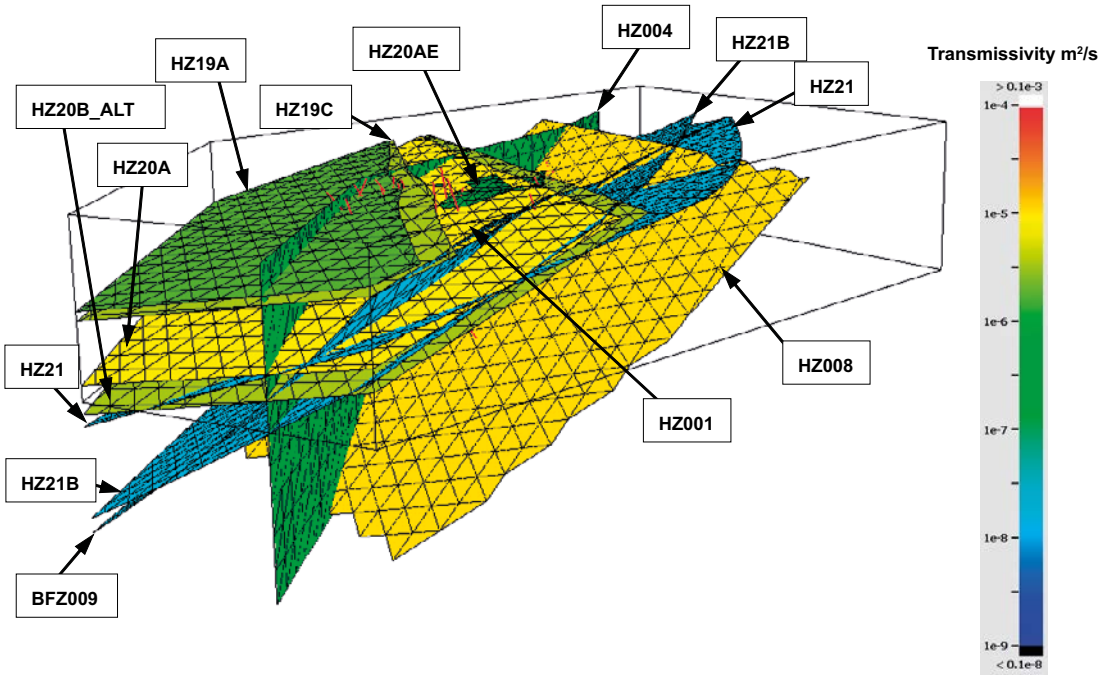

Figure 3-3. *Task 7A fault zones model represented by homogeneous unique transmissivity value for each fault zone.*

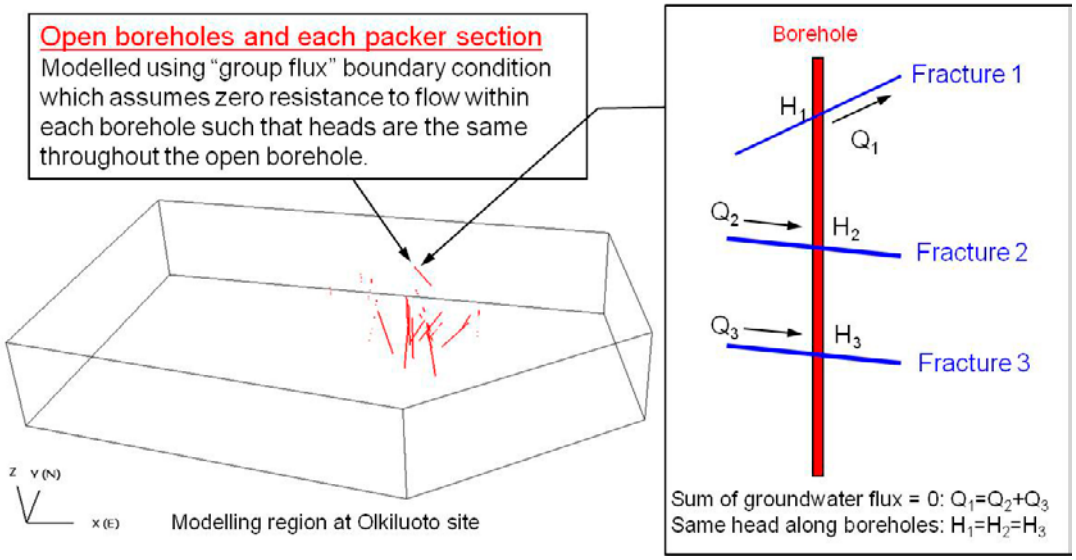

Figure 3-4. *Conceptual illustration of "Group Flux boundary condition".*

3.1.4 Processes considered

In this modelling study, the steady state seepage flow is assumed throughout the fault zones constructed by the DFN model and the surface layer modelled by continuum porous media (EPM). All fluids are assumed to be fresh water, with a constant density of 1 g/cc and a temperature of 20°C. The effect of the freshwater-saltwater interface and spatial variations in water density and temperatures (particularly near the Baltic Sea) have been ignored in this modelling.

3.1.5 Boundary and initial conditions

Boundary condition assumptions are listed in Table 3-1.

Table 3-1 Boundary condition assumptions used for Task 7A modelling (Vidstrand et al. 2012).

Boundary	Assumption
Topographic Surface (under Olkiluoto Island)	Base Case: Saturated to surface, such that Head=Elevation of ground surface
	Alternative Case: Phreatic surface calculated from vadose zone flow, assuming infiltration rate (obtain by model calibration at 5 mm/year)
Topographic Surface (under Baltic Sea)	Constant head H=0 (sea level), no skin effect to consider sea-bottom sediments
Vertical Sides and bottom of Model	No Flow (Q=0)

At the topographic surface, a constant head boundary, in which head equals to the elevation of ground surface was assumed as a basic case, and vadose zone flow (between the topographic surface and the groundwater table) was assumed to occur according to assumptions of Bear (1972), as an alternative case.

The algorithm used for the alternative case is as follows. The boundary condition at each node on the topographic surface depends on the depth of the phreatic (head) surface at that location. There are three possible states for these nodes:

- Swamped: the phreatic surface is at the ground surface and there is either a net outflow from the node to the surface, or the net inflow is less than the available infiltration due to precipitation. In this case, the head is set to the elevation, and the net outflow is calculated by the solver.
- Vadose: the phreatic surface is within a specified distance (generally 1 m) below the ground surface. In this case there is a net infiltration rate at the node, which varies from 0 m/s if the phreatic surface is at the ground surface, up to the specified maximum infiltration rate if the phreatic surface is 1 m below the ground surface. A vertical gradient of 1 is assumed in the vadose zone.
- Free: the phreatic surface is more than 1 m below the ground surface, and the specified user maximum infiltration rate is applied to the node.

The vertical side and the bottom were assumed to be a no flow boundary. At the Baltic sea floor, constant head boundary, head=0 m, was assumed.

Open boreholes and each packer section were modelled by using “group flux” boundary condition, as shown in Figure 3-4, which assumes zero resistance to flow within each borehole that heads are the same through the open borehole.

3.1.6 Numerical model

Modelling of Olkiluoto for Task 7A was carried out using FracMan (Dershowitz et al. 2007; www.fracman.com). FracMan is a hybrid discrete fracture network /continuum (DFN / EPM: Equivalent Porous Medium) code.

The Darcy flow equations were directly implemented, using a finite element flow solver, and particle tracking solute transport (Miller et al. 2001). For the purposes of Task 7A, FracMan was used with a combination of constant head, constant flux, group flux (well), and rainfall (infiltration) boundary conditions. Numerical implementation and solver assumptions and limitations are described in Miller et al. (2001).

Vadose zone flow modelling capabilities, supporting moving or variable phreatic surfaces, and spatially varying infiltration and discharge were also applied.

For Task 7A, FracMan was adapted to directly calculate PFL results corresponding to finite element flow solutions. This allows for direct comparison of field PFL measurements against results for the simulations. This calculation was carried out by considering the nodal fluxes entering and leaving the simulated open boreholes in the finite element model.

3.1.7 Parameters

The material properties assumed in this study are listed in Table 3-2, which are based on the specifications (Vidstrand et al. 2012). The hydraulic conductivity at the surface layer was set at $2 \cdot 10^{-7}$ m/s homogeneously without considering anisotropy. Porosity was 0.5%. Transmissivity of each fault zone was also specified as a single value per fault zone. Transport aperture was calculated from transmissivity using the empirical equation $e_t = a\ T^b$, where a=0.5, and b=0.5. In this modelling study, only the steady state flow conditions were considered. The storativity values for each zone, surface layer and fault zone is not defined.

Table 3-2. Material property assumptions for Task 7A modelling (Vidstrand et al. 2012).

Property	Assumption	
Hydraulic Conductivity of Surface Layers (EPM)	$2 \cdot 10^{-7}$ m/s (Homogeneous, Isotropic)	
Porosity of Shallow Layers (EPM)	0.5% (Homogeneous)	
Fault Zone Transmissivity	Fault zone name	Log of transmissivity (m^2/s)
	HZ001	–7.9
	HZ002	–6
	HZ003	–6.2
	HZ004	–6.8
	HZ008	–5
	HZ19A	–5.8
	HZ19C	–5.5
	HZ20A	–5.1
	HZ20AE	–6
	HZ20B_ALT	–5.5
	HZ21	–7.8
	HZ21B	–6.1
	BFZ099	–7.8
Fracture Zone Transport Aperture	$e_t = aT^b$, where a=0.5, and b=0.5	

3.1.8 Model conditioning and calibration

The simulations carried out for Task 7A are listed in Table 3-3, based on the specification of Vidstrand et al. (2012). Table 3-3 also summarises simulation conditions for each case, and the parameterization of results. The sensitivity analysis/calibration cases (e.g., SS02b and SS04b) focus on the uncertainty of fault zone transmissivity, which is one of key parameters affecting the head and flow distribution of the regional scale of hydrostructural model.

Vidstrand et al. (2012) define the geometric mean and standard deviation of transmissivity (in common logarithm scale) for each fault zone. We chose six major fault zones, HZ19A, HZ19C, HZ20A, HZ20B_ALT, HZ21 and HZ21B for sensitivity studies. These six fault zones were organized into three groups based on the similarity of location and orientation. For each of these three groups, a range of variation was defined from the specified standard deviation and six sensitivity cases were defined as listed in Table 3-4.

The same six sensitivity cases listed in Table 3-4 were also used for the transport modelling case PA01.

Table 3-3. Task 7A Simulation cases carried out by JAEA.

Case Name	Description	Forward/ Inverse	Boreholes	Conditions	Parameterization for comparison with measured data
SS01	Steady state flow conditions without pumping	Forward	No boreholes	Reference K and T Constant head at Olkiluoto ground surface	Infiltration rate through Olkiluoto ground surface Head distribution
SS02a	Steady state flow conditions with open boreholes	Forward	Boreholes are open and free to cross-flow.	Reference K and T Constant head at Olkiluoto ground surface Free to cross-flow borehole model	Infiltration rate through Olkiluoto ground surface Head distribution along boreholes Flow distribution along boreholes (PFL)
SS02b	Steady state flow conditions with open boreholes	Inverse	Boreholes are open and free to cross-flow.	Infiltration (Phreatic surface) boundary at Olkiluoto ground surface and calibrated to 5 mm/y **Sensitivity cases** Change T of fault zones	Head distribution along boreholes Flow distribution along boreholes (PFL)
SS02c	Steady state flow conditions without pumping	Based on SS02b	No boreholes	Best case of SS02b No flow borehole model	Head distribution along boreholes
SS03	Steady states flow with extraction from KR24	Forward	KR24 only	Pumping from KR-24 with flowing borehole model No flow borehole model for others	Head distribution along boreholes
SS04a	Steady states flow with extraction from KR24	Forward	KR24 + monitoring boreholes	Free to cross-flow borehole model Pumping from KR-24	Head distribution along boreholes Flow distribution at KR24 Flow distribution along boreholes (PFL)
SS04b	Steady states flow with extraction from KR24	Inverse	KR24 + monitoring boreholes	**Sensitivity cases** Change T of fault zones	Head distribution along boreholes Flow distribution at KR24 Flow distribution along boreholes (PFL)
PA01	Transport pathway simulation from KR24 to discharge under PA relevant BCs		No boreholes	Particle tracking from each release point along KR24	Statistics of the travel time

Table 3-4. Transmissivity values of each fault zone of the sensitivity cases for SS02b and SS04b.

Fault zone	Log of Transmissivity (m^2/s)		Range used for Sensitivity Studies	Sensitivity Analysis Cases					
	Geometric mean	Standard deviation		T1 (19 max)	T2 (19 min)	T3 (20 max)	T4 (20 min)	T5 (21 max)	T6 (21 min)
HZ19A	–5.8	1.6	±1.6	–4.2	–7.4	–5.8	–5.8	–5.8	–5.8
HZ19C	–5.5	1.3		–3.9	–7.1	–5.5	–5.5	–5.5	–5.5
HZ20A	–5.1	0.7	±0.9	–5.1	–5.1	–4.2	–6.0	–5.1	–5.1
HZ20B_ALT	–5.2	0.9		–5.2	–5.2	–4.3	–6.1	–5.2	–5.2
HZ21	–7.8	1.8	±1.8	–7.8	–7.8	–7.8	–7.8	–6.0	–9.6
HZ21B	–6.1	0.9		–6.1	–6.1	–6.1	–6.1	–4.3	–7.9

SS01: Base case, forward model, no boreholes

Case SS01 assumes reference transmissivity values for all faults, and the reference hydraulic conductivity for the surface layers. Case SS01 provides the basis for calculating the extent of hydraulic disturbances caused by the open and packed boreholes used for site characterization.

For Case SS01, a constant head boundary condition (H=z m) at the surface of Olkiluoto island as specified was assumed. This provides a further opportunity to evaluate the effect of this simplified assumption as compared to the moving phreatic surface that is assumed in later cases.

Results for Case SS01 are presented in Figure 3-5, with a comparison against measurements (which were taken for the site with open boreholes installed). A visualization of the head field on the fault zones is provided as Figure 3-6.

Conclusions from these simulations include the following:

1. A comparison of measured and simulated heads indicates that the boundary condition and material property assumptions of Case SS01 tend to over-estimate the heads near the surface. This is consistent with the modelling assumption that the water table everywhere matches the ground surface, while in fact the water table occurs at varying depths below the ground surface (expect at the location of surface ponds and streams).
2. Case SS01 simulation predicts that an infiltration rate of 19.7 mm/year is necessary to achieve a groundwater table at the surface. This is significantly higher than the expected infiltration (on the order of 5 mm/year). This is consistent with the fact that the assumed groundwater surface in the model is higher than the groundwater surface at the site.
3. The measured heads tend to be fairly constant with depth, and sometimes even increase with depth (KR01, KR12, KR04) that might be caused by salinity effect. In contrast SS01 modeled heads consistently decrease with depth. In the SS01 model, the only source for these lower heads would be a strong connection at depth to the H=0 boundary condition assumed at the sea-floor. The implication is that it would be more realistic to assume a low-permeability skin representing sea-bottom sediments, to maintain the observed hydrostatic head distribution under Olkiluoto. This conclusion needs to be somewhat tempered by the fact that the measurements as shown on Figure 3-5 are not directly comparable to the simulation results, which do not include vertical boreholes and salinity effect that we might expect to become significant below 500/600 m. These boreholes could have increased vertical hydraulic connectivity, resulting in the more hydrostatic head measurements observed.

SS02a: Base case, forward model, with open boreholes.

Case SS02a also assumes reference transmissivity values for all faults, reference hydraulic conductivity for the surface layers, and a constant head boundary condition (head=z m) at the surface of Olkiluoto. The only difference between Cases SS01 and SS02a is the inclusion of flow disturbances due to the installation of packed and open boreholes. As a result, the comparison of simulations for SS01 and SS02a can be seen as an indication of the effect of the boreholes on the groundwater system.

Results for Case SS02a are presented in Figure 3-5. A visualization of the head field on the fault zones is provided as Figure 3-7.

Conclusions from these simulations include the following:

1. A comparison between simulations SS01 and SS02a shows that heads are higher on average in SS02a than in SS01, indicating a stronger connection to the constant head boundary condition applied at the topographic surface.
2. Simulated heads in SS02a tend to be fairly constant with depth, as they are in the in situ measurements. This indicates that the vertical connectivity provided by open boreholes can cause hydrostatic pressures at depth observed near the boreholes.
3. Simulated heads in SS02a tend to be somewhat higher than measurements, which might be explained the modelling assumption that the water table everywhere matches the ground surface, while in fact the water table occurs at varying depths below the ground surface (expect at the location of surface ponds and streams).
4. Case SS02a simulation predicts the same infiltration rate (19.8 mm/year) as Case SS01 (19.7 mm/year). This indicates that the redistribution of head due to the open boreholes does not result in a significant increase in the average rock mass permeability.

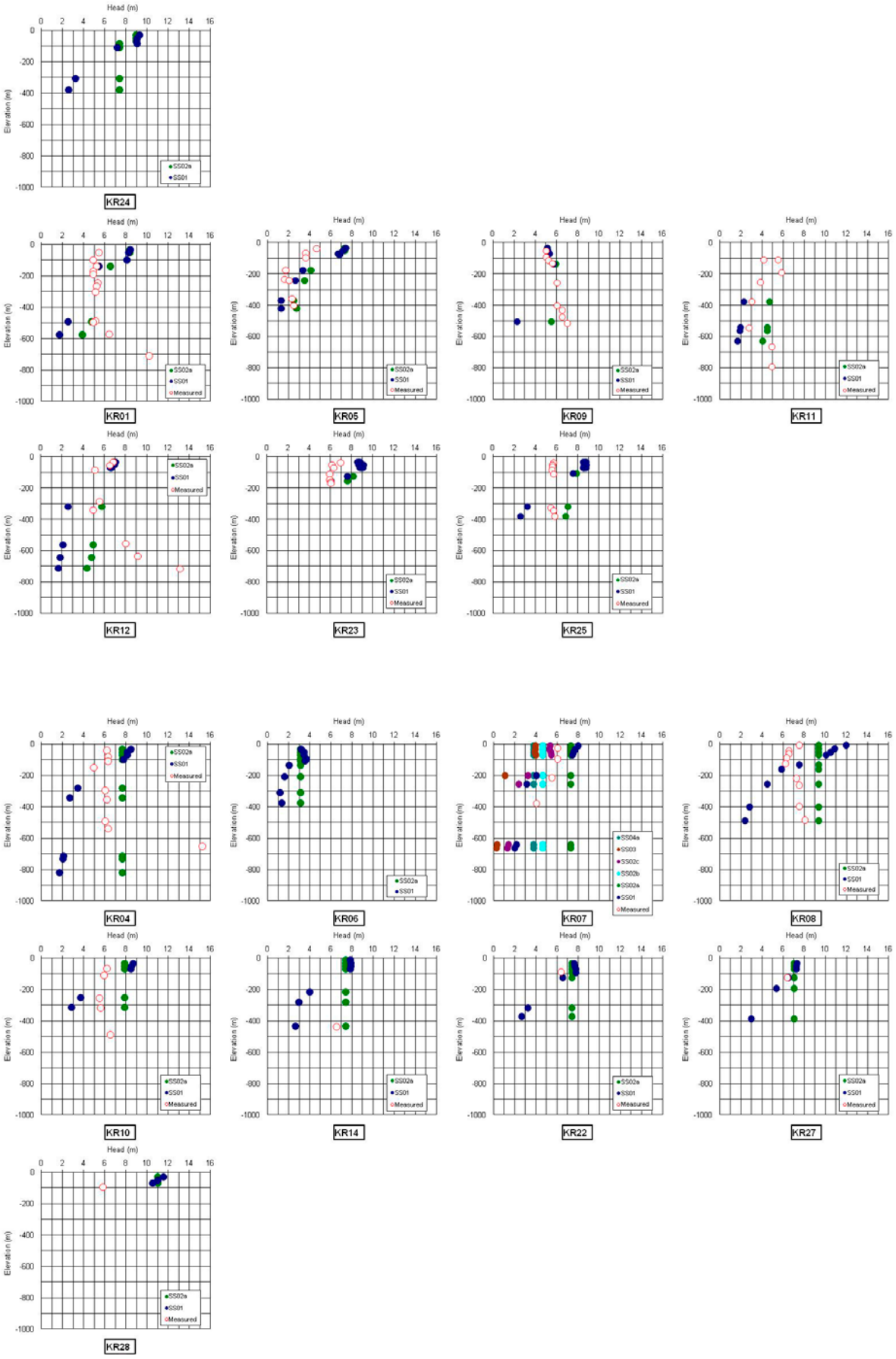

Figure 3-5. *Steady state flow simulation results for both SS01 and SS02a; head distribution along the boreholes with measured data.*

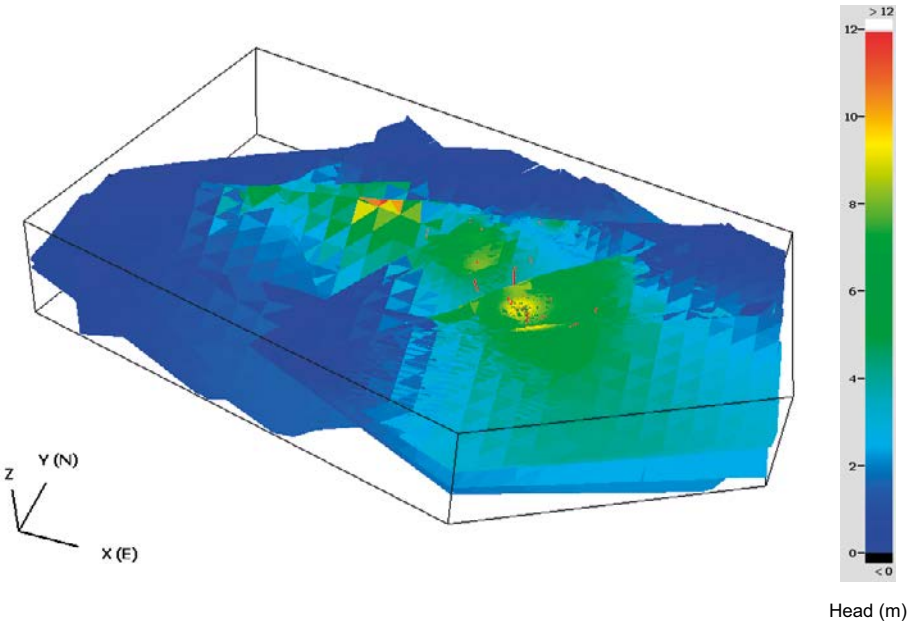

Figure 3-6. *Steady state flow simulation results for SS01; head distribution at fault zones.*

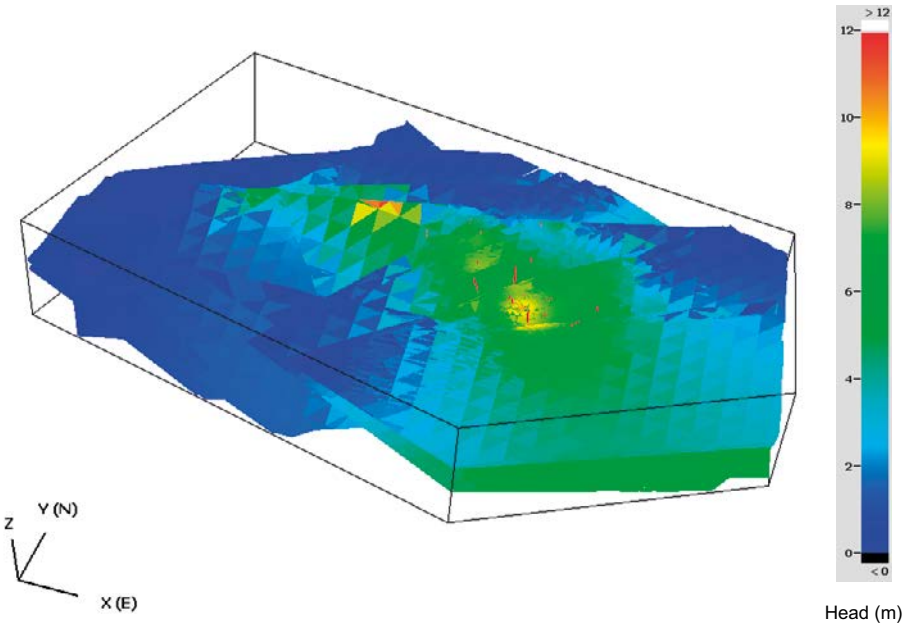

Figure 3-7. *Steady state flow simulation results for SS02a; head distribution at fault zones.*

SS02b: Sensitivity study with open boreholes and SS02c: steady state study without boreholes

Case SS02b explores how boundary condition and material property assumptions can be varied to obtain a better match between simulated and measured head and PFL flows. For this and subsequent cases, topographic surface boundary condition was switched from the constant head boundary condition, assumed for cases SS01 and SS02a to a moving phreatic surface boundary condition. The phreatic surface boundary condition is specified as a vadose zone depth and a maximum infiltration rate. For case SS02b, this maximum infiltration rate was calibrated to match the average infiltration rate of 5 mm/year, recommended by Vidstrand et al. (2012).

Figure 3-8 shows spatial pattern of discharge and recharge rate and locations with maximum infiltration set to achieve an average infiltration rate of 5 mm/year. Figure 3-9 shows the head distributions for each of the boreholes at this average infiltration rate configuration.

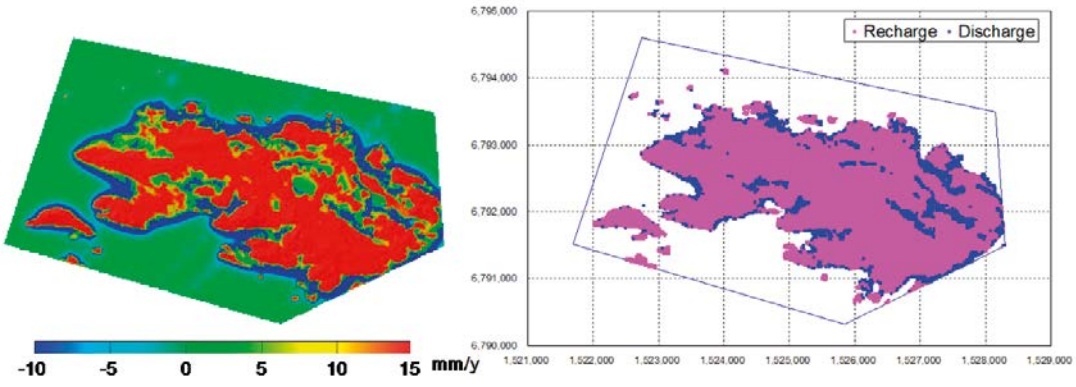

(a) Infiltration rate distribution

(b) Recharge / Discharge points distribution

Figure 3-8. *Calculated discharge and recharge distribution at Olkiluoto site; results of calibration of infiltration rate of first calibration step in SS02b case.*

Conclusions from this simulation include the following:

1. At the average infiltration rate of 5 mm/year, using reference material properties, discharge at surface only occurs at very limited, low elevation locations.
2. To achieve an average infiltration rate of 5 mm/year, infiltration varies locally from as high as 15 mm/year to 0 mm/year.
3. The reduction of average infiltration from 19.8 mm/year (SS2a) to 5 mm/year (SS2b) causes a reduction in the simulated head on boreholes. This improved the match to measurements, particularly for boreholes KR1, 5, 23 and 25, as shown in Figure 3-9.

After adjusting the surface boundary condition to match an average 5 mm/year infiltration, a sensitivity study of the influence of fault zone transmissivity on local heads and PFL flow rates was carried out. The sensitivity cases studied are listed in Table 3-4. Results from these sensitivity studies are presented in Figure 3-10 (heads), Figure 3-11 (PFL flow rates) and Figure 3-12 (visualization).

Conclusions from this simulation include the following:

1. The infiltration rate among the fault zone transmissivity sensitivity cases is varied from 4.7 mm/y to 5.9 mm/y, which is not significant differences compared with the differences in infiltration rate from the SS01 and SS02a cases.
2. The comparison of measured and simulated steady state heads (Figure 3-10) indicates that the sensitivity study T4 case provided an improved match with measured data. Sensitivity study T4 case assumes a lower transmissivity for zones HZ20A and HZ20B_alt.
3. None of the sensitivity cases studies was able to reproduce the observed significant increase in head with depth found in boreholes KR01, 09 and 12, This indicates that there is something significant at deeper zones in either the boundary conditions or hydrostructural model connectivity that is missing from the numerical models as simulated.
4. The magnitude of simulated PFL flow rates (Figure 3-11) is consistent with measurements for SS02a and for the SS02b sensitivity cases. Interestingly, there are locally high measured PFL flow rates which do not appear in the simulations (for example, at a depth of 100–150 m in KR22), and there are locally high simulated PFL flows rates that do not appear in the in situ measurements (for example, at a depth of 440–460 m in KR27). This indicates that there are locally significant flow features that are not properly modeled in the reference hydrostructural model. This is consistent with the uncertainty in the hydrostructural model, and with the fact that many smaller fault zones are not included in the hydrostructural model. However, from a statistical sense it is important to notice that there are a total of five locations of significant PFL flow in the measurements and a similar total of seven locations of significant PFL flow in the simulations.
5. It is difficult to judge between the different sensitivity study cases based on the simulated PFL flows. The sensitivity case T4 appears to slightly better match the average PFL flow, and the pattern of PFL flow. Based on this, it appears that PFL flow logs have a limited ability to reduce the uncertainty concerning fracture zone transmissivity in this study under the Task 7A conditions, such as an assumption of averaging (homogeneous) fault zone properties at each fault zone.

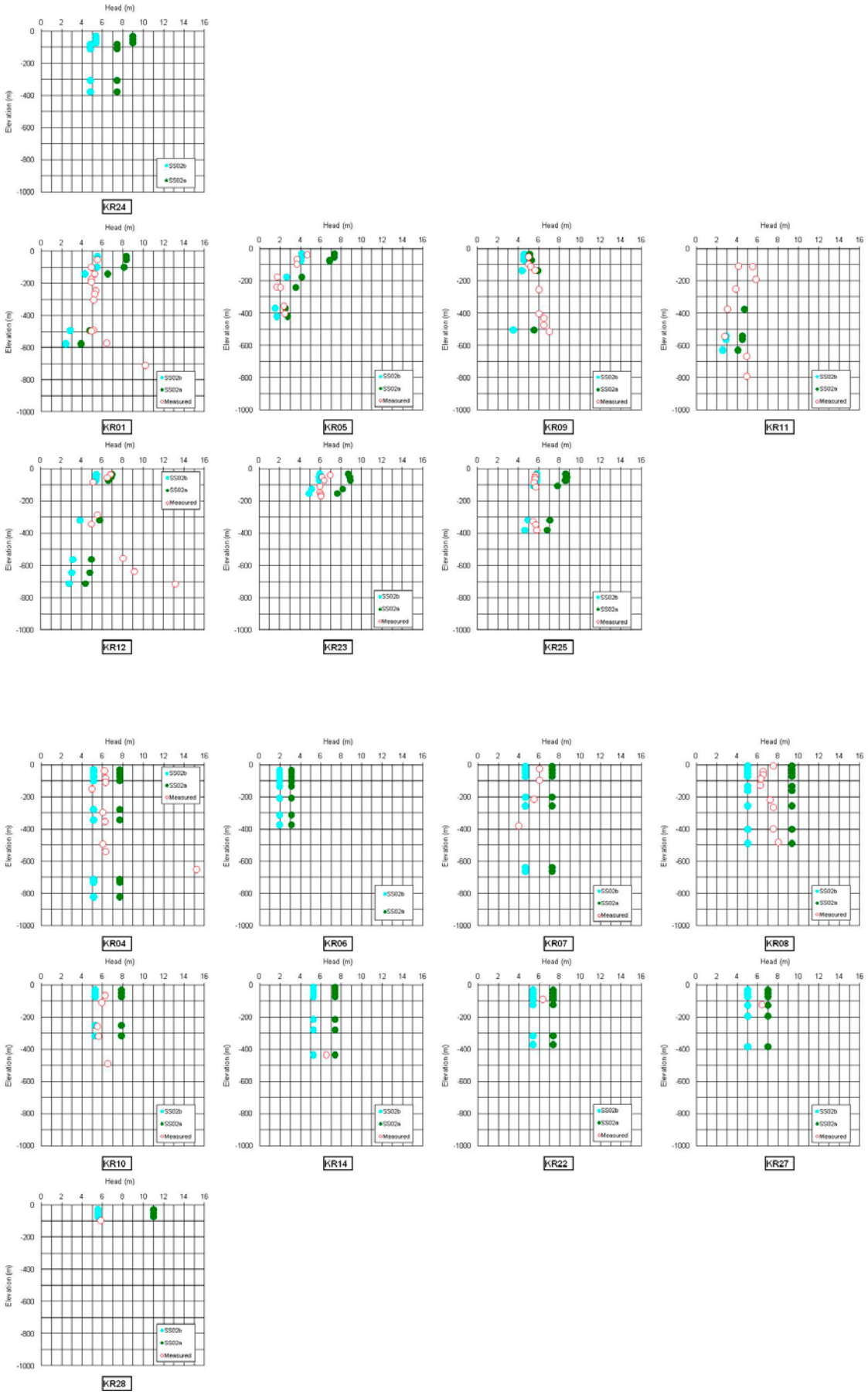

Figure 3-9. *Steady state flow simulation results of first step of SS02b compared with SS02a; head distribution along the boreholes with measured data.*

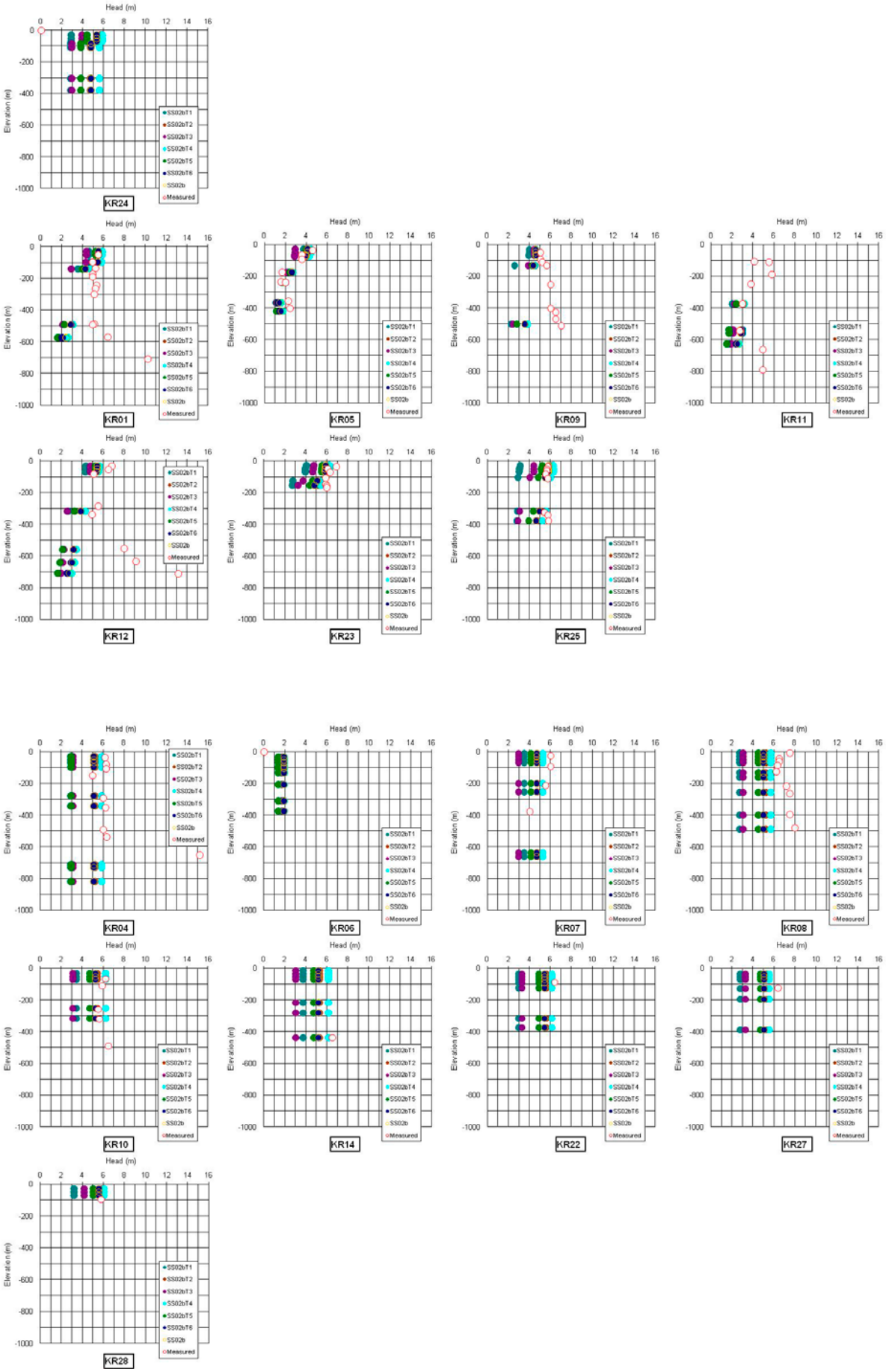

Figure 3-10. *Steady state flow simulation results of second step of SS02b compared with first step of SS02b; head distribution along the boreholes with measured data.*

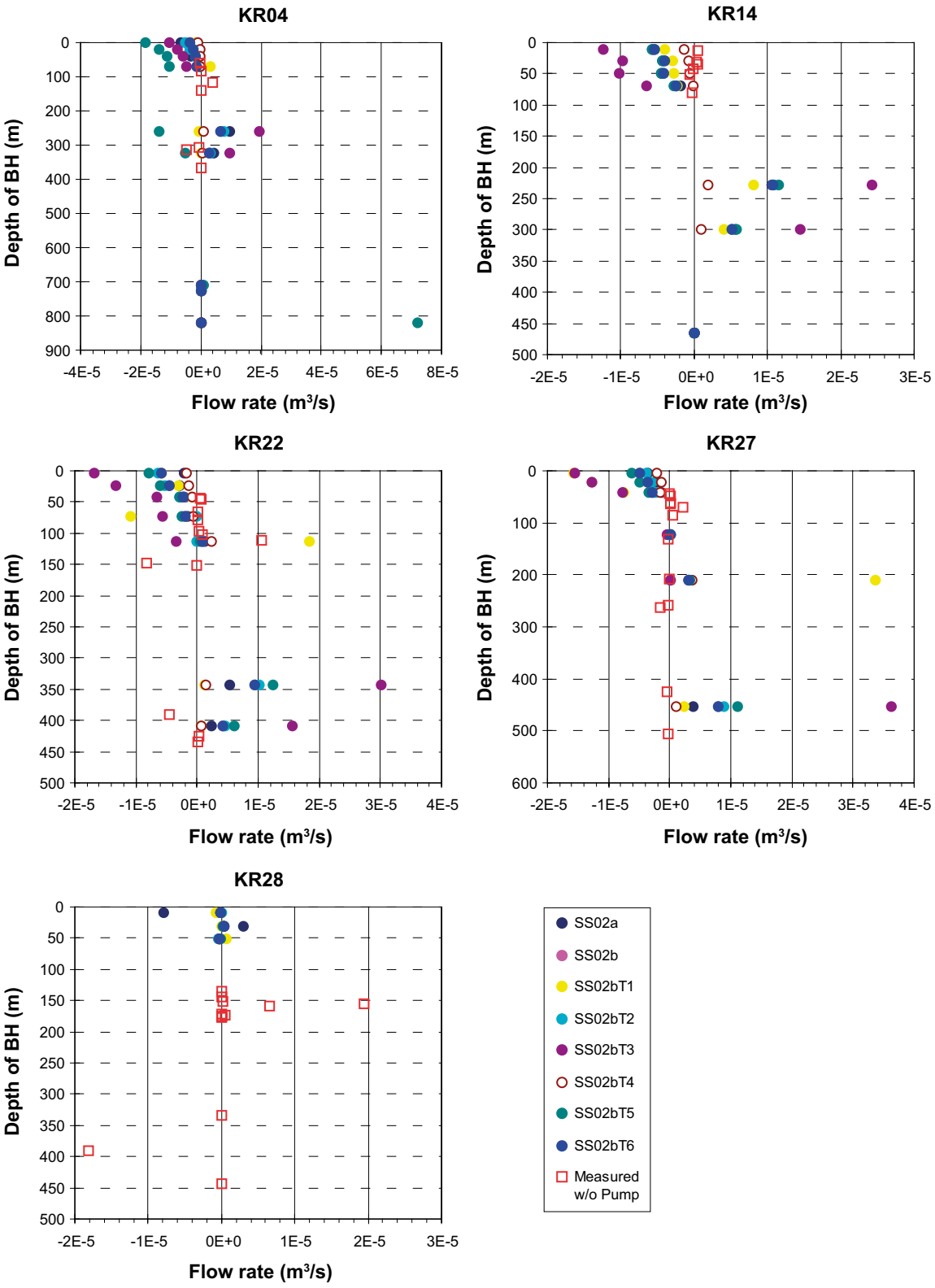

Figure 3-11. *Comparison of flow rate along the borehole, between PFL data and simulated results; first step of SS02b and SS02a.*

Case SS02c was simulated with the approximate 5 mm/year infiltration rate and material properties of sensitivity case T4, with no vertical connectivity provide by boreholes. This result, shown in Figure 3-13, can be compared against the same modelling assumptions, but with Case SS02b borehole connectivity (Figure 3-12). As in the comparison between cases SS01 and SS02a, the effect of borehole connectivity appears to be an average slight increase in head, and an increase in the uniformity of head with depth.

SS03, SS04a, forward model, steady state pumping from Borehole KR24

The purpose of simulations SS03 and SS04a was to explore the ability of the KR24 borehole pumping test to reduce the hydrostructural model uncertainty. Both SS03 and SS04a were simulated with pumping from borehole KR24 as specified in Vidstrand et al. (2012); i.e., 12.5 litres/minute (L/min.) from upper section and 5.5 L/min. from lower section, with a by-pass packer in between the sections. The difference between SS03 and SS04a is that SS04a considers the experiment as actually conducted, with open boreholes providing vertical connectivity, while SS03 models the experiment as if all boreholes had been packed off to eliminate borehole connectivity effects.

Results for cases SS03 and SS04a are shown in Figures 3-14, and SS04a is visualized in Figure 3-15. Results for these cases are presented as drawdown rather than as head value, in order to distinguish the effect of the KR24 pumping from other issues.

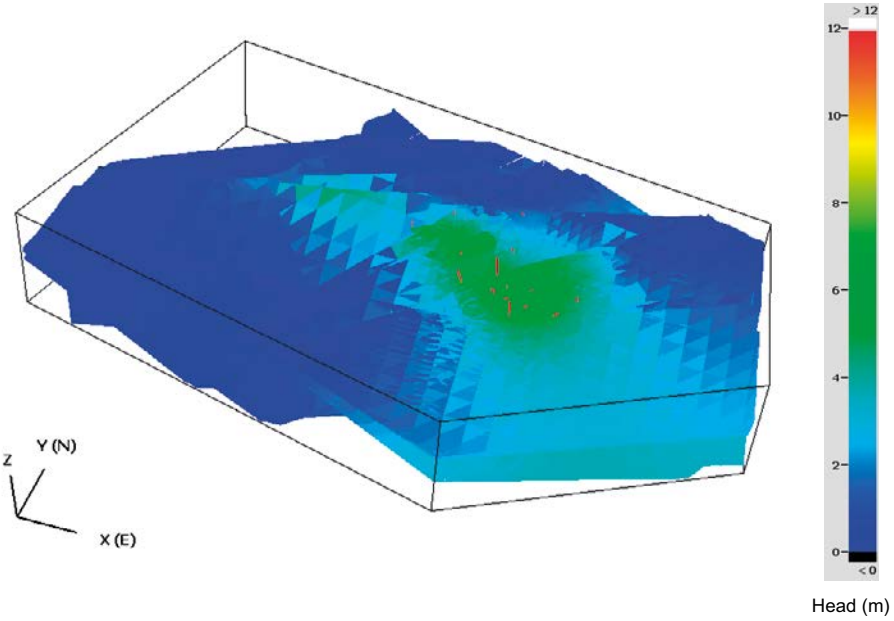

Figure 3-12. *Calibrated results for SS02b; head distribution at fault zones.*

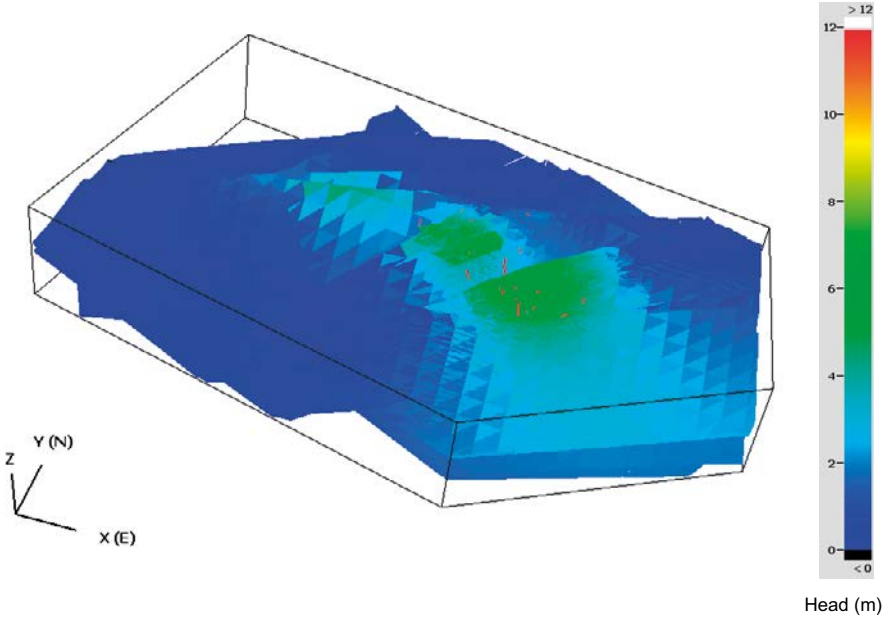

Figure 3-13. *Steady state simulation results for SS02c; head distribution at fault zones.*

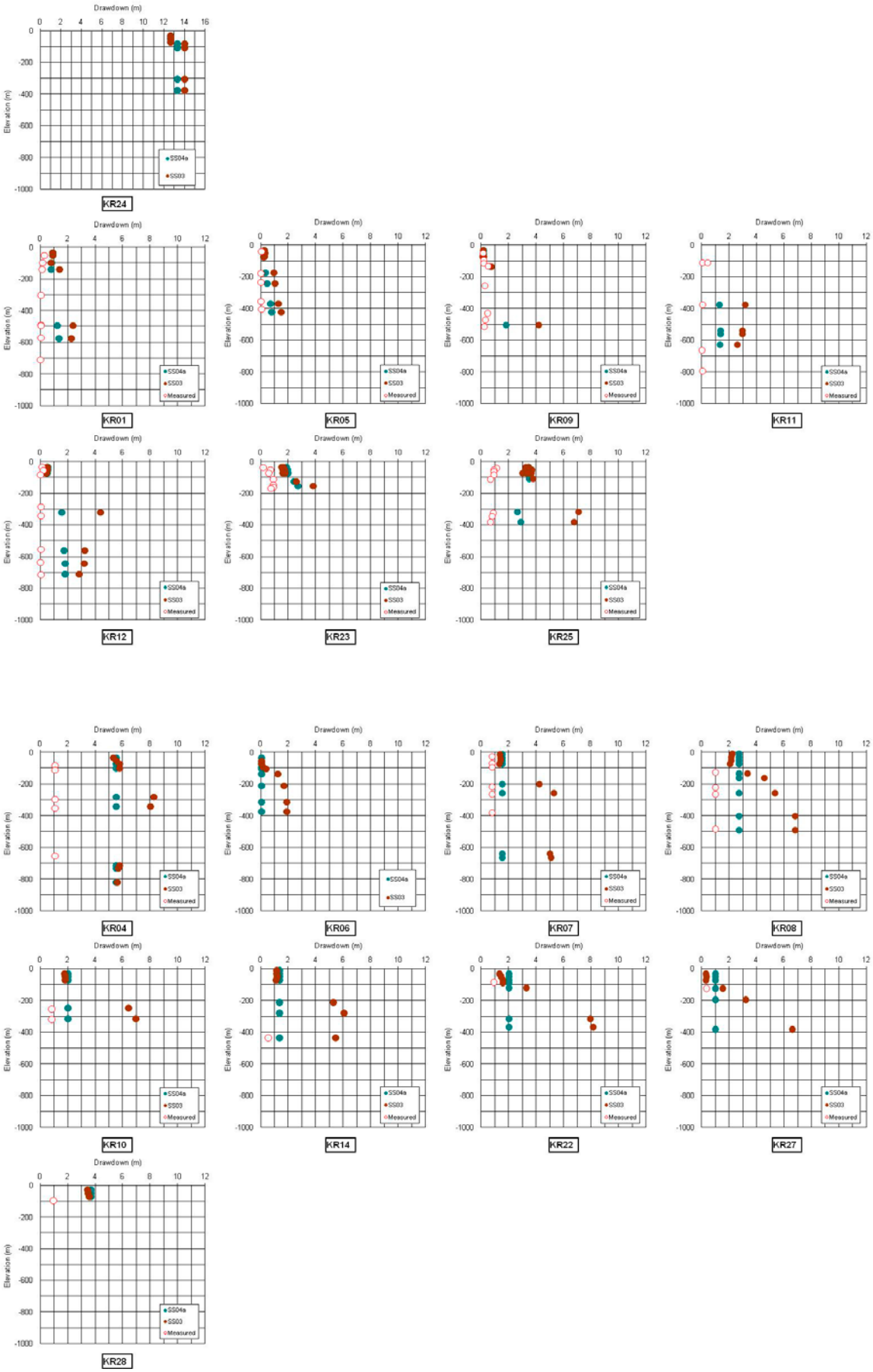

Figure 3-14. *KR24 pumping steady state flow simulation results for both SS03 and SS04a compared with measured data, presented as drawdown along the boreholes with measured data.*

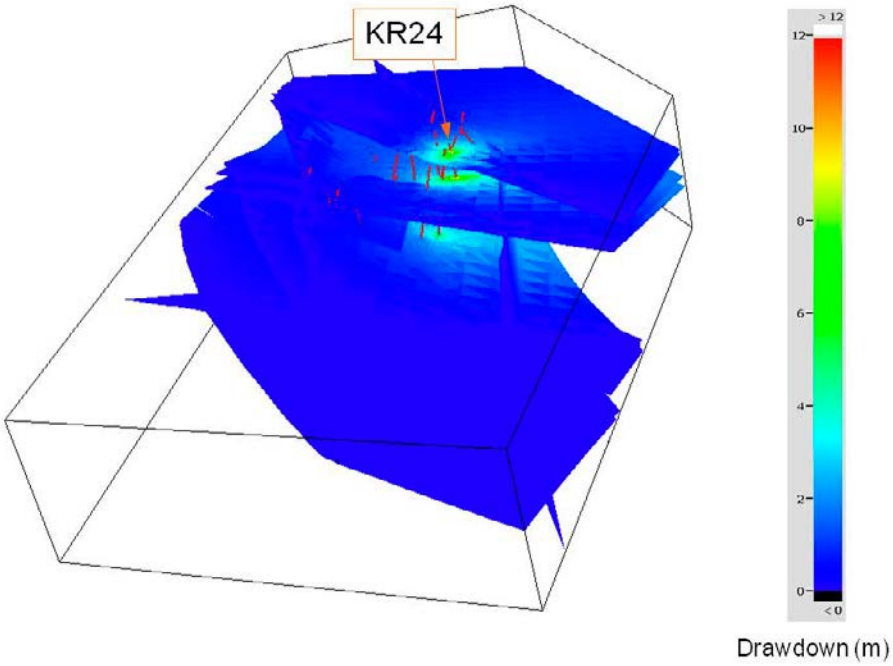

Figure 3-15. *Drawdown distribution at fault zone for SS04a case.*

Conclusions from simulations SS03 and SS04a include the following:

1. Measured drawdowns are generally much smaller (0 to 1 m) compared to simulated drawdowns (2 to 8 m). This is especially true for borehole KR 23 and 25 in the surface layer and for borehole KR4 for all zones. This indicates that the model is less able to replace the water pumped from KR24 than is the case for actual in situ conditions. One possible explanation for this is the use of no-flow boundary conditions on the vertical edges of the model incorrectly restricts the flow of water into the rock volume under KR24 pumping conditions. Another possible explanation is that there could be local heterogeneities in the fracture zones which reduce the sensitivity of borehole measurements to the KR24 pumping.
2. Simulation SS04a provides a much better match to drawdowns than SS03, which does not include the effect of open boreholes. This indicates that these open boreholes have a major effect on the results of the KR24 pumping test, averaging out local hydraulic responses, and making it more difficult to use the pumping test results to constrain the properties of faults as they intersect the boreholes.
3. Simulation SS03 shows a greater variability in drawdown than either the measurements or SS04a, both of which included vertical open holes. The absence of this local variability in the case of open boreholes makes it more difficult to validate the conceptual model using this test, and limits the uncertainty reduction achieved. This might be partially offset by looking at the PFL measurements.

SS04b, Sensitivity Study, Pumping from Borehole KR24

The SS04b sensitivity study used the same variation cases as SS02b, listed in Table 3-3. In addition to the T1 through T6 cases simulated in SS02b, the assumptions used before SS02b were added as a reference case, labeled “T0.”

Results from these simulations are presented as drawdown (Figure 3-16) and a PFL flow (Figure 3-17). Conclusions from these simulations include the following:

1. Changes in fault zone transmissivity over the wide range shown in Table 3-4 were insufficient to move the drawdown down to the 0 to 1 m level of the measurements. This indicates that the discrepancy is more likely due to surface boundary condition issues than to material property (i.e. fault transmissivity).

2. Large changes in fault transmissivity are more effective in reducing drawdowns for some wells (such as KR23) than for other wells (such as KR28). This indicates that the ability of pump tests to distinguish values of fault transmissivity is limited by how direct the connection is between the pumping and monitoring wells.
3. Case SS04a (T4 case fault properties described in Table 3-4) has lower average drawdown and hence is a better match with in situ measurements.
4. The measured shallow and deep drawdowns (presumably responding to the shallow and deep pumping sections of KR24) are similar for most wells. This is also true for most of the simulations. This indicates "success" for the implementation of vertical hydraulic connectivity in the wells, but shows a limitation of open boreholes when trying to distinguish hydraulic responses.
5. Comparison of all these sensitivity cases shows that the magnitude of drawdown can be calibrated to some extent by varying the fracture zone transmissivity. However, the sensitivity is limited, and absent a compelling variation in drawdown between wells or with depth, there is low confidence in the use of this drawdown information to reduce the uncertainty in the interpretation of fracture zone transmissivity.
6. PFL flow rate patterns with KR24 pumping (Figure 3-17) are very similar to those without pumping (Figure 3-10). The vertical connectivity of the rock mass due to the open boreholes appears to limit the variability of PFL responses, and hence the ability of the PFL to reduce uncertainty about the properties of the faults.
7. All sensitivity simulations have significant PFL flows in the shallow zone, although the use of a continuum EPM to model the surface layer was expected to result in an under-prediction of the PFL flow rate. This result indicates that the flow rate to the borehole at the sallower zone might significant to keep water balance along the boreholes during PFL measurements.
8. The locations of PFL anomalies in the simulations do not match the location of measured PFL anomalies in boreholes. This indicates a systematic limitation of the accuracy of the hydrostructural model. This error is beyond what can be addressed in the simulations carried out, which maintained the geometry of faults and only varied their properties.
9. On average, the reference SS04a case provides a better match to PFL measurements than any of the sensitivity cases considered. However, none of the cases provided a convincing match. For example, the measured high flow rate (both negative and positive) of around –150 m depth in borehole KR22 and at an approximate 400 m depth in borehole KR28 were not reflected in any of the simulations.
10. The value of both the KR24 pumping test in general, and the PFL flow measurements in particular seem to be limited by the vertical connectivity provided by the open boreholes.

PA01, Particle Tracking of Transport Pathways

One of the purposes for Task 7A is to examine how site characterization data such as the KR24 pumping test and the PFL measurements can constrain the hydrostructural model and PA relevant parameters calculated from the hydrostructural model. This issue is very difficult to quantify, and therefore the PA01 case concentrated on the reduction of uncertainty concerning:

- advective travel time distribution,
- advective travel distance,
- pathway geometry.

It is hoped that PA01 will show that the uncertainty in these parameters within uncertainty of the hydrostructural model of Vidstrand et al. (2012) will be reduced by constraining the results to the T4 case which provided the best match to head and flow measurements.

The PA01 case was conducted by particle tracking method to calculate groundwater travel time and transport pathway geometry as "PA relevant performance measures" for pathways from three release points specified along KR24 (RP1, RP2, and RP3) under Olkiluoto Island. Particle tracking pathways were derived head fields corresponding to each of the six cases used for studies SS02b and SS04b (see Table 3-4). These simulations were carried out for cases without open boreholes, and with no pumping boreholes, to approximately undisturbed steady state boundary conditions.

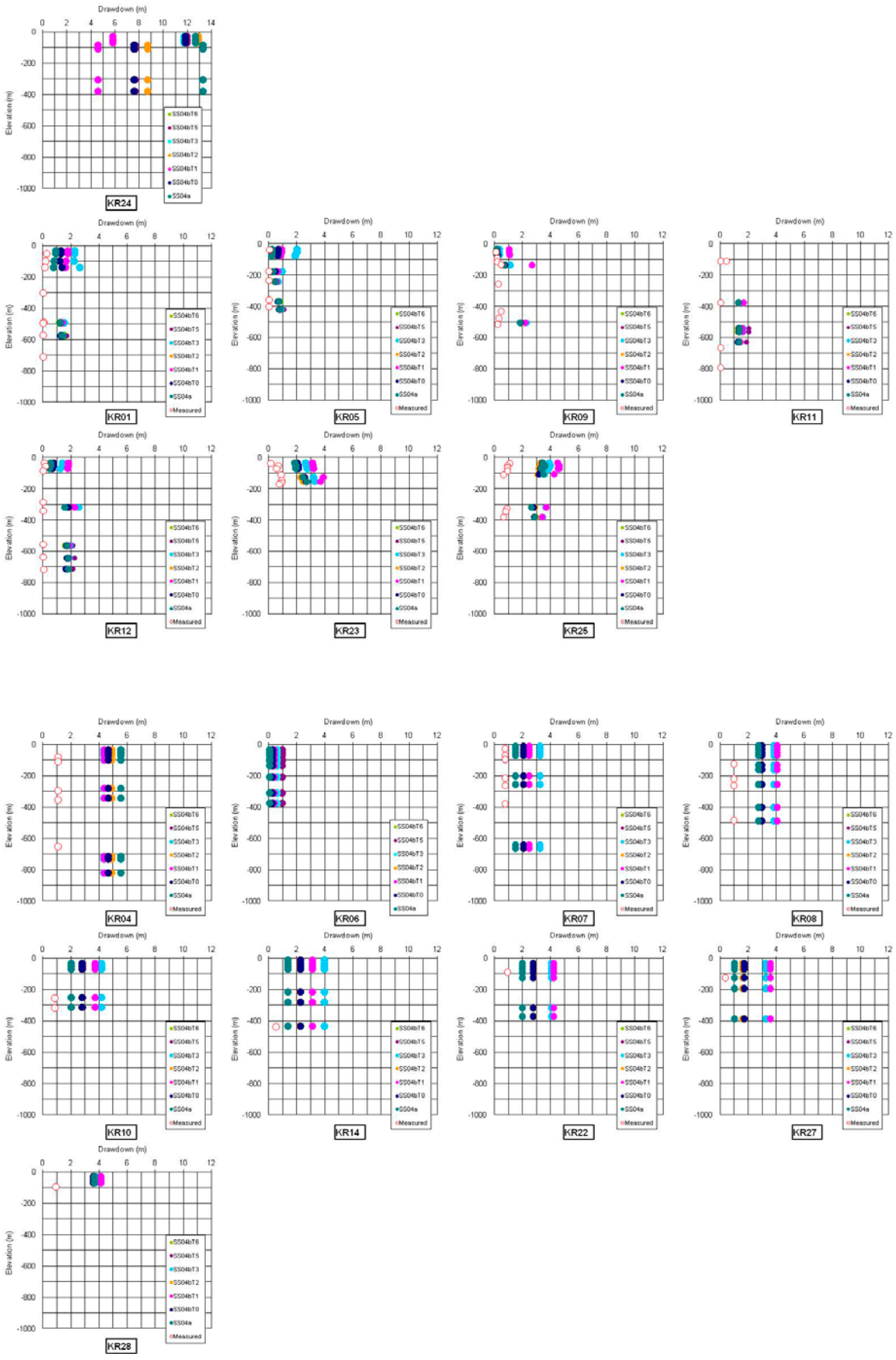

Figure 3-16. *KR24 pumping steady state flow simulation results for both SS04b, presented as drawdown along the boreholes with measured data. The ss04bT4 case is same case as the ss04a case.*

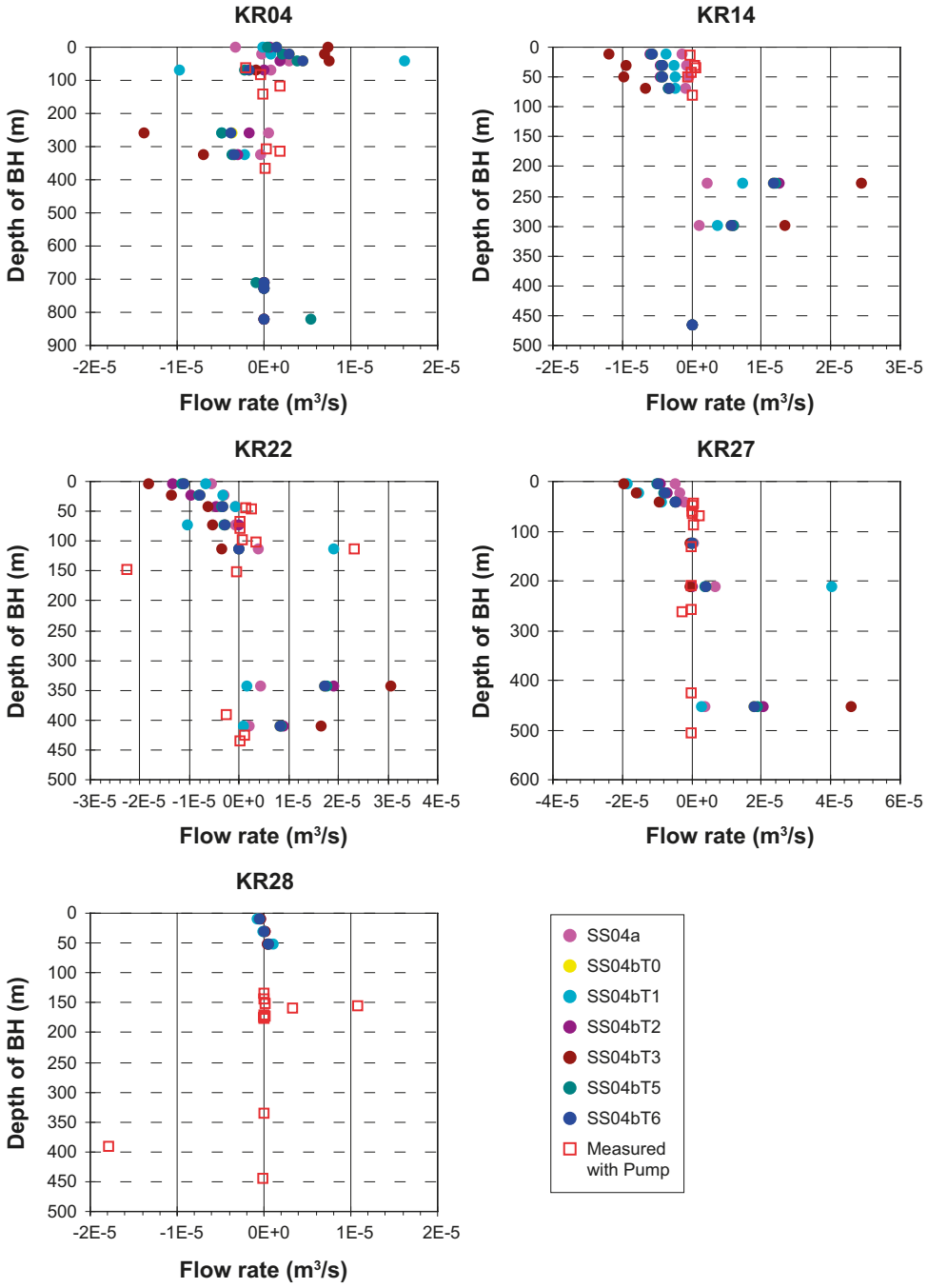

Figure 3-17. *Comparison of flow rate along the borehole, between PFL data and simulated results, first step of SS04a and SS04b.*

For study PA01, approximately 100 particles were simulated at each of the three release points. PA01 focuses on advective pathways, and therefore dispersion was only included in the solute transport simulations to the extent necessary to exercise a range of advective pathways for each release point. Consequently, longitudinal dispersion was assumes as 1 m, and transverse dispersion was assumed as 0.1 m.

Simulation results are provided in Figures 3-18 through 3-27. Figure 3-18 illustrates the cumulative probability density function (cpdf) for particle travel time for PA01 (assuming the material properties of the T4 case) from RP1, 2 and 3. Figure 3-19 also shows particle travel distance for PA01 (T4 case) from RP1, 2 and 3. In both figures, a solid line shows travel time and distance within fault zones and dotted line shows the travel time including the travel in the EPM elements of the surface layer.

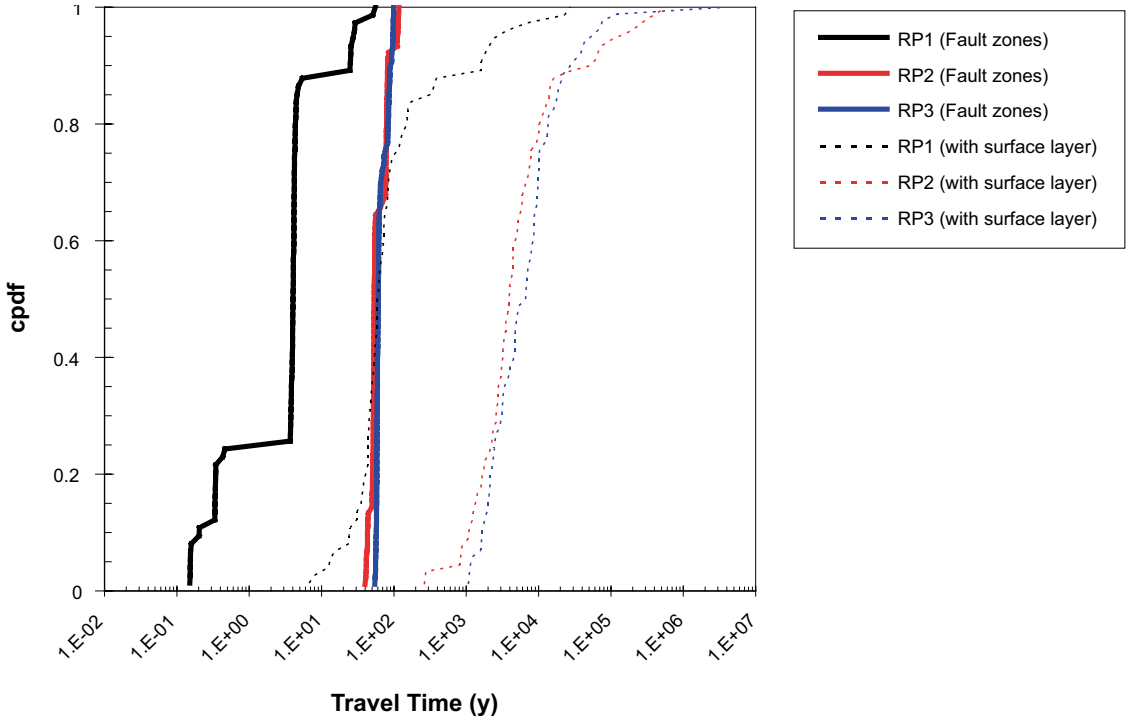

Figure 3-18. *Cumulative probability density function (cpdf) of particle travel time for PA01 cases (T4 case) from RP1, 2 and 3. Solid line shows travel time within fault zones and dotted line shows travel time to the boundary including surface layer.*

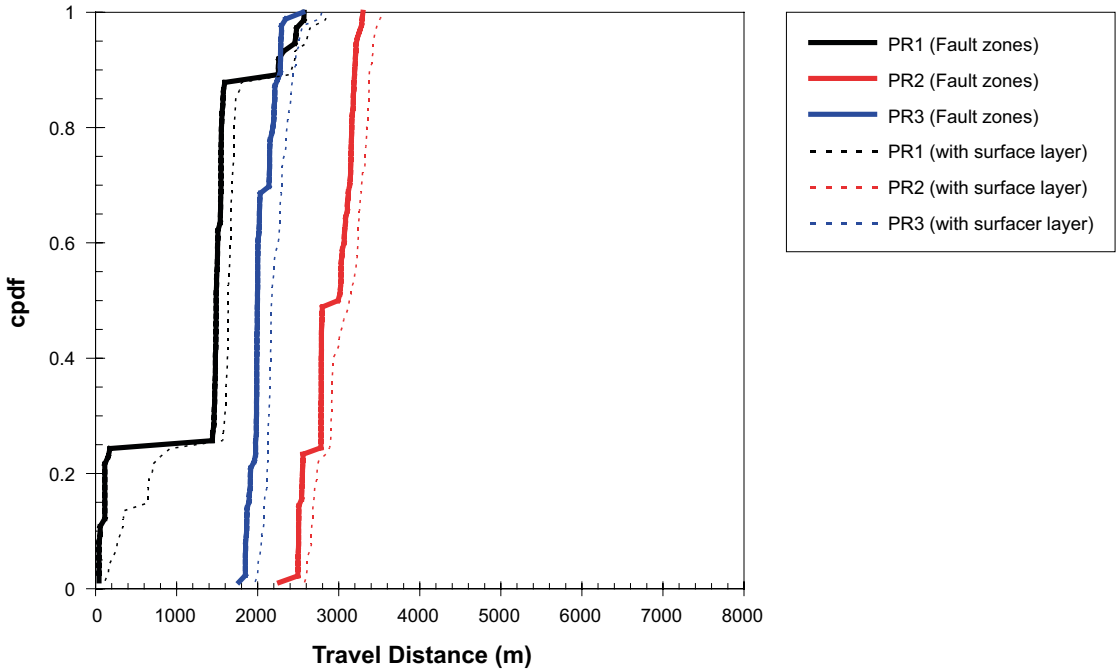

Figure 3-19. *Cumulative probability density function (cpdf) of particle travel distance for PA01 cases (T4 case) from RP1, 2 and 3. Solid line shows travel time within fault zones and dotted line shows travel time to the boundary including surface layer.*

It is important to distinguish between the transport in the DFN fracture zones and transport in the shallow EPM layers, because the site characterization activities evaluated in this task focus primarily on the faults, while the high porosity (0.5%) assumed for the surface layers means that most of the actual travel time is spent in the EPM elements.

The effect of surface layers on particle travel distances (Figure 3-19) is much less significant. Particles released from RP2 (HZ20A) and RP3 (HZ20B_ALT) tend to have larger travel time and travel distance, than time and distance released from RP1 (HZ19A and HZ19C). Average travel times and distances of the three particle release locations are provided in Table 3-5.

Figures 3-20 through 3-22 show example transport pathways (particle trajectories) for the particle release locations RP1, RP2, and RP3, respectively. Particles released from RP1 (Figure 3-20) pass through zones HZ19A and HZ19C, which are connecting RP1 section, and then tend to travel south along zones HZ19A and HZ19C to discharge locations on the surface boundary (Olkiluoto ground surface and coastal area). A few particle pathways from RP1 follow a longer pathway which includes the deeper fault zones HZ20A and HZ20B_ALT via HZ004 before travelling through the EPM elements to a discharge location beneath the Baltic.

The particle trajectories from RP2 are shown in Figure 3-21. All particles released from location RP2 travel through fault zone HZ20A, which is connected to the RP2 release location, and then tend to travel to south along HZ20A to the shallow EPM elements, and then to their discharge locations at the Baltic Sea near southern edge of the model. A few particle pathways from RP2 travel through fault zone HZ20B_ALT via HZ004 to the shallow EPM elements and then discharge to Baltic Sea.

The particle trajectories from release location RP3 are shown in Figure 3-22. All particles from release location RP3 travel through the fault zone HZ20B_ALT, which directly connects to the RP3 release section. From there, these particles follow pathways south through fault zone HZ20B_ALT, up to the shallow EPM elements, and then discharge to the Baltic Sea.

Table 3-5. Average of travel time and travel distance.

Particle release point	Travel time (year)		Travel distance (m)	
	Fault zones	Breakthrough to boundary	Fault zones	Breakthrough to boundary
RP1	6.6	1,012.2	1,274	1,481
RP2	63.2	27,091.5	2,902	3,077
RP3	67.6	57,222.3	2,043	2,235

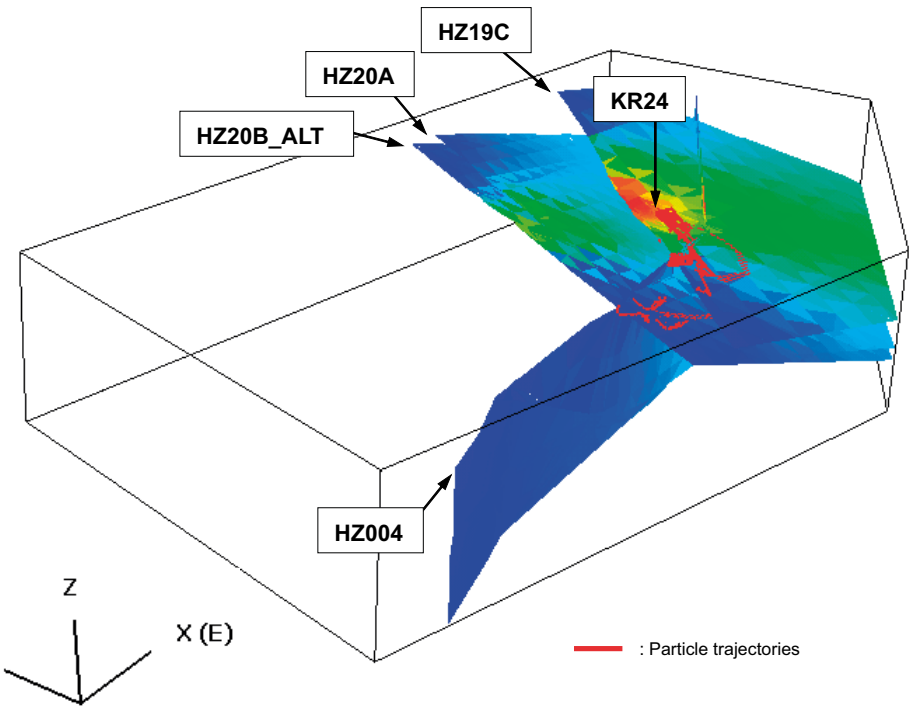

Figure 3-20. *Particle trajectories of PA01 cases (T4 case) from RP1. Solid red line shows the particle trajectories from RP1.*

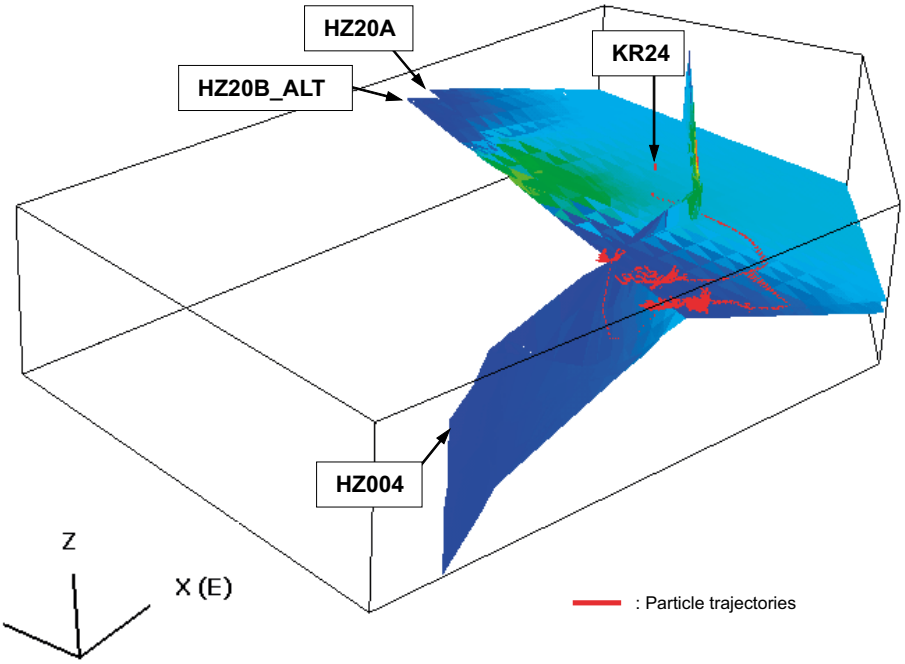

Figure 3-21. *Particle trajectories of PA01 cases (T4 case) from RP2. Solid red line shows the particle trajectories from RP1.*

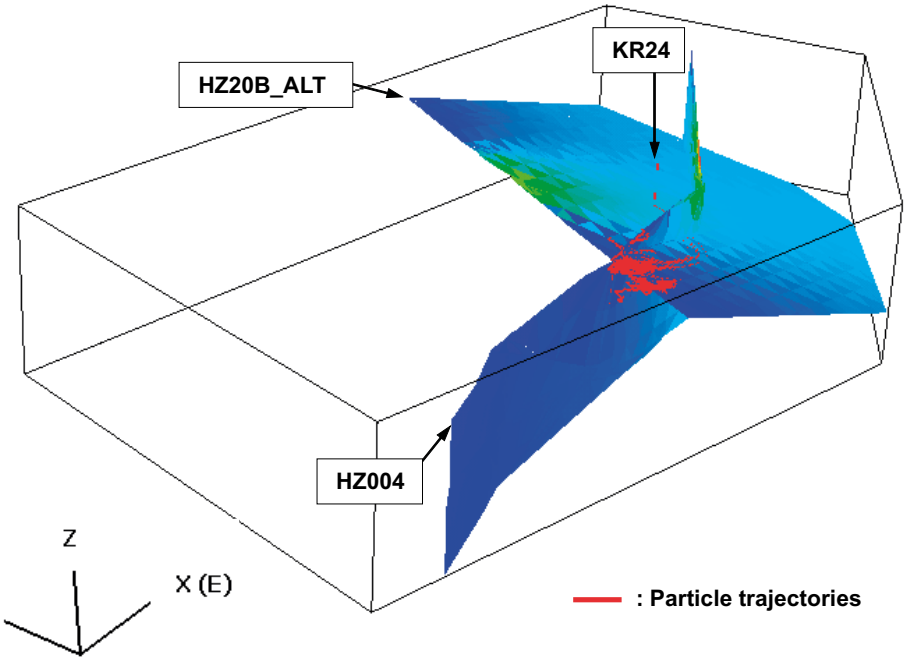

Figure 3-22. *Particle trajectories of PA01 cases (T4 case) from RP3. Solid red line shows the particle trajectories from RP3.*

Figure 3-23 presents travel time and travel distance distributions for the three release points, for a total of eight sensitivity cases, including the six cases listed in Table 3-4. For each of these cases, the distribution of (a, c, e) advective travel time and (b, d, f) advective travel distance. Solid lines indicate the portion of the pathway within the DFN elements representing the fault zones, and dashed lines indicate results for the total pathway, including time and distance spent in the EPM elements representing the shallow layers.

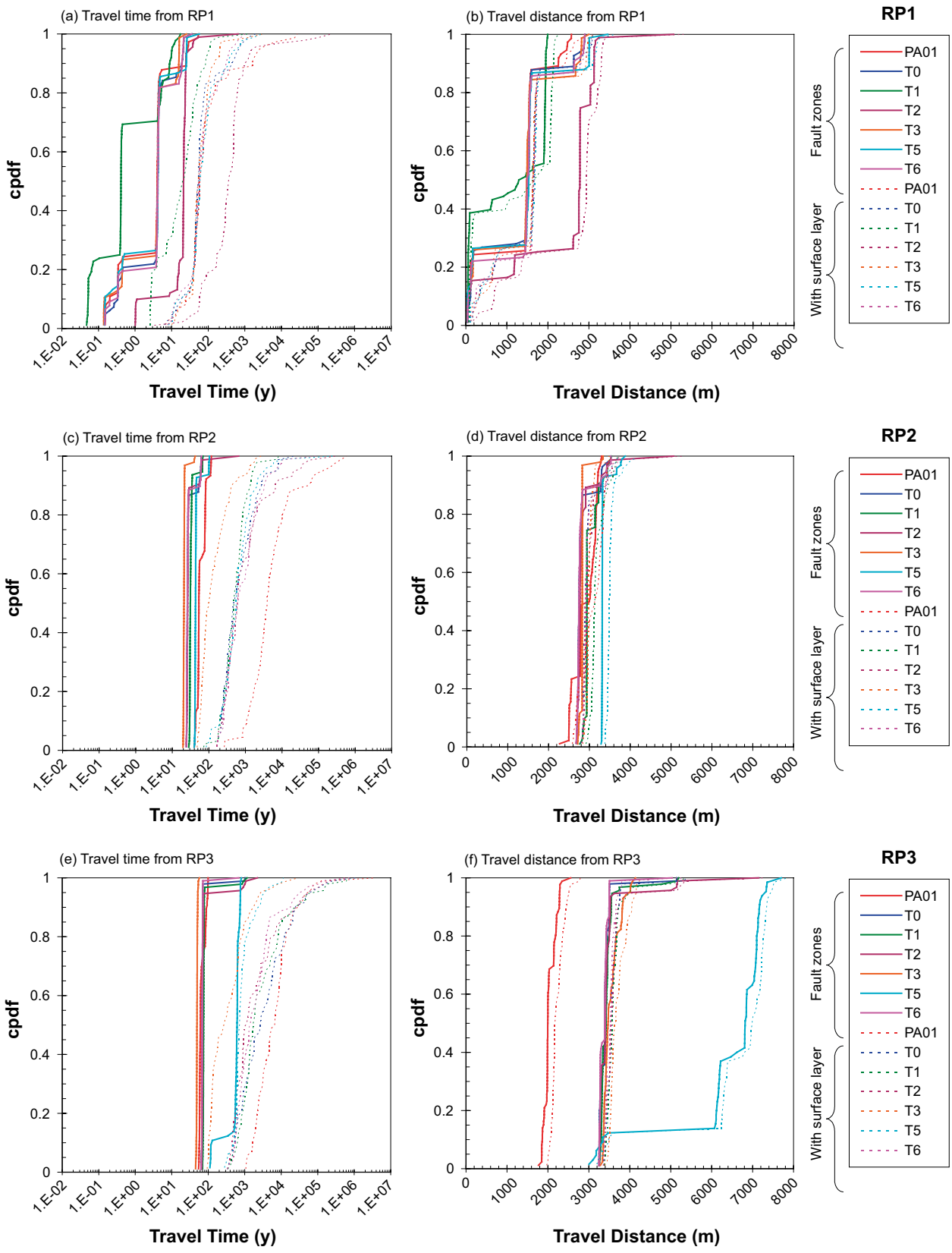

Figure 3-23. *Sensitivity analysis results of fault zone transmissivity onto particle travel time and travel distance.*

Conclusions from these simulations include the following:

1. Pathways from release point RP1 (Figures 3-23(a) and 3-23(b)) are strongly affected by the transmissivity of the HZ19 fault zone. Changes in fault transmissivity affect not only the velocity within the fault zones, but which zones are traversed by the pathways. For example, in the T4 case (illustrated in Figures 3-20 through 3-22) and the T6 case (lower transmissivity) pathways traverse many different zones (HZ19A, HZ19C, HZ20A, HZ20B_ALT, and HZ004). For the T1 fault properties (Figure 3-25), all pathways remained within the HZ19 fault zone.
2. As a result of the difference in travel pathways for release point RP1, mean travel times vary by approximately two orders of magnitude, and mean travel distances vary by a factor of two. These variations are of the order that could be significant for PA, and therefore indicate that it is important to know the transmissivity with sufficient accuracy to be able to distinguish for example between cases T2 and T1. However, the results of case SS03, SS04a and SS04b indicate that the open holes pumping and PFL tests were insufficient to distinguish between these fault zone transmissivity scenarios.
3. Results for release point RP2 (Figures 3-23(c) and 3-23(d)) indicate that the pathways from this point traverse the same basic set of fault zones, regardless of the different fault transmissivity scenarios. From release point RP2, the range of uncertainty in fault zone transmissivity represented by cases T1 through T4 does not result in significant variability in either advective travel time or advective travel length. The variability in advective travel time is driven rather by variability in the portion of the pathways within the surface EPM layers.
4. The sensitivity cases from RP2 show slightly shorter travel time where a larger transmissivity is assigned to the HZ20 fault zones when compared to the reference T4 case. The T3 case (higher transmissivity for HZ20 fault zones) has the shortest travel time.
5. Consequently, if release point RP2 accurately represented the situation at a repository, the reduction in uncertainty in fault zone transmissivity would be make only relatively small reductions in uncertainty in PA compared with other release point cases, as indicated by the uncertainty and variability of pathway travel time and length.
6. The travel time distribution for pathways from release point RP3 (Figure 3-23(e)) are similar to those for RP2, in that the variability or uncertainty in fault zones does not cause uncertainty and variability of travel time (and therefore, site characterization to reduce these uncertainties would not reduce the uncertainty of this aspect of PA).
7. The travel distance distribution results from release point RP3 (Figure 3-23(f)) are generally similar to the results for RP2, indicating that within a certain range, uncertainty in fault zone transmissivity causes only a small uncertainty in the travel distance. However, two cases (Cases T4 shown as PA01 and T5) have significantly different travel distances, indicating that for these fault transmissivity values, the pathways taken are indeed significantly different. RP3 pathways are shown in Figure 3-22 (Case T4 shown as PA01, higher transmissivity), Figure 3-26 (Case T5, higher transmissivity for HZ21 fault zone), and Figure 3-27 (Case T6, lower transmissivity for HZ21 fault zone). These pathways show three distinctive sets of pathways, each with a characteristic path length as shown in Figure 3-23(f). Based on this result, it could be concluded that while the travel time of Figure 3-23(e) is not sensitive to pathways, the uncertainty in transmissivity of pathways must be reduced at least sufficiently to distinguish which of the three characteristic pathways apply.

3.2 Task 7B – Block scale

3.2.1 Modelling approach

Task 7B considers a region of approximately 500 × 500 m surrounding boreholes KR14, KR15, KR16, KR17, and KR18 at the Olkiluoto site in Finland. The fundamental objectives of the task are as follows:

- Quantify the reduction of uncertainty in the properties of the fracture network.
- Assess the PFL data when analysing the rock mass and fractures.

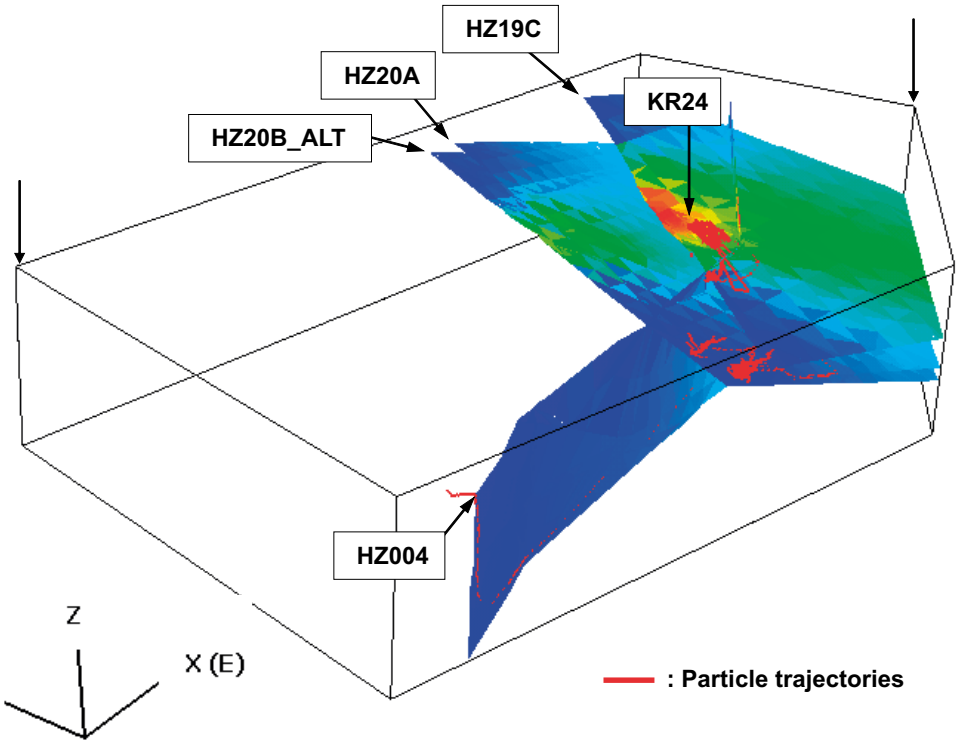

Figure 3-24. *Particle trajectories of from RP1 for sensitivity case T2 (lower transmissivity for HZ19 fault zones).*

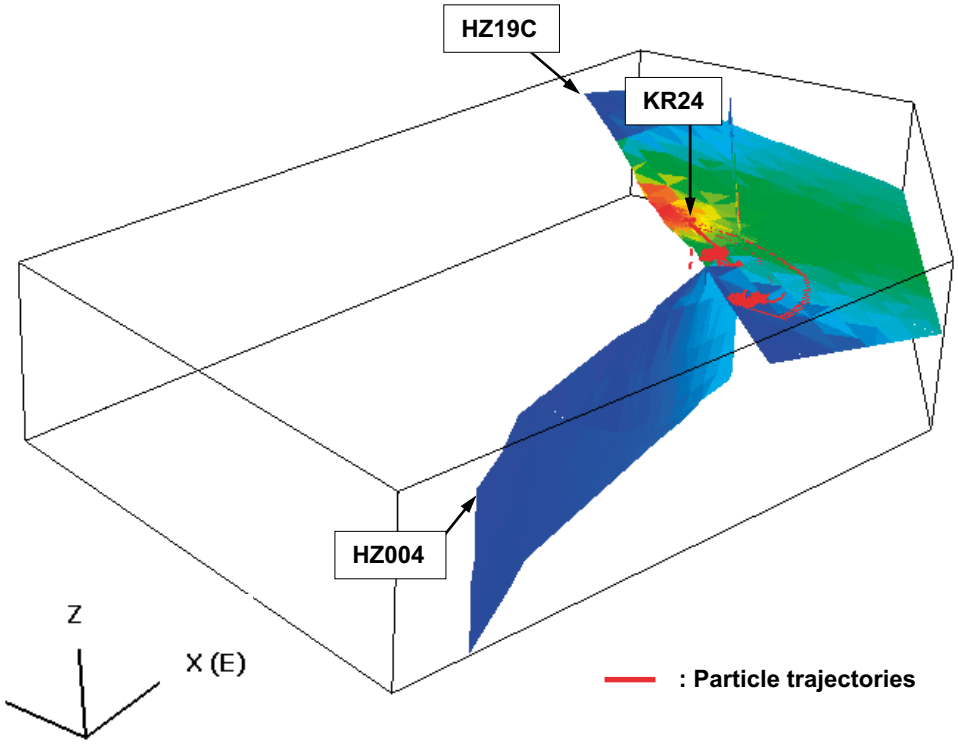

Figure 3-25. *Particle trajectories of from RP1 for sensitivity case T1 (higher transmissivity for HZ19 fault zones).*

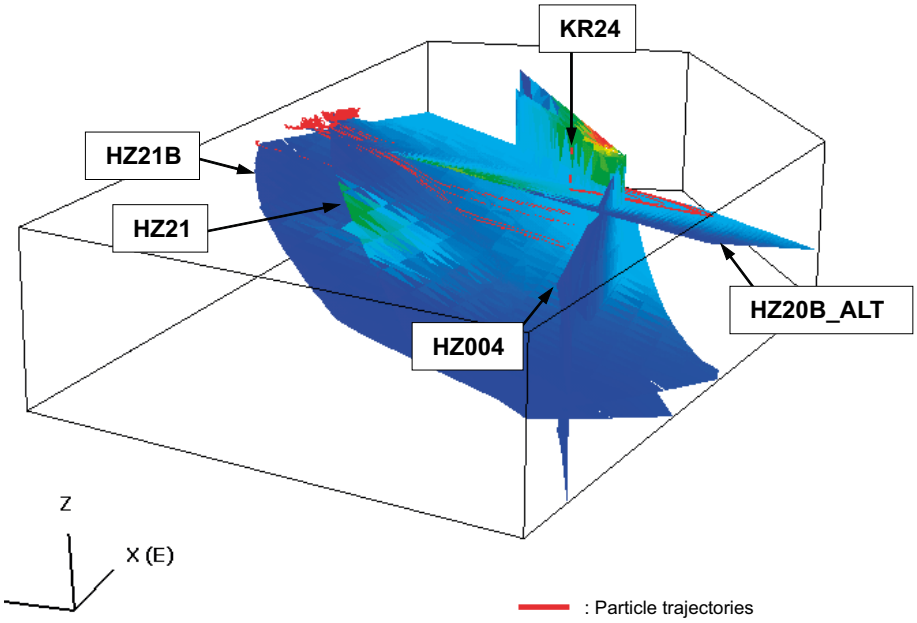

Figure 3-26. *Particle trajectories of from RP3 for sensitivity case T5 (higher transmissivity for HZ21 fault zones).*

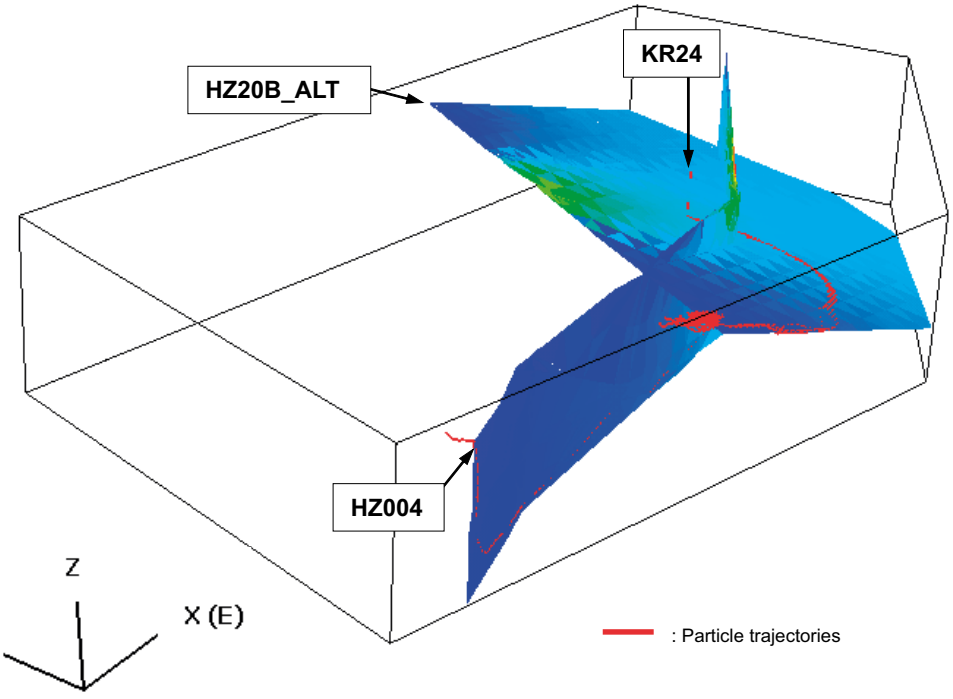

Figure 3-27. *Particle trajectories of from RP3 for sensitivity case T6 (lower transmissivity for HZ21 fault zones).*

The model was constructed by combining the following two elements:

- Larger structures such as major fault zones, modelled with a fixed (deterministic) geometry and calibrated hydraulic properties, and
- Background fractures, represented by a stochastic DFN.

The modelling approach for the larger structures is described below. This conceptualisation of the deterministic fault zone model was the first step in constructing the DFN model:

1 A deterministic fault zone model was derived based on interpretation of the transient cross hole interference test data. Pressure derivative plots of transient data were used to develop a "mapping" of transmissivity versus time and radial distance, and to identify the nature of fracture connectivity in terms of flow dimension (e.g, linear, cylindrical and spherical flow, and boundary effects).

2. The following three alternative models for the deterministic fault zone were constructed, by using the hydrogeological structural model provided:
   - 2006 model, which is the reference model used for Task 7A,
   - 2008 model, which is the reference model used for Task 7B, which is specified by Vidstrand et al. (2012) , provided by CAD format file, HZ-08_20080409.dxf and HZ-08_faces.dxf,
   - modified 2008 model, in which the fault zone HZ002 is added to the 2008 model, based on the deterministic fault zones model conceptualisation derived by the pressure derivative plot analysis.

   Comparisons were made among the three models for their consistency with the conceptualisation as above, and their plausibility.

3. The relative model plausibility was estimated using the residual sum of squared errors between measured data and simulated results, such as head along the boreholes and flow rate measured by PFL, normalized by number of compared points.

   A stochastic population of background fractures, represented by discrete features, was derived directly from PFL data. The following background fracture analyses were carried out.

4. Fracture orientation was analyzed to define sets and preferred orientations from flowing features identified in PFL within the model region.

5. Fracture transmissivity distribution was derived from PFL measurements.

6. Fracture size distributions were estimated from the correlation to transmissivity.

7. The spatial pattern of background fractures was also analysed by using the data of fracture intersection to the borehole identified in PFL.

3.2.2 Data usage and interpretation

Conceptualisation of deterministic fault zone model

The hydraulic interference tests conducted at KR14, KR15, KR16, KR17 and KR18 boreholes (Klockars et al. 2006) were analysed in order to understand the hydraulic properties and connectivity of faults and fractures. This analysis used derivative plots of transient pressure data to "map" the spatial pattern of hydraulic connectivity and boundary conditions. In this study, the following three sets of pressure interference test data were analyzed, as shown in Figure 3-28. The injected section and the target features are shown in Figure 3-29.

(a) Phase 3: injected from KR18 (53.5–59.5 m) targeted on the plane1.

(b) Phase 4: injected from KR17 (49–51 m) targeted on the plane1.

(c) Phase 4: KR17 (123.5–125.5 m) targeted on the plane3.

The locations of injection and observation sections in each borehole are summarised in Figure 3-30. Figure 3-31 shows an example of derivative analysis using the recovery phase after the injection test from KR18 (53.5–59.5 m) and its pressure responses to the observation sections in KR17. As the derivative value (Y-axis) is related to the transmissivity (Doe 2002, Enachescu et al. 2004), convergence of derivative plots in several test results on the same graph could provide the connectivity of fractures in the test section. The derivative value at the late time in the observation sections of L4, L5, L6 and BL1 in KR17 is similar to the value in injection section (Figure 3-31 and Figure 3-32a–c). This suggests that the water-conducting fractures (WCFs) in each observation section could be connected with that in the injection section (i.e., plane1). Based on this result, a WCF plane was interpolated between these observation sections and the injection section. Based

on these analyses, a model for the connectivity of deterministic flow features was conceptualised as shown in Figure 3-33. The HZ19C and HZ002 fault zones in the 2006 model (i.e., the model used for Task 7A) are not sufficiently conductive to reproduce the radial flow observed in the pressure interference test in the region between these fault zones in boreholes KR16, 17 and 18. The extent of this region is limited to the area around KR15 and KR 14. Only the narrow section at KR15 is connected to this region, and hydraulically no significant connection to KR14 was observed, as shown in Figure 3-33. This indicates the need to include a water conductive feature between the HZ19C and HZ002 fault zones. This feature could be a homogeneous, two dimensional planar feature, which is consistent with "unison" pressure response zone observed during the pressure response tests.

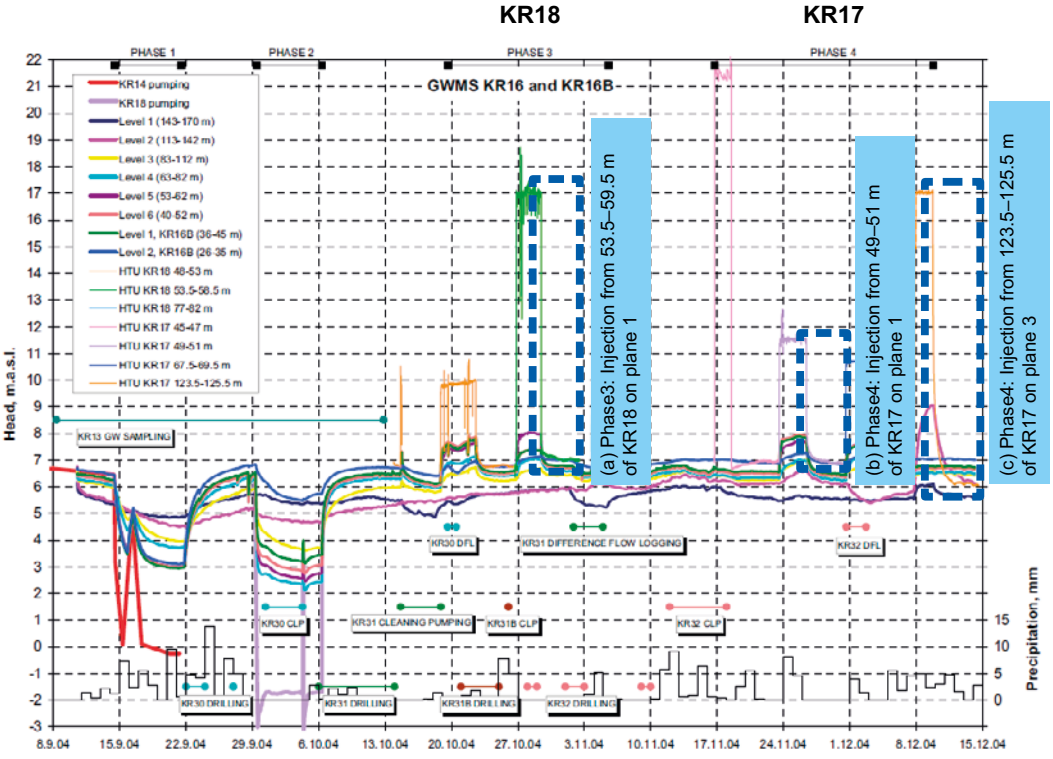

Figure 3-28. *Pressure recovery tests used for the derivative plot analysis (Klockars et al. 2006).*

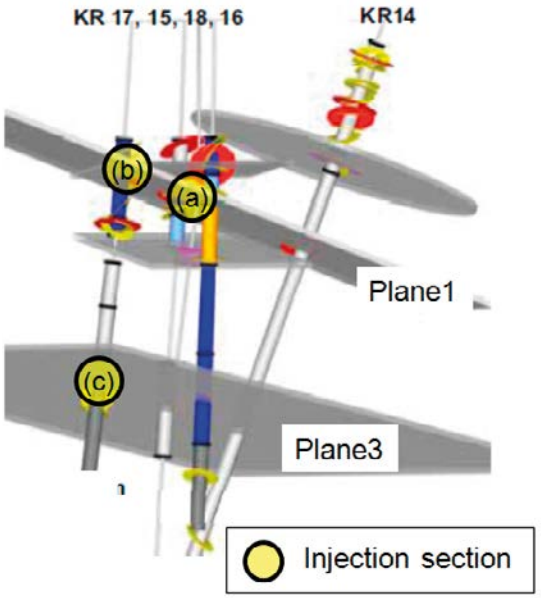

Figure 3-29. *Injection intervals and target features of pressure interference tests used for the derivative analyses (Klockars et al. 2006).*

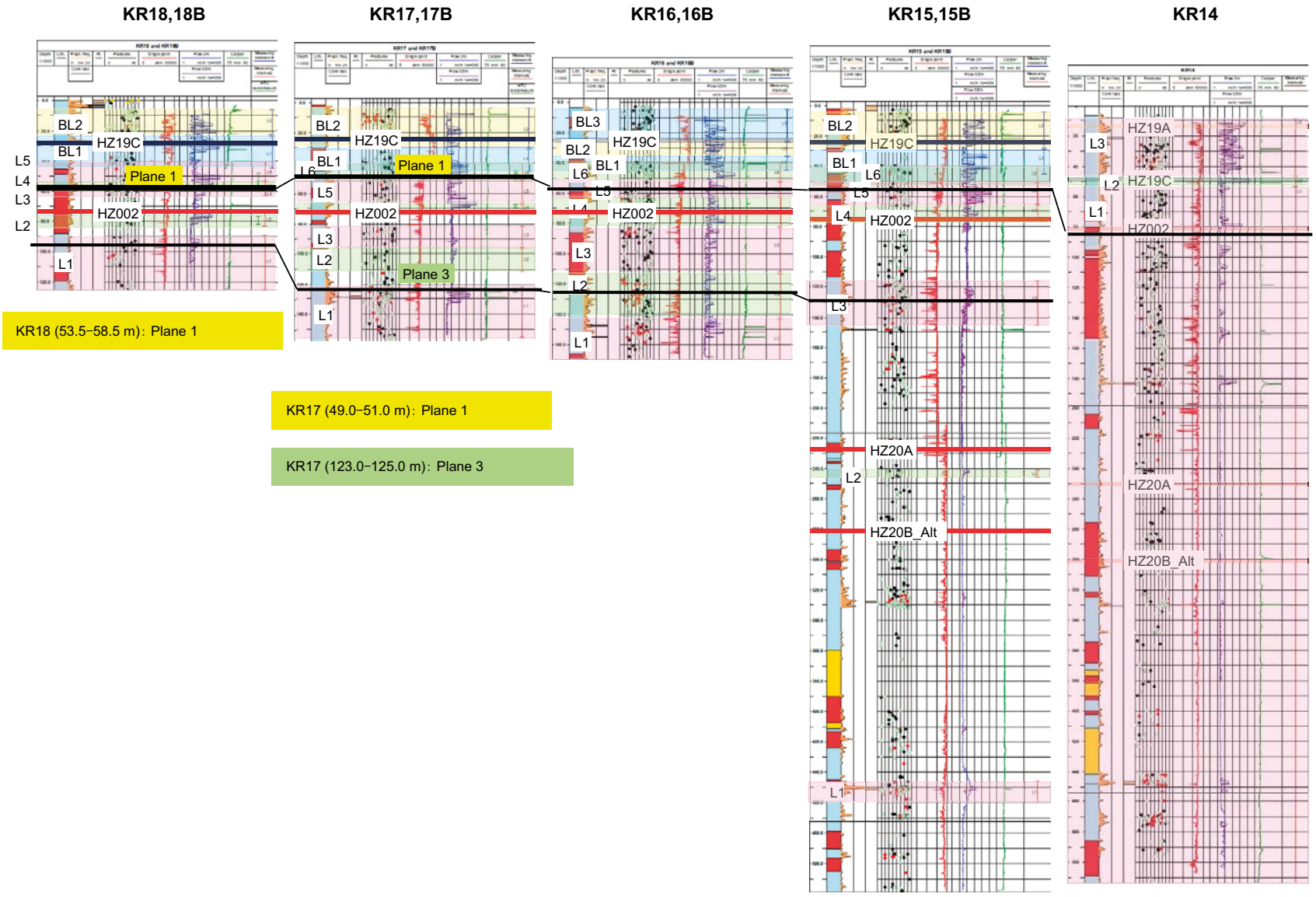

Figure 3-30. *Injection and observation sections. The injection section in each test are (a) 53.5–58.5 m in KR18 on plane1, (b) 49.0–51.0 m in KR17 on plane1 and (c)123.0–125.0 m in KR17 on plane3, respectively.*

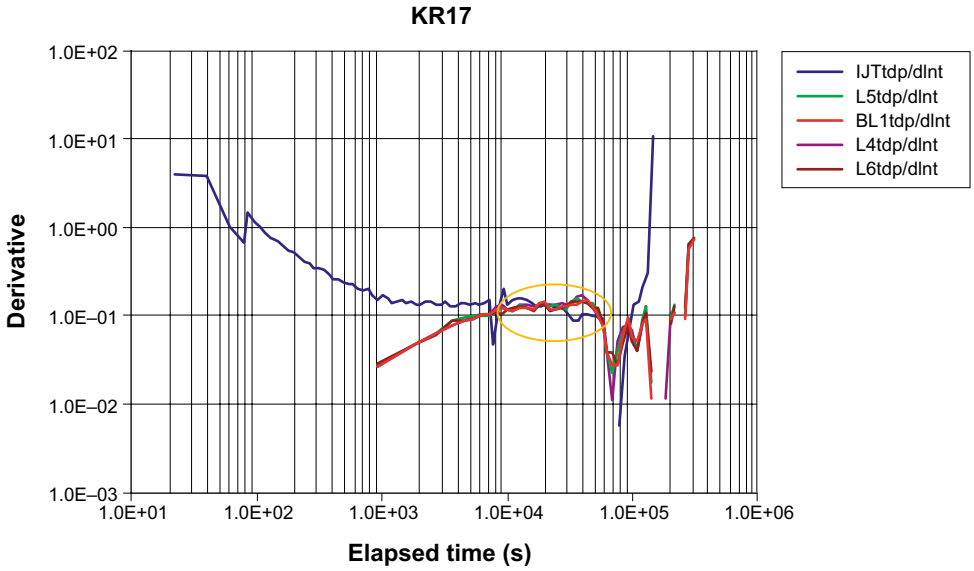

Figure 3-31. *An example of results of the derivative analysis.*

Figure 3-34 shows the comparison between the HZ19A and HZ19C fault zones included in the 2008 model (shown as red lines) and the conceptual model based on analysis of hydraulic interference tests. The HZ19C seems to represent the larger conductive feature estimated by the derivative plot analysis. In the 2008 model, the HZ002 has also been removed from 2006 model. However, some form of structure similar to HZ002 needs to be considered to provide observed connectivity at the depth of 70–80 meters. Therefore, the third alternative model (the modified 2008 model in which fault zone HZ002 was added to the 2008 model) was proposed to reproduce the conceptual model derived by derivative plot analyses of pressure interference tests.

Model plausibility analysis among the three alternative models

Three alternative conceptual models for deterministic faults are shown in Figure 3-35, (a) reference model used for Task 7A: "2006 model", (b) reference model used for Task 7B: "2008 model" and (c) modified 2008 model, incorporating HZ002. This analysis was carried out using the simplified boundary condition as described in Figure 3-36. The transmissivity of each fault zone was set as geometrical mean value as specified by Vidstrand et al. (2012).

The alternative conceptual models were evaluated by carrying out steady state flow simulations for two situations (without pumping and with pumping) for a series of the pressure interference tests, and comparing with flow response data and pressure response data. The relative model plausibility was estimated using the residual sum of squares (RSS) normalized by number of compared points as:

$$\frac{\sum(measured - simulated)^2}{n-1} \qquad 3\text{-}1$$

Figure 3-37 shows the pressure response (drawdown) during (a) phase 1 pumping from KR14 and (b) phase 2 pumping from KR18, for each alternative model. Figure 3-38 summarises the RSS of the simulation results for the 2006 model, 2008 model, and modified 2008 model. The height of the column represents the residual sum of squared errors normalized by number of compared points. According to this measure, the 2008 model provides the best match to measurements in case of (a) phase 1, (d) phase 3-2 and (g) sum of total, since it has the lowest residual error. The "n" count provided on each column represents number of compared in situ measurements points along the boreholes matched by the model. According to this measure, the modified 2008 model could be the preferred model, because it shows relatively small RSS values although it includes structures at a larger number of locations such that 58 in situ measurements can be compared. Neither the 2006 model (27 measurements) nor the 2008 model (29 measurements) includes a comparable number of connections to the measured boreholes.

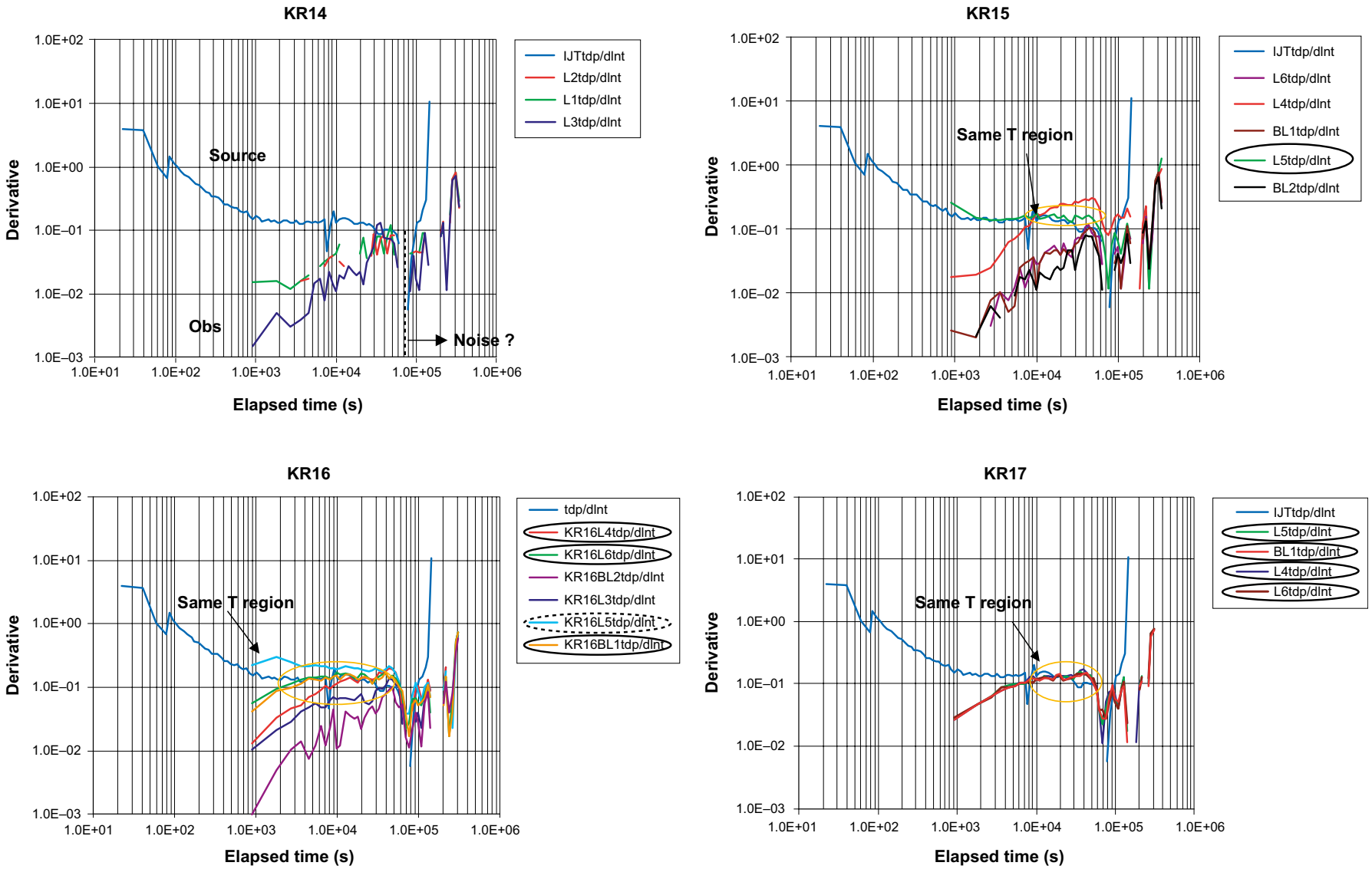

Figure 3-32a. *Results of the derivative analysis. Response in each observation section to the injection from KR18 (53.5–59.5 m).*

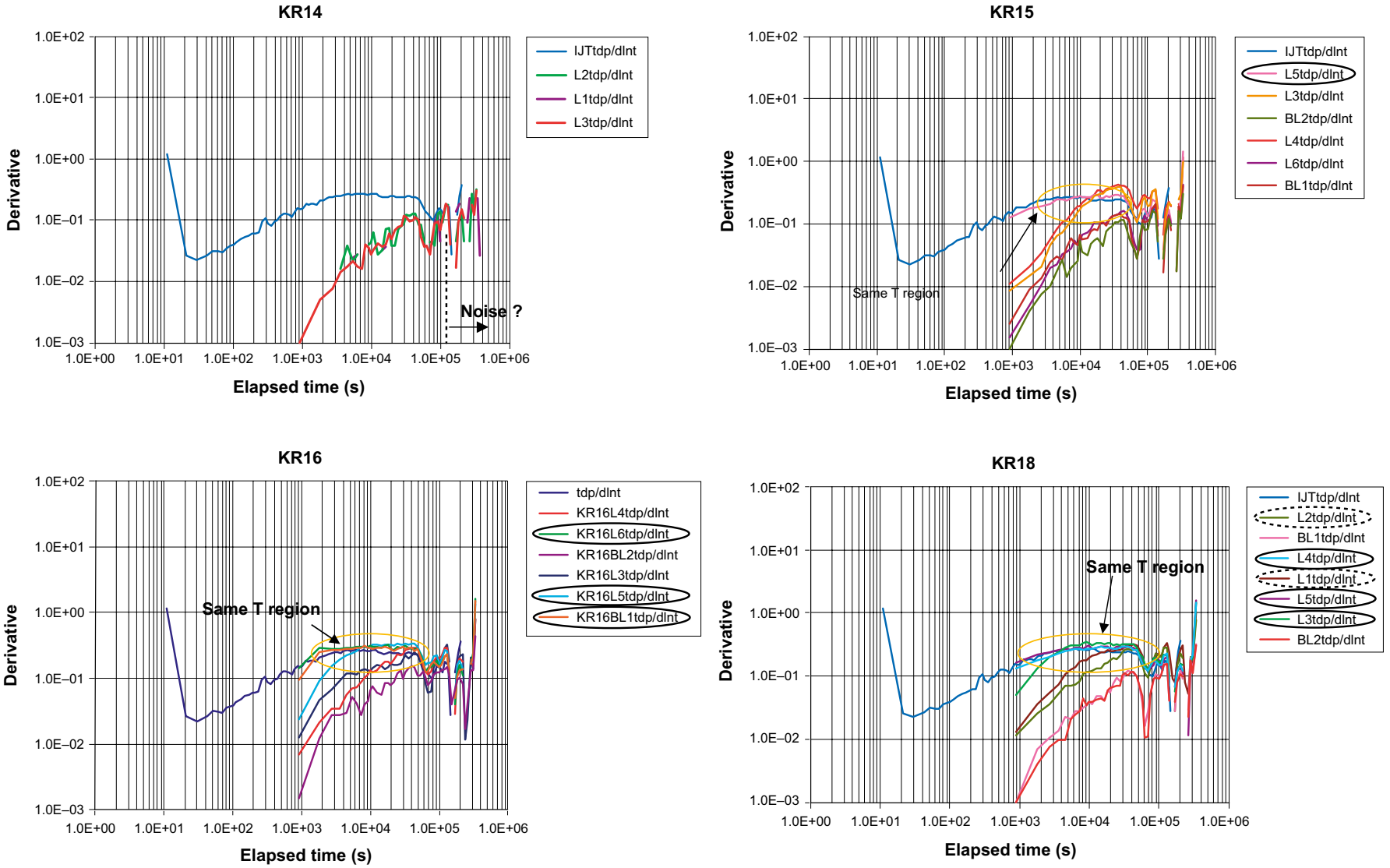

Figure 3-32b. *Results of the derivative analysis. Response in each observation section to the injection from KR17 (49–51 m).*

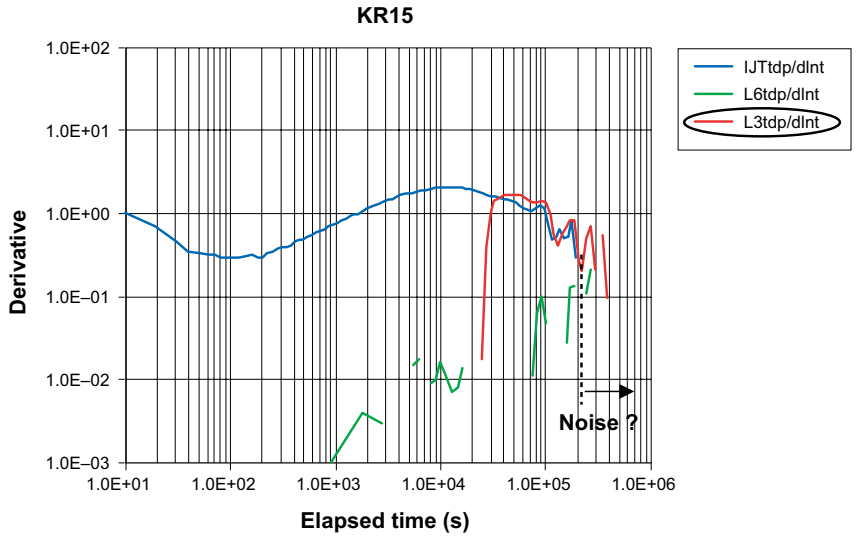

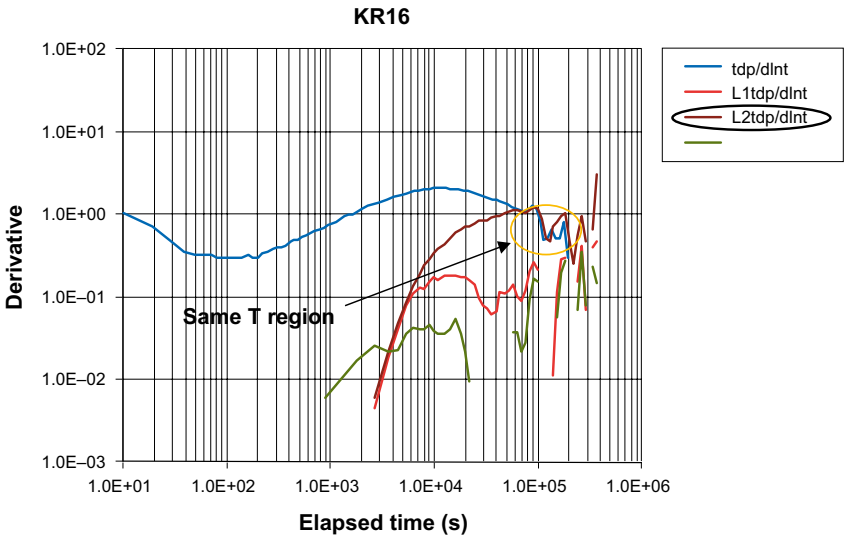

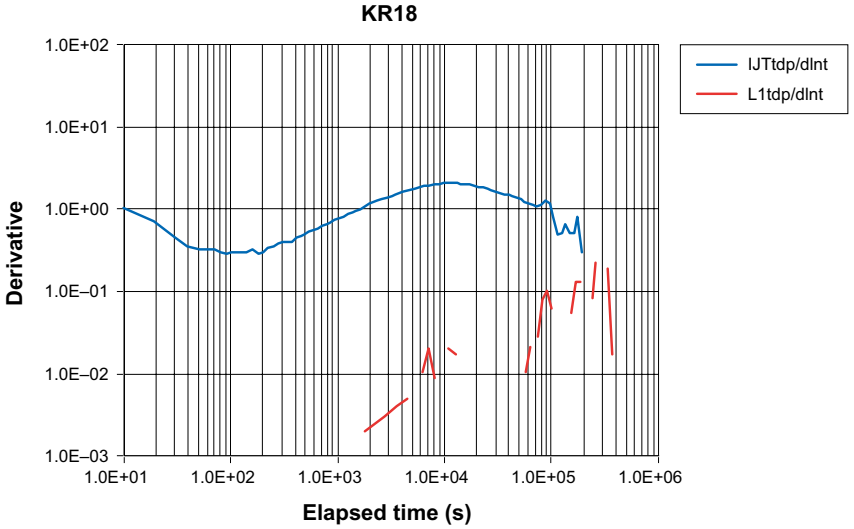

Figure 3-32c. *Results of the derivative analysis. Response in each observation section to the injection from KR17 (123.5–125.5 m).*

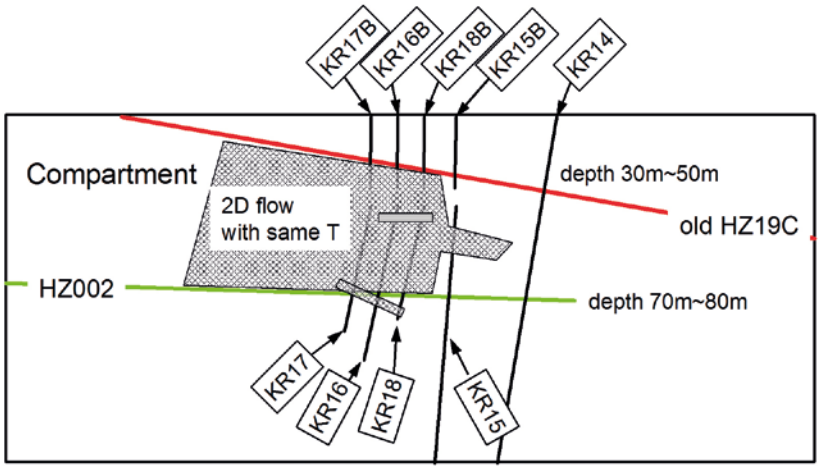

Figure 3-33. *Hydrostructural model based on analysis of hydraulic interference data. "Old" HZ19C and HZ002 are faults zone used in the Task 7A reference model.*

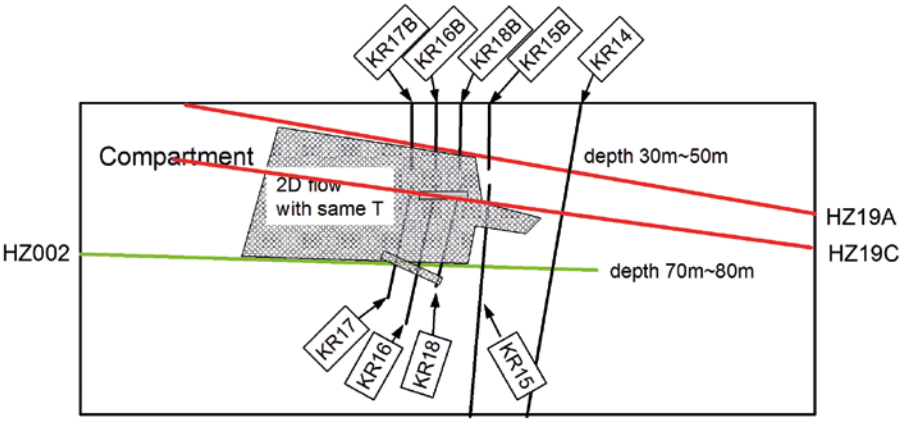

Figure 3-34. *Comparison between HZ19A, C fault zones included in 2008 model (shown red lines) and the conceptual model based on analysis of hydraulic interference tests. In 2008 model, HZ002 was removed from the 2006 model. In order to provide connectivity observed at the depth of 70–80 m, HZ002 or similar zones need to be added.*

Background fractures analysis

The population of background fractures among the fault zones was estimated from a statistical analysis of the dataset of water conducting fractures identified in boreholes KR14–18 by PFL. Because the focus of Task 7B is above fault zone HZ20A, data below HZ20A at each borehole was eliminated from this analysis.

Table 3-6 summarises the derived parameters for the population of background water conducting fractures. Volumetric fracture intensity P_{32} was estimated from one dimensional intensity of water conducting fractures measured by PFL using the analytical approach (Wang 2005). Fracture orientation data for water conducting fractures was fitted to a Fisher distribution using procedures described in Dershowitz et al. (2007). Fracture transmissivity data obtained by PFL could be fitted to lognormal distribution. In this study, the minimum values shown in dataset in which maximum and minimum values were estimated as one of uncertain range, were chosen to fit the lognormal distribution (Figure 3-39). Because there are no fracture size data measured for each water conductive fracture, the following empirical correlation found in Task 6C between transmissivity, T, and size, L, is used for estimating the size distribution (Dershowitz et al. 2003).

$$T = 5 \cdot 10^{-10} \cdot L^{1.386} \qquad 3\text{-}2$$

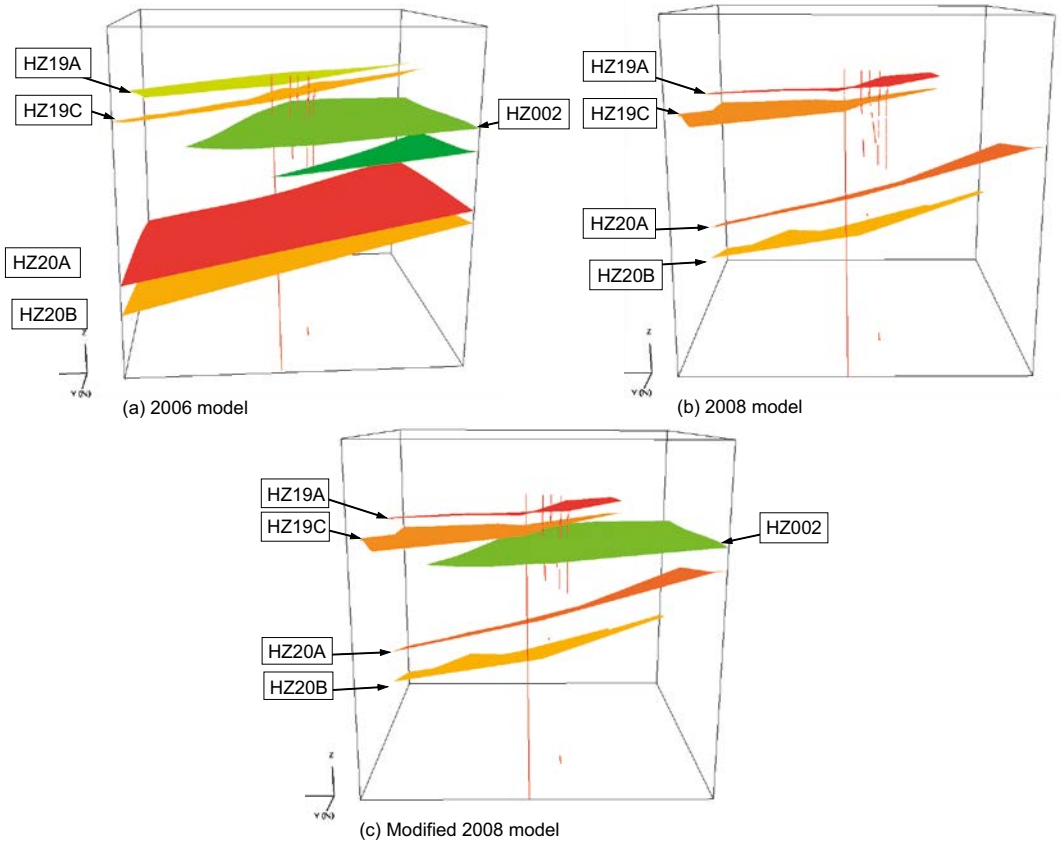

Figure 3-35. *Three alternative fault hydrostructural models evaluated in Task 7B.*

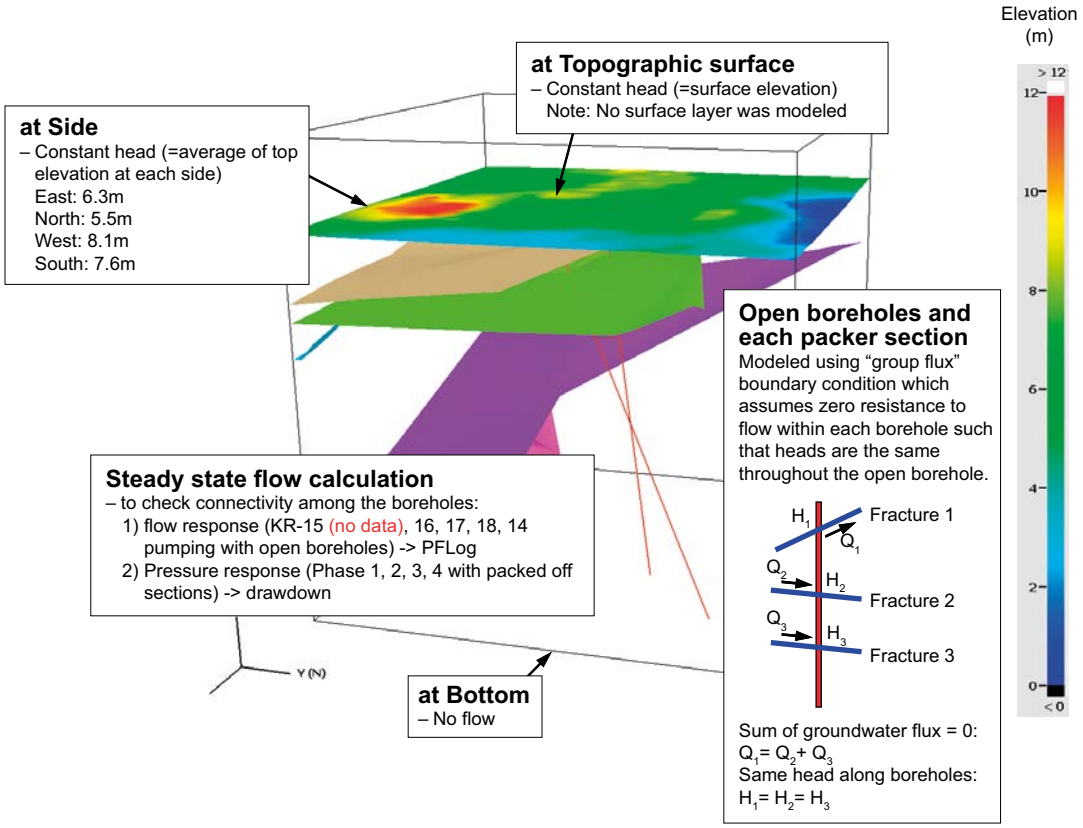

Figure 3-36. *Boundary conditions and model assumptions used for the model plausibility analysis to evaluate the effect of local fault geometry.*

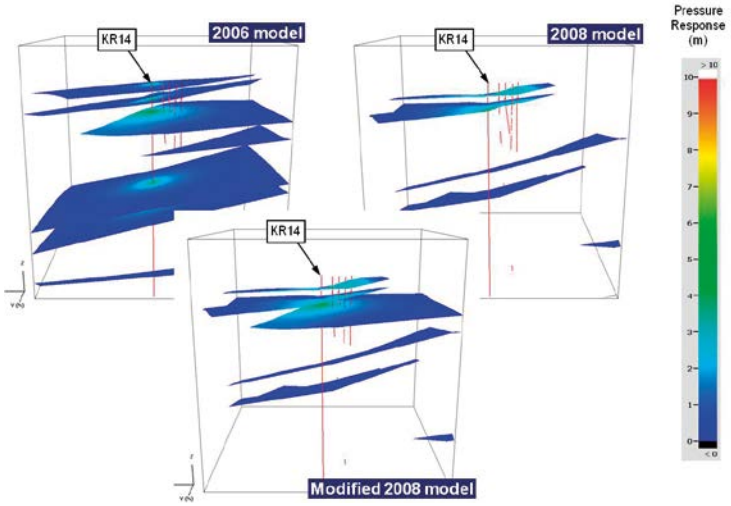

(a) Pressure response during Phase 1 (KR14 pumping)

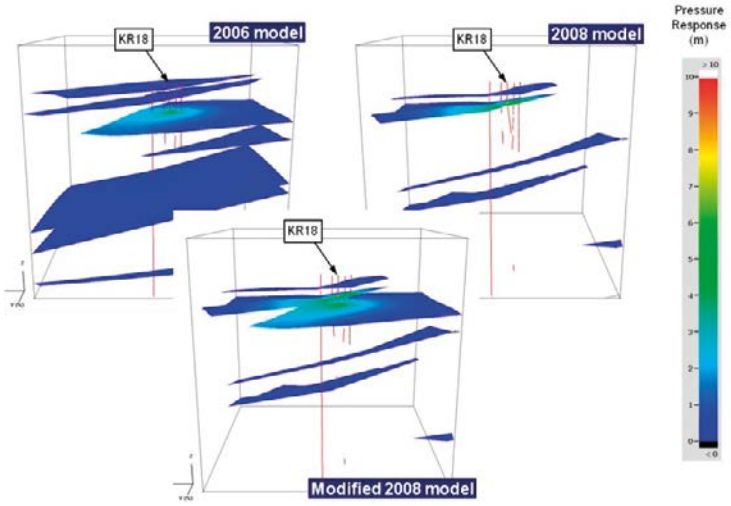

(b) Pressure response during Phase 2 (KR18 pumping)

Figure 3-37. *Simulated results for the model plausibility analyses, shown by pressure response (drawdown).*

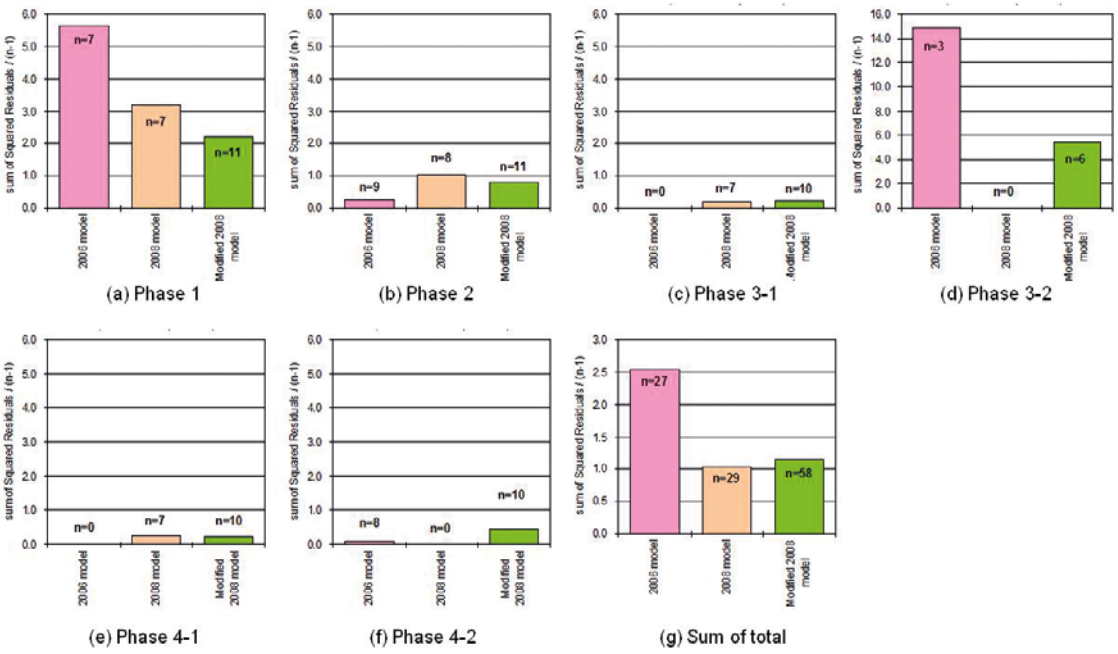

Figure 3-38. *Evaluated results of the model plausibility analyses, at each pumping case (a)–(f) and sum of all cases (g).*

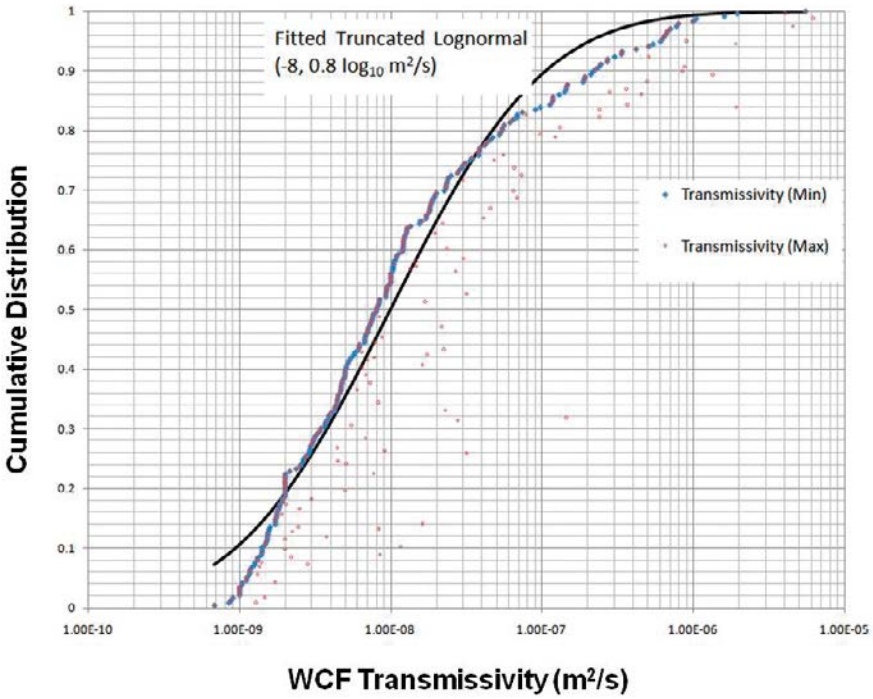

Figure 3-39. *Transmissivity distribution fitted to measured data (minimum values).*

A major purpose of Task 7B is to improve the understanding of uncertainty. This study focused on the uncertainly related to alternative stochastic realizations of the background fracture population. Figure 3-40 shows an average hydraulic conductivity in a 500 m scale of model block for each of five realizations, in each direction. Horizontal hydraulic conductivity seems to be twice the vertical conductivity. Average hydraulic conductivity of background fractured rock by the DFN is consistently 2–10 times larger than the reference value of 10^{-9} m/s.

Table 3-6. Summary of background fracture parameterization.

Parameter	Value	Remarks
Fracture intensity, P32 estimated by Wang (2005)	0.3 m^2/m^3	Assumes Fisher distribution
Intensity, P10	0.23	Calculated from water conducting fractures, identified by PFL
Wang conversion factor	1.3	
Orientation (pole, Fisher distribution) trend, plunge	229, 78	
Fisher k	4.7	Fisher K-S goodness of fit =74%
Transmissivity (Lognormal distribution)		
Mean, Standard deviation	–8, 0.8	Common logarithm
Size, L (Lognormal distribution)		
Mean, Standard deviation	31 m, 67 m	L is correlated to transmissivity T (Dershowitz et al. 2003)
		$T = 5 \cdot 10^{-10} \cdot L^{1.386}$

3.2.3 Geometrical description

The modelling region has a 500 m × 500 m × 500 m cubic volume, centred on borehole KR15. Figure 3-41 shows the deterministic fault zone model, which is the most plausible among the three alternative models as discussed above, and an example realization of the background fractures.

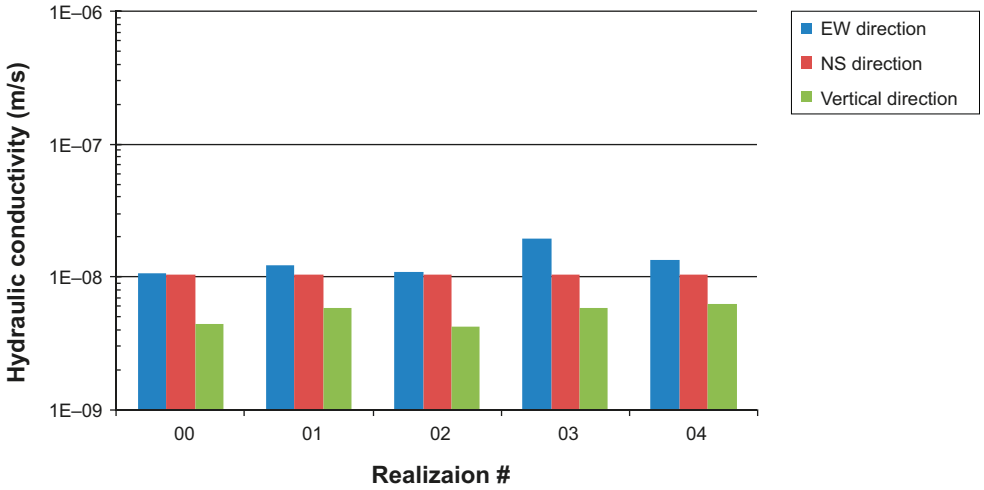

Figure 3-40. *Average hydraulic conductivity of background fracture rock at 500 m × 500 m × 500 m scale, five realization results.*

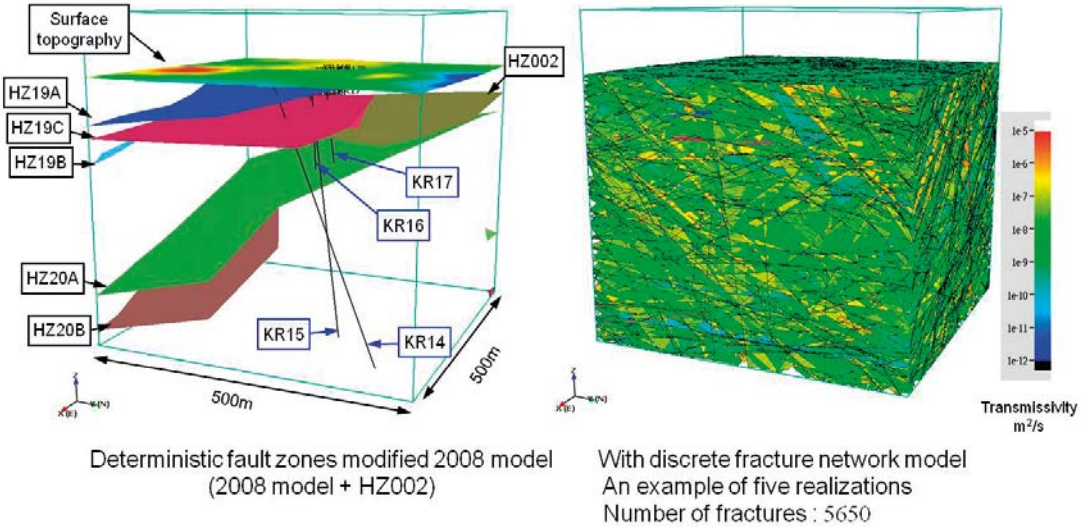

Figure 3-41. *The deterministic fault zones model, modified 2008, and an example of background fracture network model generated in the modelling region, 500 m × 500 m × 500 m.*

3.2.4 Processes considered

Task 7B was simulated assuming a steady state condition on Darcy's flow law through the deterministic fault zones and a background fracture network model. All fluids were assumed to be fresh water, with a constant density of 1 g/cc and a temperature of 20°C.

3.2.5 Boundary and initial conditions

The same boundary conditions illustrated in Figure 3-36 and used for the conceptualisation of the deterministic fault zone were applied. At the side boundaries, constant head was used, which is set as the average of top elevation at each side. The top boundary was also assumed to be a constant head, which is defined by the elevation of the topographic surface. Open boreholes and each packer section were modelled by using "group flux" boundary condition, the same as is shown in Figure 3-4, which assumes zero resistance to flow within each borehole such that heads are the same through the open borehole.

3.2.6 Numerical model

Modelling of Olkiluoto for Task 7B was also carried out using FracMan (Dershowitz et al. 2007; www.fracman.com).

3.2.7 Parameters

The material properties assumed in this study are listed in Table 3-7, which are based on the specifications (Vidstrand et al. 2012). For the background fractures, the parameters are described in Table 3-6. Transmissivity of each fault zone was also specified as a single value per fault zone. Transport aperture is calculated from transmissivity using the empirical equation $e_t = a\ T^b$, where a=2, and b=0.5 (Sawada et al. 2000). In this modelling study, only the steady state flow conditions were considered. The storativity values for each fracture and fault zone are not defined.

Table 3-7. Material property assumptions (Vidstrand et al. 2012).

Property	Assumption	
Fault Zone Transmissivity	Fault zone name	Log of transmissivity (m^2/s)
	HZ19A	–5.1
	HZ19B	–5.5
	HZ19C	–5.4
	HZ20A	–5.3
	HZ20B	–5.5
Fracture Zone Transport Aperture	$e_t = aT^b$, where a=2, and b=0.5	

3.2.8 Model conditioning and calibration

Table 3-8 shows the simulation cases specified in Vidstrand et al. (2012). In this study, based on the simplified boundary conditions and limited number, five realizations of the background fracture model were examined. This might cause certain level of errors in estimating head distribution as absolute values. Although it is important to estimate head distribution to demonstrate the model confidence, head is significantly affected by the boundary conditions. Therefore, in this study we have been focusing on the examination of the flow connectivity among the boreholes by comparing pressure response (drawdown) and flow response, rather than comparing head, with measured data. The pressure response and flow response simulation results, as well as the model calibration processes, are discussed below.

Table 3-8. Task 7B simulations cases as specified in Vidstrand et al. (2012).

Name	Description	Boreholes	Purpose
SS20a	“Natural conditions”	No boreholes	Forward
SS21	“Natural conditions”	Boreholes are open and free to cross-flow	Calibration
SS22	“Natural conditions”	Boreholes are packed-off	Calibration
SS20b	“Natural conditions”	No boreholes	Based on calibrated models after SS21 & SS22
PA20c	“PA conditions”	No boreholes	Forward
SS23a	Pumping in KR14	Boreholes are open and free to cross-flow	Forward (followed by …)
SS23b	Pumping in KR14	Boreholes are open and free to cross-flow	Calibration
SS24a	Pumping in KR14	Boreholes are packed-off	Forward (followed by …)
SS24b	Pumping in KR14	Boreholes are packed-off	Calibration
SS25a	Pumping in KR18	Boreholes are open and free to cross-flow	Forward (followed by …)
SS25b	Pumping in KR18	Boreholes are open and free to cross-flow	Calibration
SS26a	Pumping in KR18	Boreholes are packed-off	Forward (followed by …)
SS26b	Pumping in KR18	Boreholes are packed-off	Calibration
TS27	Pumping in KR15	Boreholes are open and free to cross-flow	Forward
TS28	Pumping in KR14	Boreholes are open and free to cross-flow except for one isolated flowing structures in other boreholes*	Forward
PA29	“PA conditions”	No boreholes	Calibration

Pressure Response

Figure 3-42 and 3-43 show the comparison between simulated and measured drawdown during KR-14 pumping and KR-18 pumping cases, respectively. At the pumping boreholes, the constant flow rate pumping, 25 L/min. at KR-14 and 6 L/min. at KR-18 were applied. These cases correspond to SS24a and SS25a simulation cases listed in Table 3-8.

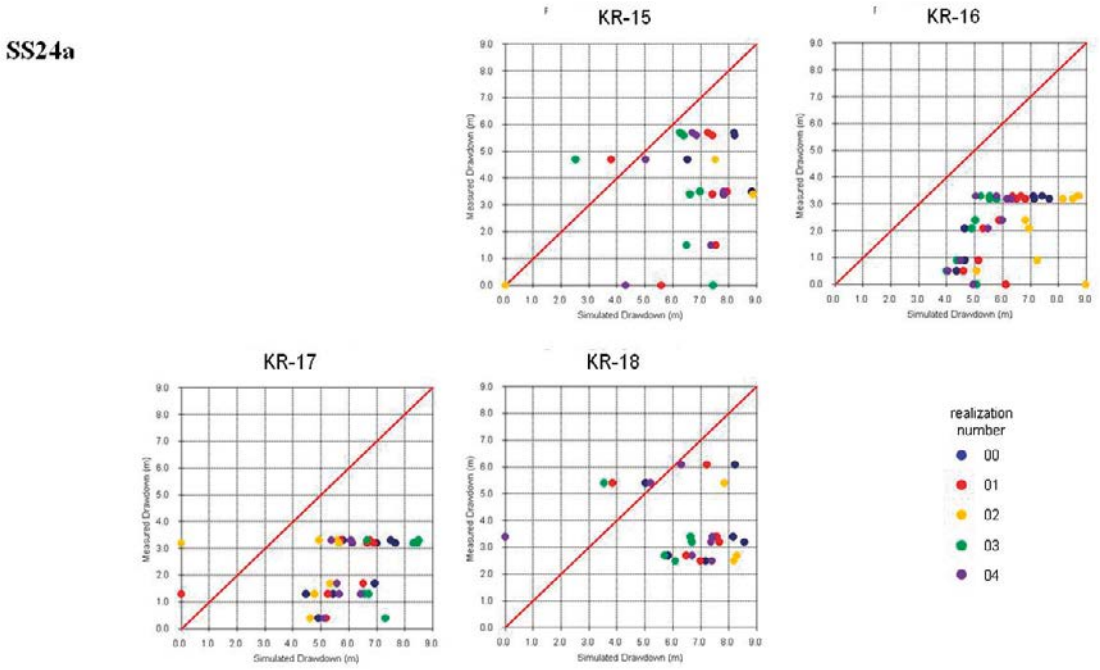

Figure 3-42. *Comparison between simulated (x-axes) and measured (y-axes) drawdown during KR-14 pumping (25 L/min.), which is case SS24a listed in Table 3-8.*

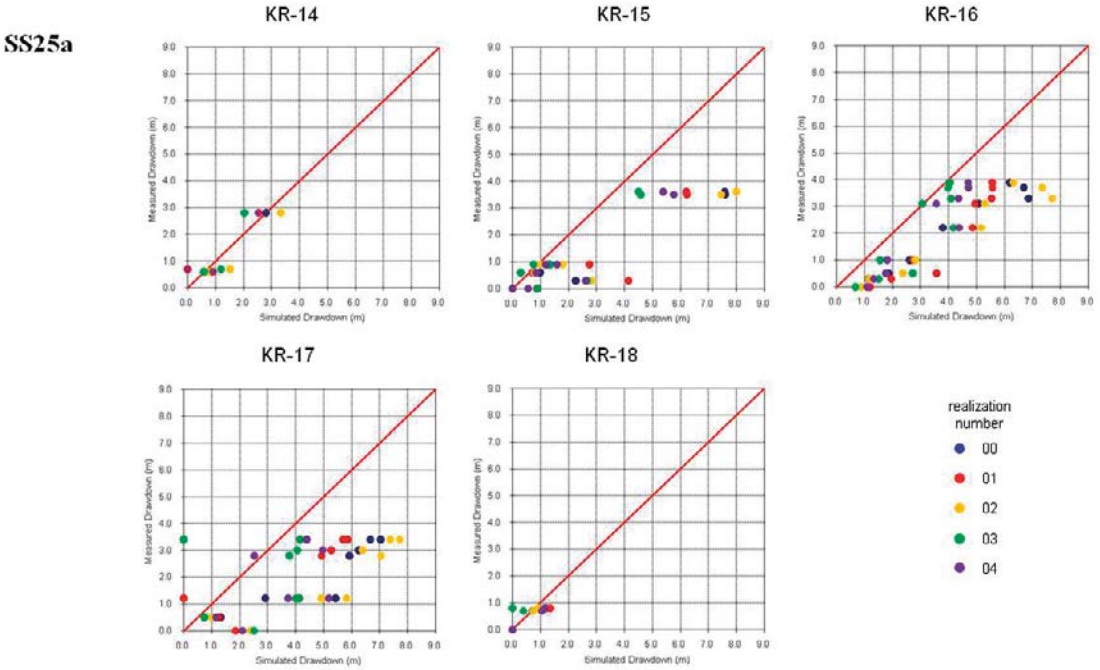

Figure 3-43. *Comparison between simulated (x-axes) and measured (y-axes) drawdown during KR-18 pumping (6 L/min.), which is case SS25a listed in Table 3-8.*

In this study, pressure response is examined using drawdown (change of head due to pumping) rather than the value of head itself. The simulated drawdown shown in Figure 3-42 and 3-43 tends to be larger than the measured drawdown. When the boundary condition at the pumping borehole is changed from a constant pumping flow rate as specified, to a constant drawdown as measured, the simulated pressure response is closer to the measured value as shown in Figure 3-44 and 3-45, which are the simulated pressure responses in case of applying a constant drawdown condition at the pumping boreholes instead of constant flow rate as specified in order to achieve measured drawdown at pumping borehole. This indicates that the lesser hydraulic conductivity among the boreholes might be required as one of the options for the model calibration.

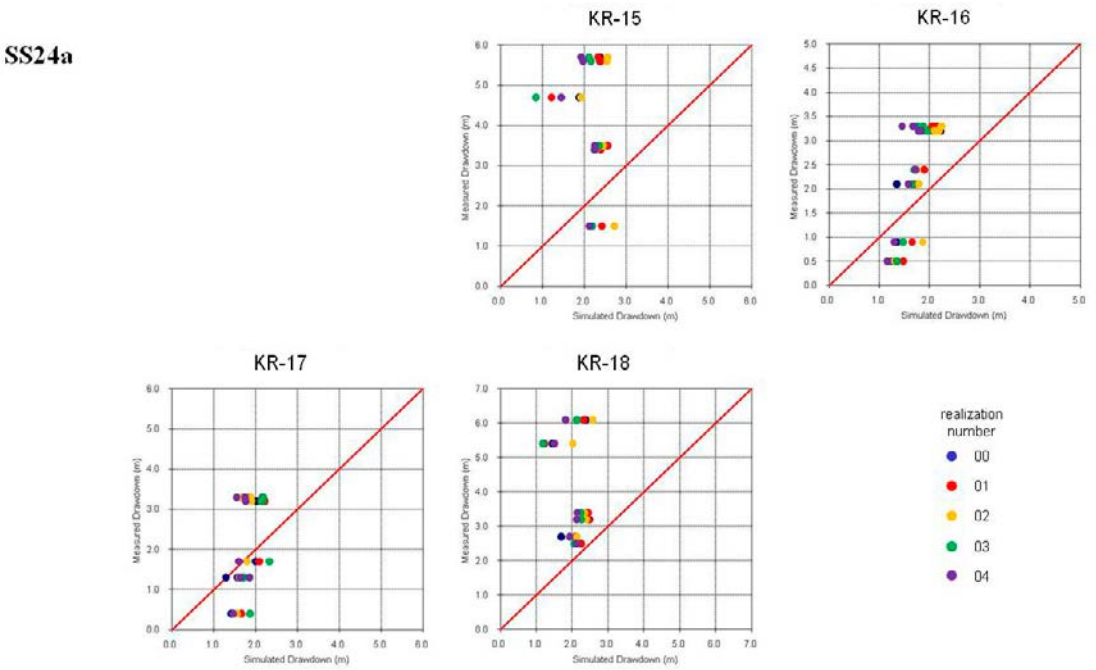

Figure 3-44. *Comparison between simulated (x-axes) and measured (y-axes) drawdown during KR-14 pumping (constant head boundary to archive 6.8 m drawdown), which is case SS24a listed in Table 3-8.*

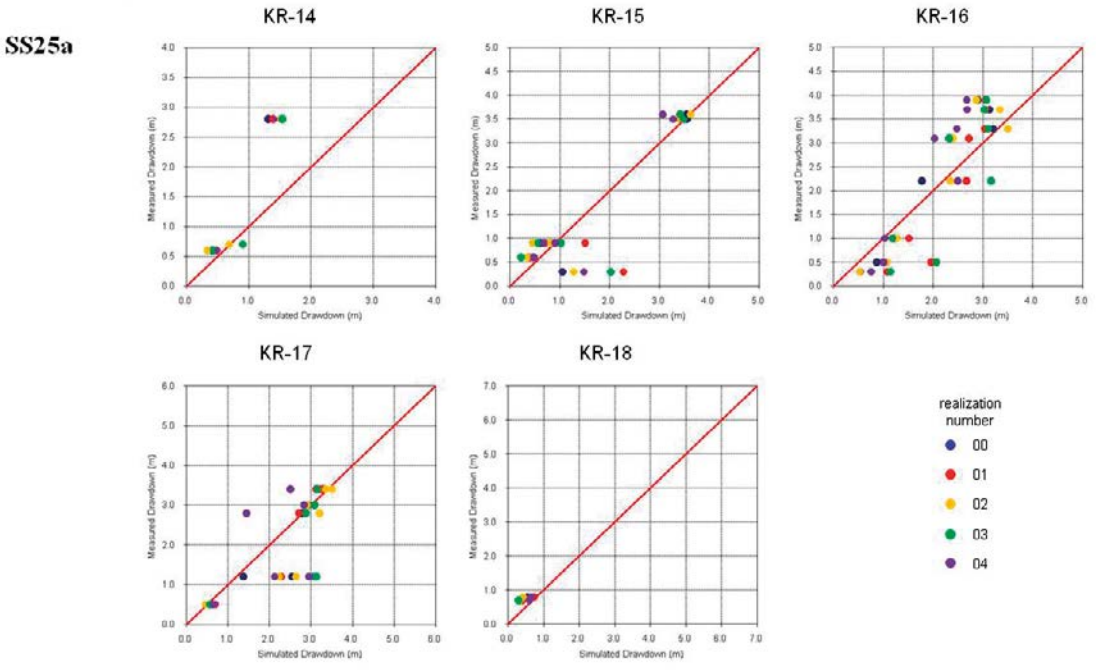

Figure 3-45. *Comparison between simulated (x-axes) and measured (y-axes) drawdown during KR-18 pumping (constant head boundary to archive 8.1 m drawdown), which is case SS25a listed in Table 3-8.*

Figures 3-46 and 3-47 show the simulated flow response, which is calculated from the PFL flow rate during pumping phase minus the steady stable flow rate, compared with the measured flow response. From these figures, the major flow response along the boreholes can be reproduced except for the "B" series boreholes, which penetrated to shallow surface layer up to about 50 m from the surface, where fracture density and hydraulic conductivity might be higher than the deeper zone. In addition, simulations are able to reproduce the major flow responses; however, the match is better without the stochastic background fracture population. The background fracture network model tends to cause the model to over-estimate hydraulic responses. This is because that the density of background fracture population is based directly on PFL measurements (Table 3-6) and the deterministic fault zones are added to the model without adjusting total fracture density P_{32}, which might be one of potential calibration options. In addition, stochastic variability among the five realizations causes certain changes of flow response between the deterministic fault zones, which might be one of challenges to constraining stochastic model by data at each measured location.

Figures 3-48 and 3-49 present the normalized RSS for cases SS24a and SS25a. The drawdown at the observation borehole is closer in the case of pumping by constant head to achieve the drawdown measured at pumping well, as discussed above. Thus, the error of this case is smaller than that for the constant flow rate pumping case. These values were used for one of the performance measures in the processes of calibrating the model as described below.

Model calibration

The model was modified by adjusting the hydraulic connectivity between the boreholes and the DFN model being composed of the deterministic fault zones (modified 2008 model) and the background fractures. The modifications were performed by 1) removing background fractures below HZ20A to avoid hydraulic connectivity from KR14 and KR15 at deeper zone, and 2) by disconnecting between KR14 and HZ002, HZ19C to be consistent with major fault zone model derived by the derivative analysis based on crosshole interference test. In addition, model calibrations were examined based on the following two points of view.

1. Calibrate the parameters that control an average hydraulic characteristic.
2. Calibrate the parameters that control heterogeneous flow connectivity of the DFN model.

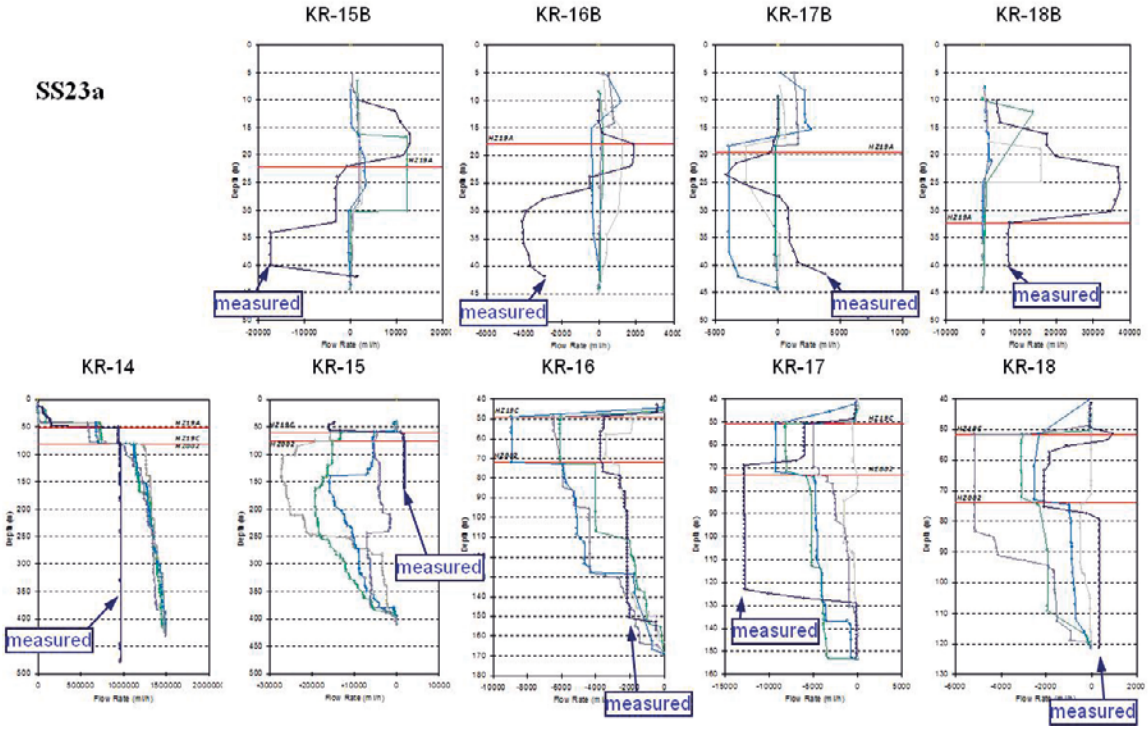

Figure 3-46. *Flow response, PFL flow rate during pumping phase minus flow rate during steady state, compared with the measured value during KR-14 pumping (25 L/min.), which is case SS24a listed in Table 3-8.*

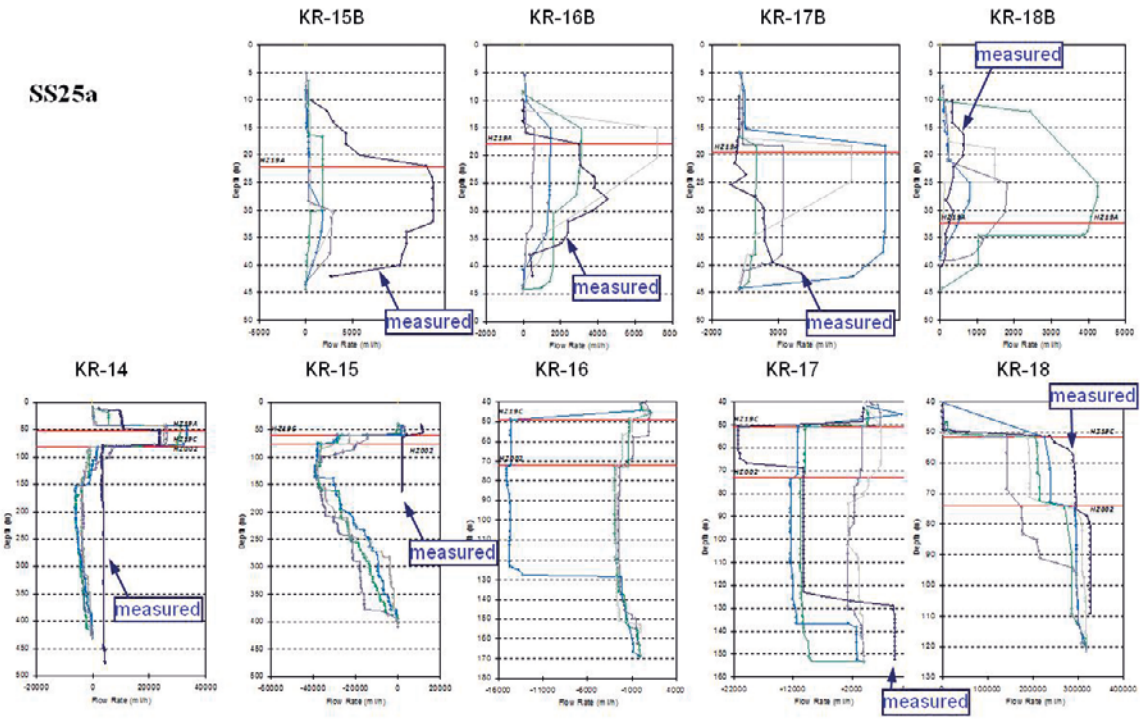

Figure 3-47. *Flow response, PFL flow rate during pumping phase minus flow rate during steady state, compared with the measured value during KR-18 pumping (6 L/min.), which is case SS25a listed in Table 3-8.*

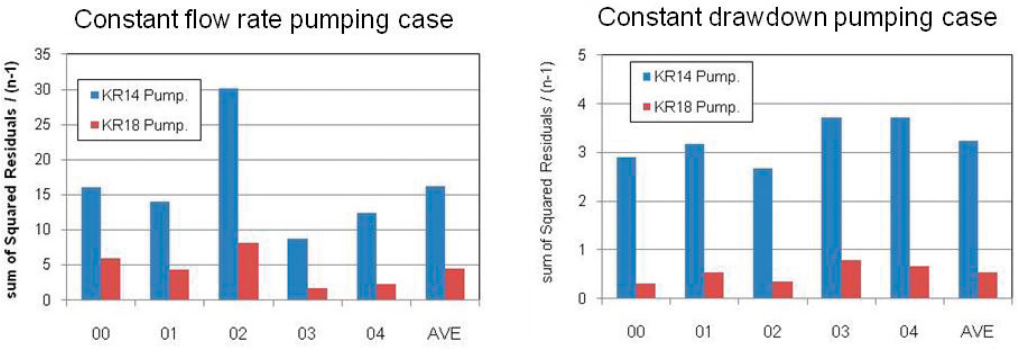

Figure 3-48. *Model plausibility evaluated by normalized RSS based on the pressure responses simulations at each realization (00–04); left: constant flow rate pumping case, right: constant drawdown pumping case.*

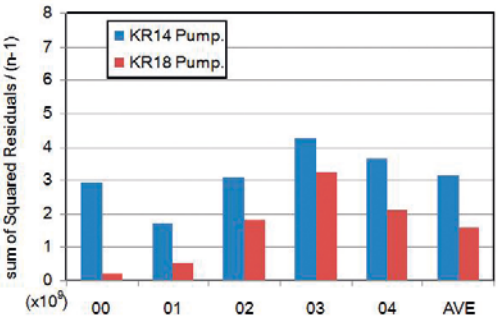

Figure 3-49. *Model plausibility evaluated by normalized RSS based on the flow responses simulations at each realization (00–04).*

An average hydraulic characteristic was controlled by multiplying a factor for changing transmissivity of each fracture. Figure 3-50 shows the variability of the model plausibility evaluated by the RSS normalized by number based on pressure responses for both cases of KR-14 pumping and KR-18 pumping, by changing the factor, 0.1, 0.2, 1, 2, 5, 7, 10, for both. The change of average of hydraulic conductivity affect on recharge rate from the ground surface under the constant head boundary used in this study. The recharge rate change is also shown in Figure 3-50. It might be a reasonable to choose 5 for the factor, because of the minimum RSS for KR18 pumping and also a small number for KR14 pumping. From the measured pressure response data, the upper zone above HZ002 has a small drawdown, which requires less connectivity to the pumping section or high permeability to the constant head boundary to the model. In addition, in the shallow zone above about –100 m, transmissivity tends to have high values. Consequently, the modification on the model was made as shown in Figure 3-51. The transmissivity above HZ002 increased by factor=5, and no change was made for the rest of deeper zone, based on the depth dependency of the transmissivity and the sensitivity calculation shown in Figure 3-50.

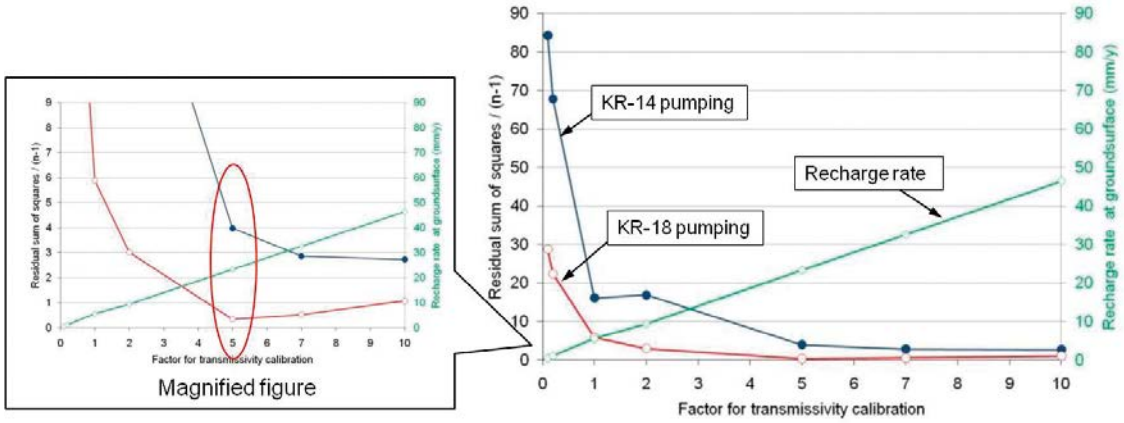

Figure 3-50. *Model plausibility evaluated by normalized RSS based on the pressure responses for both KR-14 pumping and KR-18 pumping, with changing the factor for transmissivity calibration. Left figure shows that y axis is magnified to 9 maximum.*

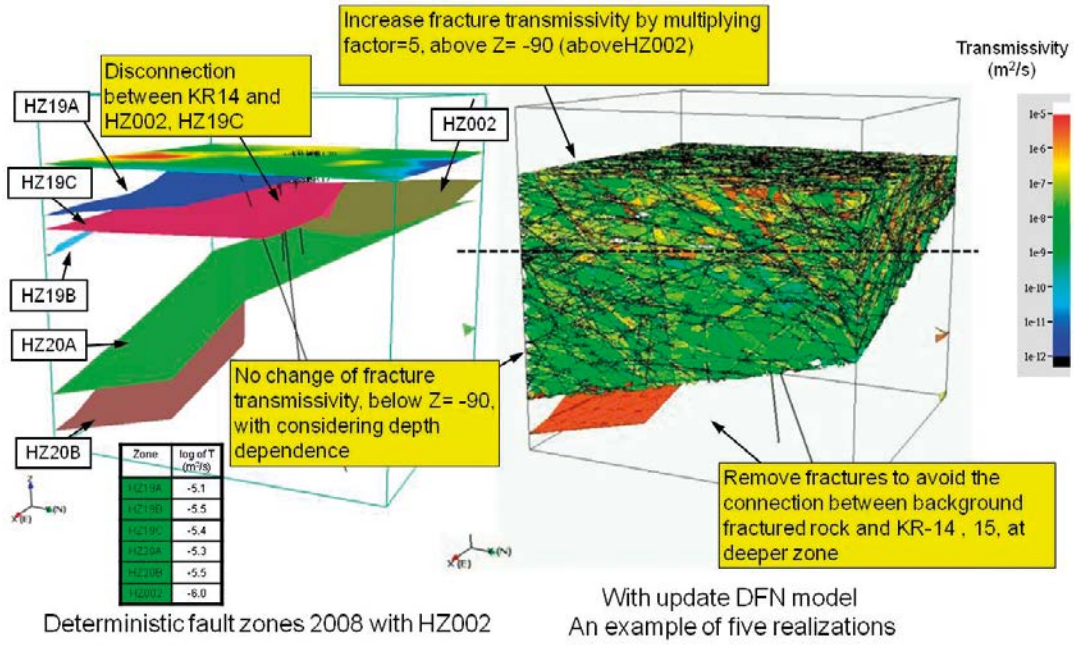

Figure 3-51. *Summary of modification of the model for calibration.*

The heterogeneous flow connectivity of the DFN model on the background fractures was examined by applying a concept of anti-fracture at fracture intersections as shown in Figure 3-52. Fracture network structure is generally composed of frequently distributed fractures that are well connected. The models assume that every fracture is hydraulically connected. However, the issue of hydraulic connectivity is very important and one of the important uncertain factors. For example, the experiments at the Kamaishi Mine (Sawada et al. 2000) and at the TRUE-Block Scale sites (Winberg et al. 2003) show the incomplete hydraulic connectivity, so-called "flow compartmentalisation". Connectivity, including channelling effects, have been recognized as a major remaining uncertainty of the DFN approach since the 1990's (see e.g., Mazurek et al. 1998). This study examined compartmentalisation effect by assuming hydraulic disconnection at the fracture intersection of randomly selected background fractures and fault zones. The parameters of these disconnections were varied to anneal the well-interconnected fracture network structure.

In this study, the probability of fracture disconnection was changed from 0% to 50% to disconnect hydraulically at the fracture intersection, with five stochastic realizations, and the residual sum of squared errors was used for comparing the model plausibility. Figure 3-53 shows the examination results of pressure response, where hydraulic disconnection affects pressure response and RSS increases the percentage of hydraulic disconnection increases. This might be caused by a reduction of effective hydraulic conductivity of background fracture and deterministic fault zones. Figure 3-54 shows the results for flow response. The hydraulic disconnection has relatively less significant effect on this examination. Although hydraulic disconnection to calibrate the well-connected fracture network structure might be effective, it is less valid in this study due to the limited number of realizations.

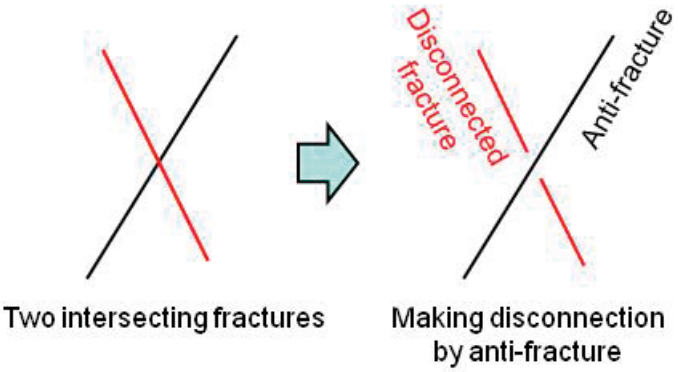

Figure 3-52. *Conceptual illustration on anti-fracture at fracture intersection for making a disconnection of fracture network structure.*

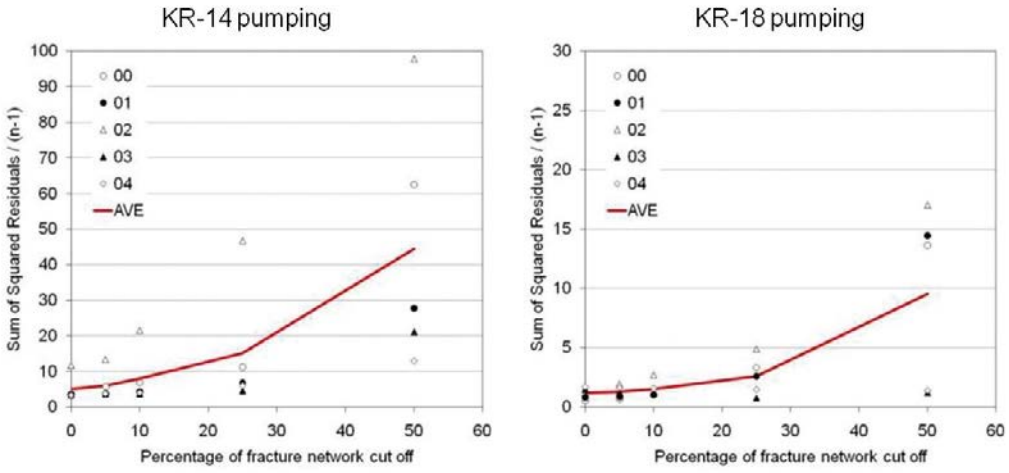

Figure 3-53. *Model plausibility evaluated by normalized RSS based on the pressure responses for both KR-14 pumping and KR-18 pumping, with changing the percentage of fracture network cut off.*

Based on the calibrated model as discussed above, the pressure response and flow response during KR14 and KR18 pumping were recalculated. Figure 3-55 shows the pressure response during KR14 pumping by constant flow rate, 25 L/min. as specified. At the pumping well, KR14, the drawdown is about 4.0 m, which is closer to a measured value of 6.8 m. From Figure 3-55, a minor zone below HZ002 has a larger drawdown than was measured. Decreasing hydraulic connectivity of background fractures may be required at the minor fracture zone below HZ002 around KR14. Figure 3-56 shows the pressure response during KR18 pumping by 6 L/min. as specified. At pumping well KR18, the drawdown is about 1.9 m, which is closer to a measured value, 1.8 m. Figure 3-56 shows a better match between simulated and measured pressure responses than Figure 3-43. Figure 3-57 and 3-58 also show the flow responses during KR14 and KR15 pumping, respectively. Some minor and major responses could be reproduced, as shown Figures 3-46 and 3-47. The calibrated model plausibility based on pressure responses shown in Figure 3-59 is improved significantly, except for a realization number "02", which has relatively larger drawdown for both KR14 and KR18 pumping cases. Improvements to flow response in calibrated simulations are shown in Figure 3-60.

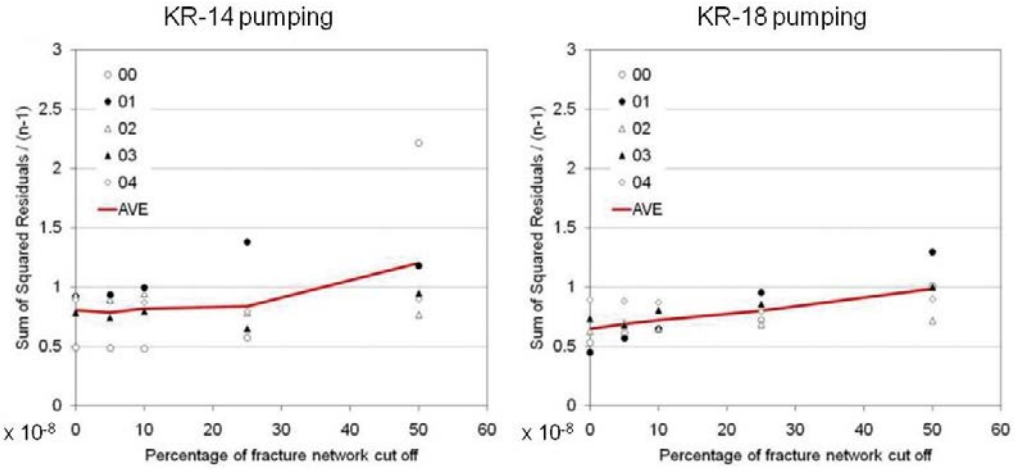

Figure 3-54. *Model plausibility evaluated by normalized RSS based on the flow responses for both KR-14 pumping and KR-18 pumping, with changing the percentage of fracture network cut off.*

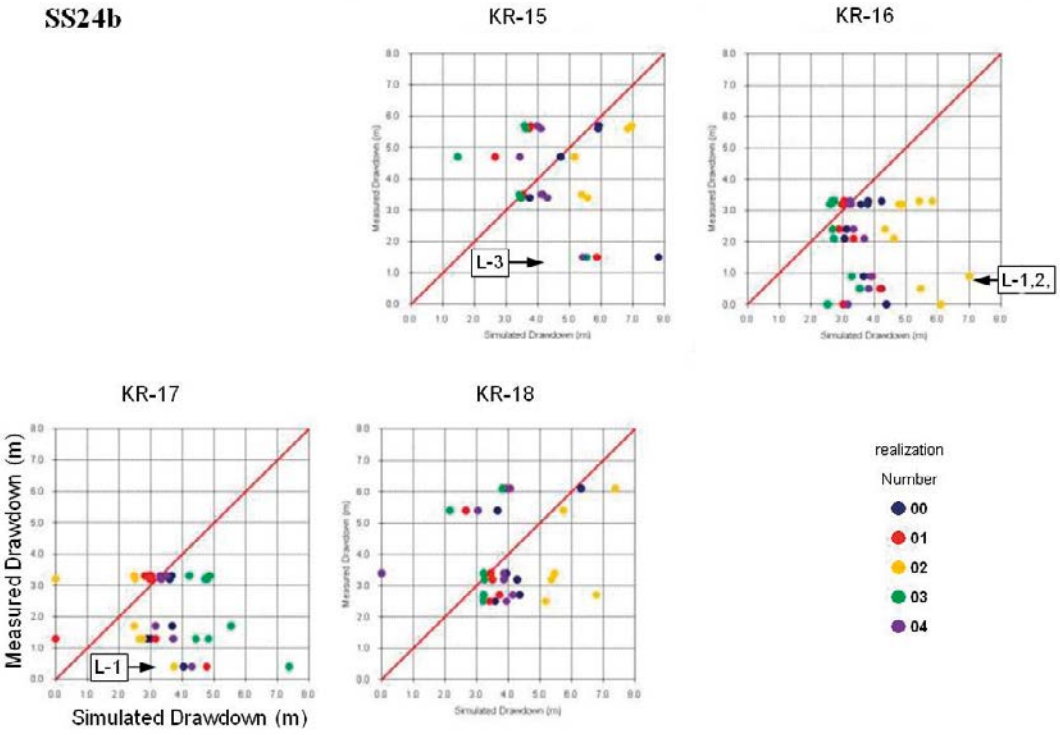

Figure 3-55. *Comparison between simulated (x-axes) and measured (y-axes) drawdown during KR-14 pumping (25 L/min.), based on the calibrated model, which is case SS24b listed in Table 3-8.*

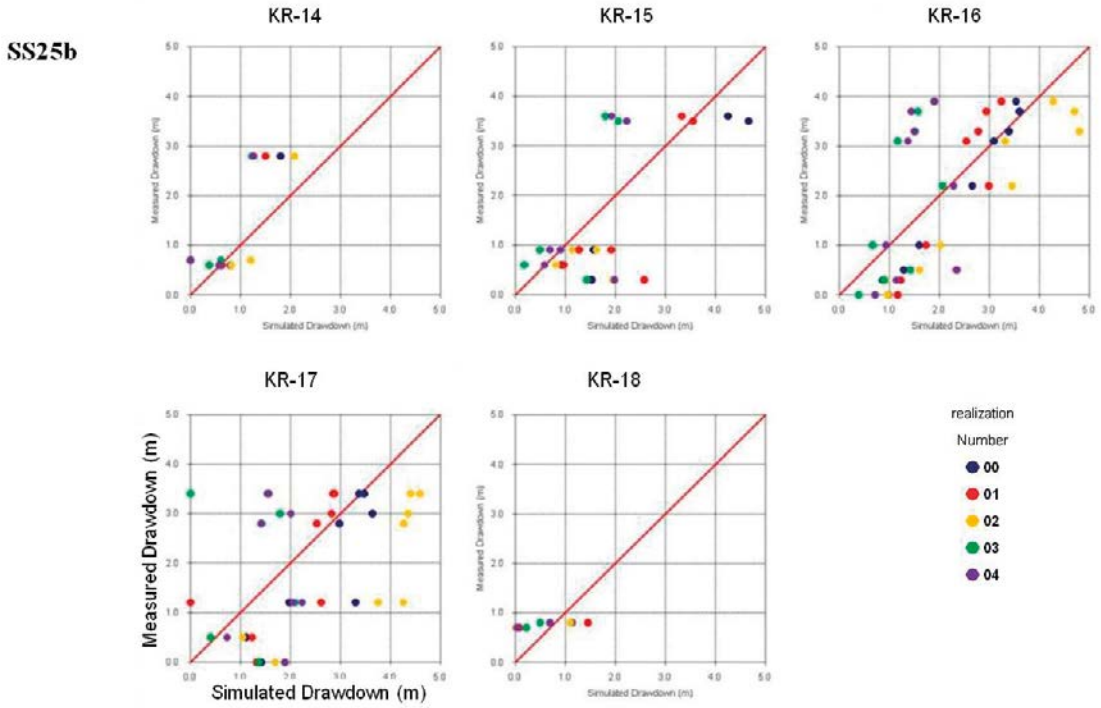

Figure 3-56. *Comparison between simulated (x-axes) and measured (y-axes) drawdown during KR-18 pumping (6 L/min.), based on the calibrated model, which is case SS25b listed in Table 3-8.*

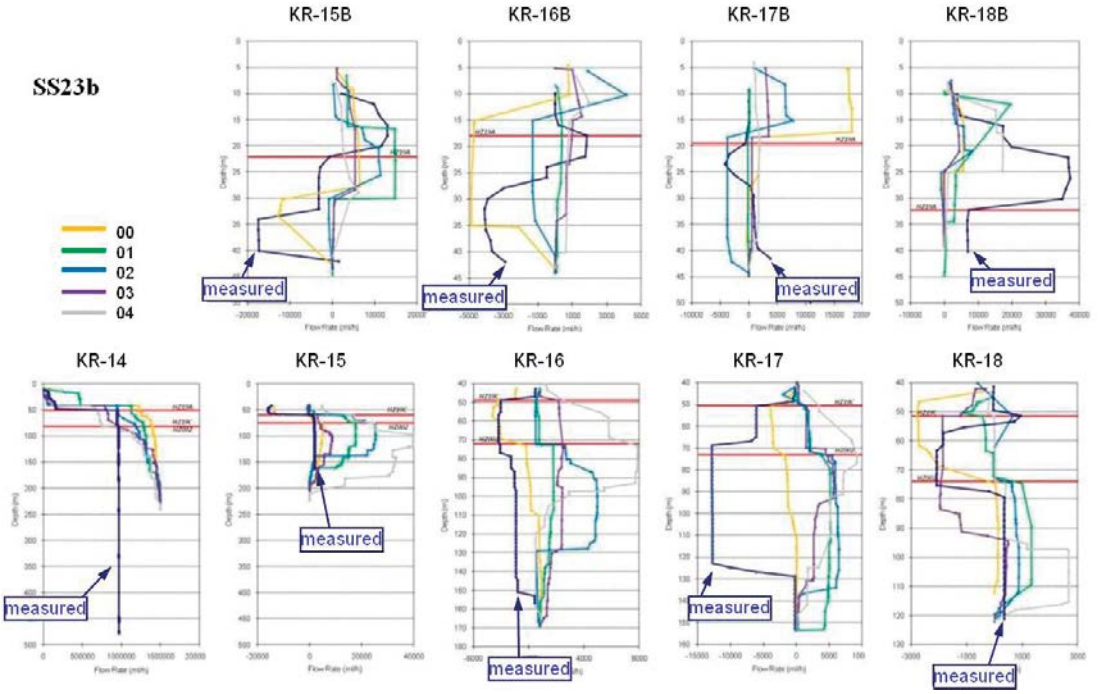

Figure 3-57. *Flow response, PFL flow rate during pumping phase minus flow rate during steady state, compared with the measured value during KR-14 pumping (25 L/min.), which is case SS23b listed in Table 3-8.*

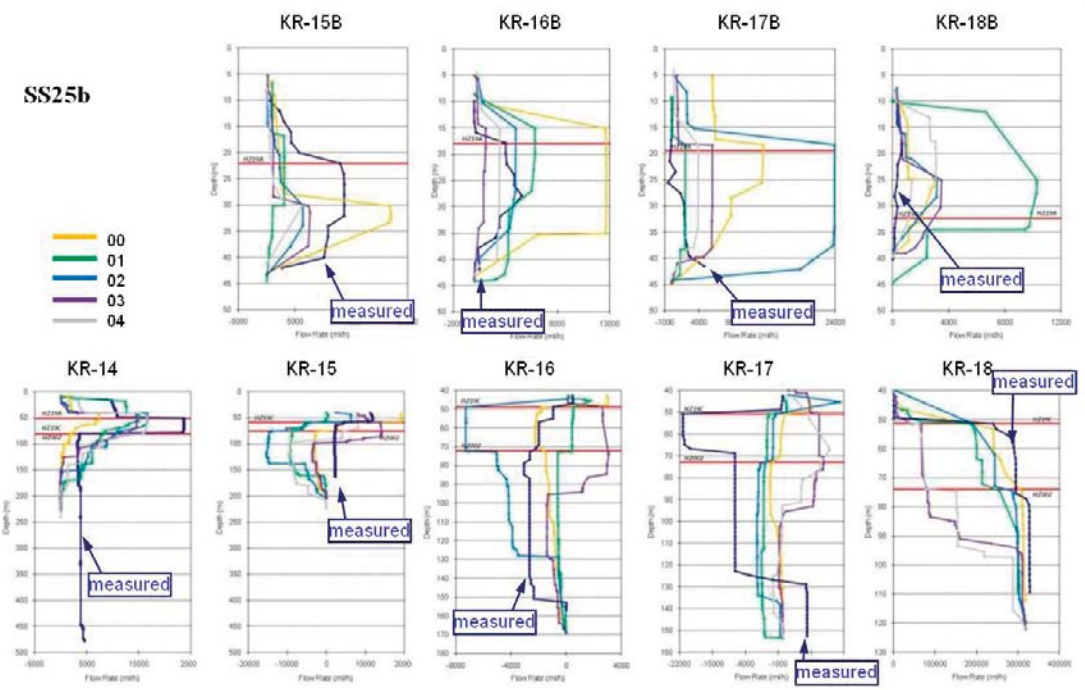

Figure 3-58. *Flow response, PFL flow rate during pumping phase minus flow rate during steady state, compared with the measured value during KR-18 pumping (6 L/min.), which is case SS25b listed in Table 3-8.*

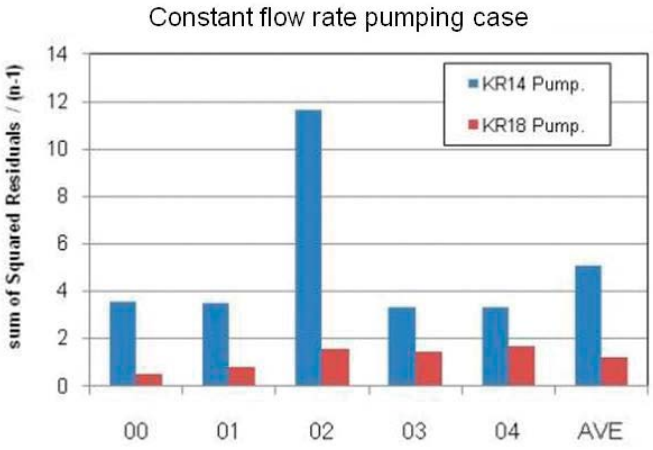

Figure 3-59. *Calibrated model plausibility evaluated by normalized RSS based on the pressure response simulations.*

The models were applied for conducting the particle tracking simulations to calculate hydrodynamic transport resistance (f-factor), F, as specified:

$$F = \sum_i \frac{W_i L_i}{Q_i} = \sum_i \frac{2L_i}{q_i} \qquad 3\text{-}3$$

Where W_i and L_i are width and length of i-th flow channel, respectively. Q_i and q_i are groundwater flow rate and Darcy flux of i-th flow channel, respectively. This corresponds to "PA29" listed in Table 3-8. Nine starting points are specified around KR-14 borehole and the particles were tracked from the starting points to the model boundaries (Vidstrand et al. 2012). Figure 3-61 shows the f-factor distribution from each starting point based on non-calibrated model as illustrated in Figure 3-41. In this study, about hundred of particle trajectories were used for the analyses. F-factors are widely distributed among the particle trajectories and also shows different pattern among the stochastic realizations. The f-factor calculated by the calibrated model, as illustrated in Figure 3-62, slightly decreased, especially starting from points 4 and 5. This decrease might be caused by changing transmissivity at the surface region upper than z=–90.

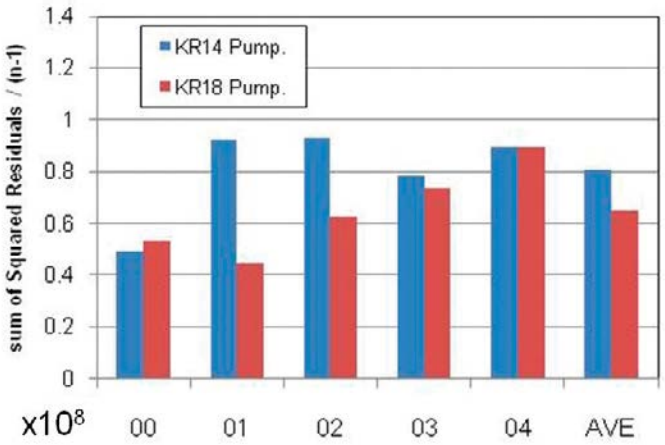

Figure 3-60. *Calibrated model plausibility evaluated by normalized RSS based on the flow response simulations.*

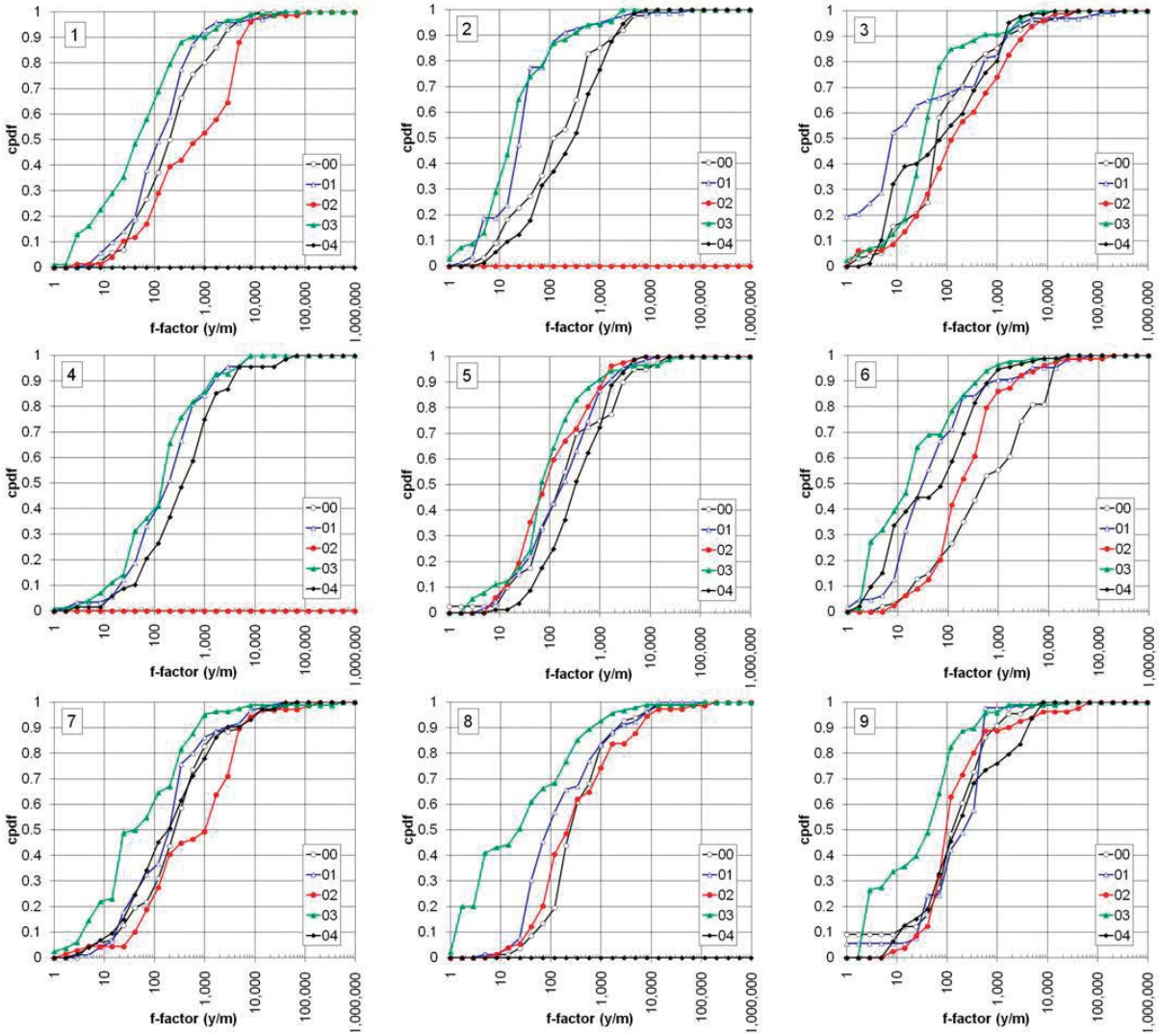

Figure 3-61. *F-factor distribution starting from nine points as specified, case PA20c listed in Table 3-8.*

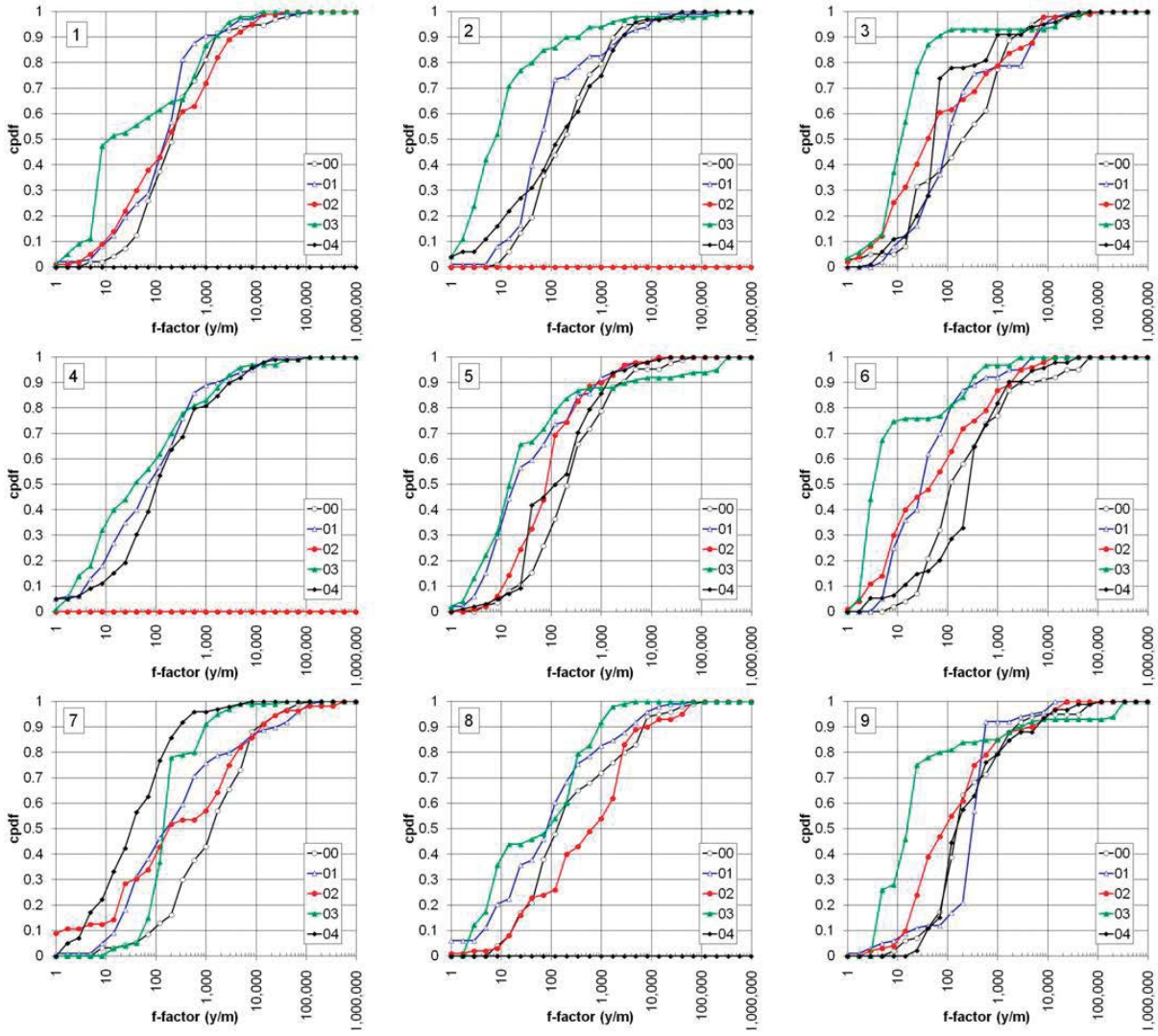

Figure 3-62. *F-factor distribution starting from nine points as specified, case PA29 listed in Table 3-8.*

3.3 Task 7C – Single-fracture scale

3.3.1 Modelling approach

The objective of Task 7C is detailed modelling of heterogeneity within a single fracture around the shafts at ONKALO. The heterogeneity scales of concern vary from the 10 m scale (between boreholes) to the 0.01 m scale (which controls PFL measures and transport behaviour). The model was based on available data provided by the task specification (Vidstrand et al. 2012). Several studies have been carried out looking at the micro-structural model of a fracture wall and the spatial distribution of aperture and/or transmissivity in a single fracture (Hakami et al. 1995, Murata 2001, Tetsu and Sawada 2010, Sato and Sawada 2010, Sawada and Sato 2010). The modelling methodology requires information as listed below:

- Data type / category: geometry of a fracture, transmissivity, fracture width, mineral fillings.
- Spatial resolution: along the drift walls, in core and image logs at boreholes.
- Scale of influence of heterogeneity on flow and transport at/between boreholes.
- Relevance to the target: correlation between transmissivity and aperture, roughness.

In general, data available for the modelling is very limited in category, resolution and number. The properties, such as transmissivity and fracture width are only applicable for a certain portion of the fracture, and at a specific scale. However, it is generally assumed that this variability is subsumed within the overall uncertainty of the calculation and the variability between fractures.

Figure 3-63 shows the provisional work flow for modelling the heterogeneous aperture distribution within a single fracture discussed in Task 7C. Based on PFL transmissivity data, aperture distribution was estimated from Doe's law (Uchida et al. 1994). Joint roughness number (Jr) measurements at the PP and KR boreholes contributed to modelling fracture roughness. Aperture mapping data at shafts and fracture geological investigation of boreholes can be used as input information for modelling spatial distribution. However, since spatial resolution and the amount of data were not sufficient for analysis, these data were not used in this modelling study. Groundwater inflow measurement data measure by "Nappy tests" at shaft KU2 was translated to aperture data, assuming an arbitrary boundary condition and Doe's law which is empirical correlation between transmissivity and aperture. Aperture values were estimated from PFL transmissivity data using the Doe's law. These apertures were then used as constraint values for generation of heterogeneous aperture fields using SGeMS (Stanford Geostatistical Modelling Software; Remy et al. 2009). A range of simple variogram models were evaluated with SGeMS, and the resulting aperture fields were compared visually with images from the resin injection data from the TRUE experiments (Winberg et al. 2003) and the Kamaishi Mine rock sample (Tetsu and Sawada 2010). The visual comparisons indicated that the simple variogram models were inadequate, and they did not provide the multi-scale channelling structures visible in both the TRUE resin injection data and the Kamaishi Mine rock resin impregnation results.

An alternative model approach was therefore developed to simulate a multi-scale fracture roughness model, which is characterized by variable correlation lengths in different scales, as shown in Figure 3-64. Due to an absence of measured data to describe multi-scale fracture roughness at this study area, the multi correlation lengths were arbitrary defined by assuming similar patterns as the Kamaishi Mine rock sample caused by slickenside and slicken step at the several-centimetre scale and several decimeter scale, and by fracture branch and fracture intersection in several-meter scale and several-tens-of-meters scale, respectively. Heterogeneous aperture distribution was also constrained at each measured point and a histogram of aperture data estimated from PFL transmissivity data and Nappy tests as discussed above. However, the transmissivity distribution estimated from Nappy tests was shifted to match with geometrical mean of transmissivity by PFL measured at PP boreholes at KU2 and KU3, respectively.

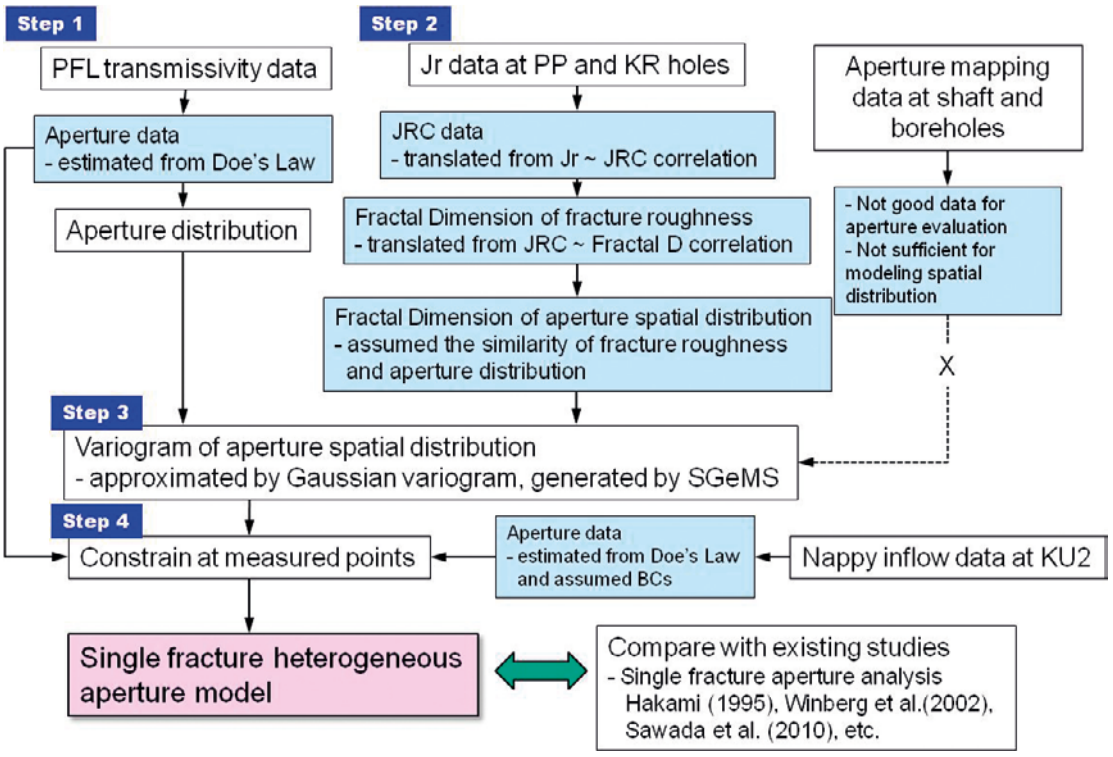

Figure 3-63. *Work flow for modelling a single fracture heterogeneous aperture.*

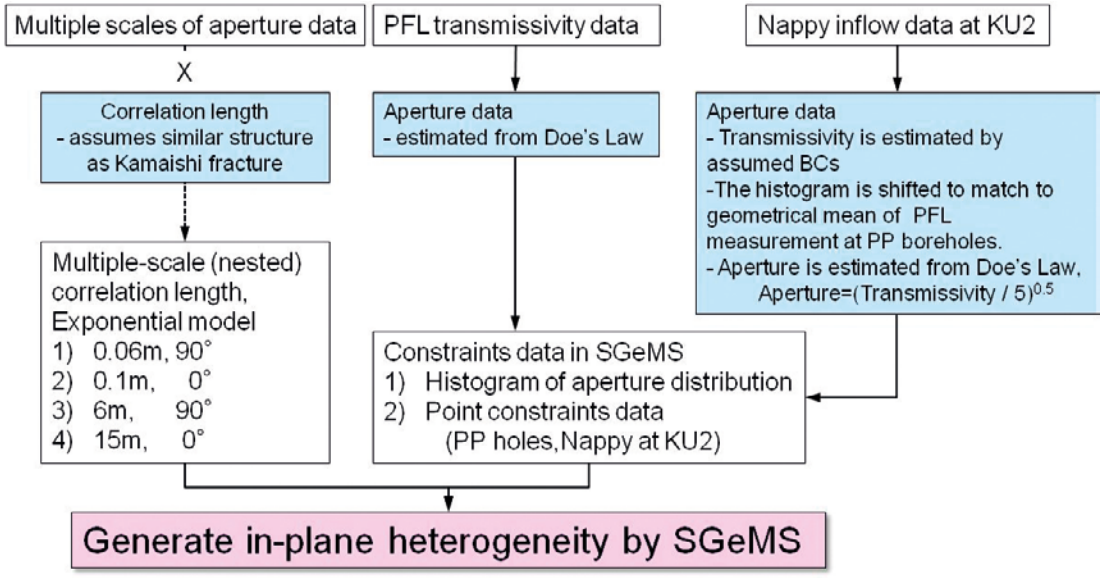

Figure 3-64. *Alternative modelling approach to conceptualise the multi-scale correlation length model.*

3.3.2 Data usage and interpretation

The modelling approach as shown in Figure 3-64 used the aperture data estimated from PFL transmissivity data and groundwater inflow data measured at shaft KU2 by Nappy tests. Transmissivity data measured by PFL at PP and KR boreholes were transformed by using empirical correlation between transmissivity and transport aperture, which makes transmissivity a quadratic function of the fracture aperture:

$$Aperture = aT^b \qquad 3\text{-}4$$

where a is constant and b is an exponent. In this study, same parameter values as used in Task 7A, a=0.5 and b=0.5 were applied to this equation. Figure 3-65 shows the fitted aperture distribution. Nappy inflow data measured at shaft KU2 were translated to aperture data, assuming an arbitrary boundary condition and Doe's law.

Figure 3-66 shows in-plane heterogeneity models for both KU2 and KU3 based on the multi-scale correlation lengths model, listed in Figure 3-64, generated by a nested approach in SGeMS. Aperture spatial distribution was constrained at the PP and KR boreholes by aperture data estimated from PFL transmissivity. Also, aperture distribution was constrained by the histogram of aperture value estimated from Nappy inflow data.

The background fractures were modelled by a stochastic DFN model approach. Figure 3-67 shows the flow chart for estimating Task 7C's stochastic parameters. The orientation data measured at the PP and KR boreholes were analyzed and the Elliptical Fisher model was chosen. Transmissivity distribution was estimated based on transmissivity data measured at PP boreholes and KR boreholes by PFL, and transport aperture was estimated from the correlation to the fracture's transmissivity. Other parameters, such as density and fracture size were estimated based on the existing studies.

3.3.3 Geometrical description

The modelling region for Task 7C studies is 200 m × 200 m × 200 m, centring on shafts KU2 and KU3 (Figure 3-68). The target fracture, FR1, was modelled at the scale of a single fracture (20 m × 20 m), orientated to match the trace observed at the shafts. Aperture values generated by SGeMS in 0.05 m spatial resolution are up-scaled to a 0.2 m scale of finite element mesh.

3.3.4 Processes considered

Task 7C was used to understand steady state groundwater flow through the target fractures around the shafts, embedded within a background fracture network model. All fluids are assumed to be fresh water, with a constant density of 1 g/cc and a temperature of 20°C.

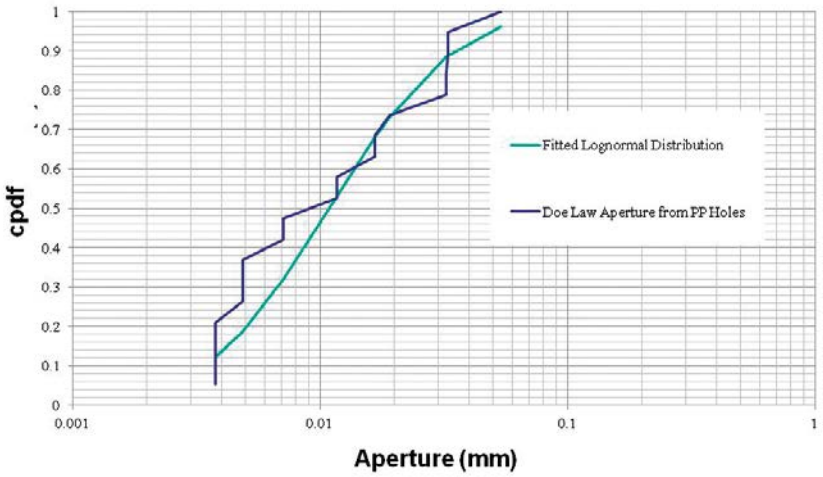

Figure 3-65. *Estimated aperture distribution estimated from translated aperture based on measured PFL transmissivity data by assuming an empirical correlation between aperture and transmissivity.*

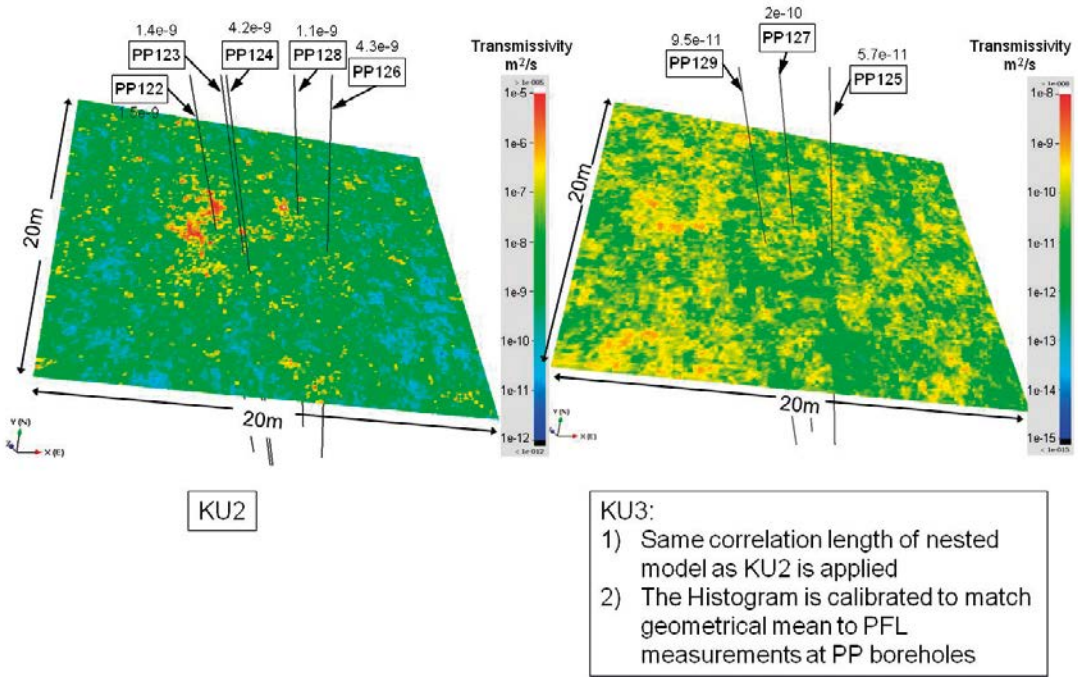

Figure 3-66. *Examples of in-plane heterogeneity models for both KU2 and KU3 based on the multi-scale correlation length model. These models are constrained by aperture data estimated from PFL transmissivity at each PP and KR borehole, and also constrained by the histogram of aperture value estimated from Nappy inflow data.*

3.3.5 Boundary and initial conditions

Figure 3-68 shows the boundary condition for these simulations. The side boundary of the 200 m block is defined as a constant head boundary of –60 m, which considers regional drawdown around the shafts due to excavation activities at ONKALO. The block's top and bottom boundary are set as no flow boundaries. Borehole boundary conditions for open boreholes are set as constant head. For plugged boreholes, the boundary condition is set as a group flux boundary condition with flux Q=0. Figure 3-4 provides a conceptual illustration of the Group Flux boundary condition. This boundary condition assumes zero resistance to flow within the borehole, such that heads within the borehole are identical.

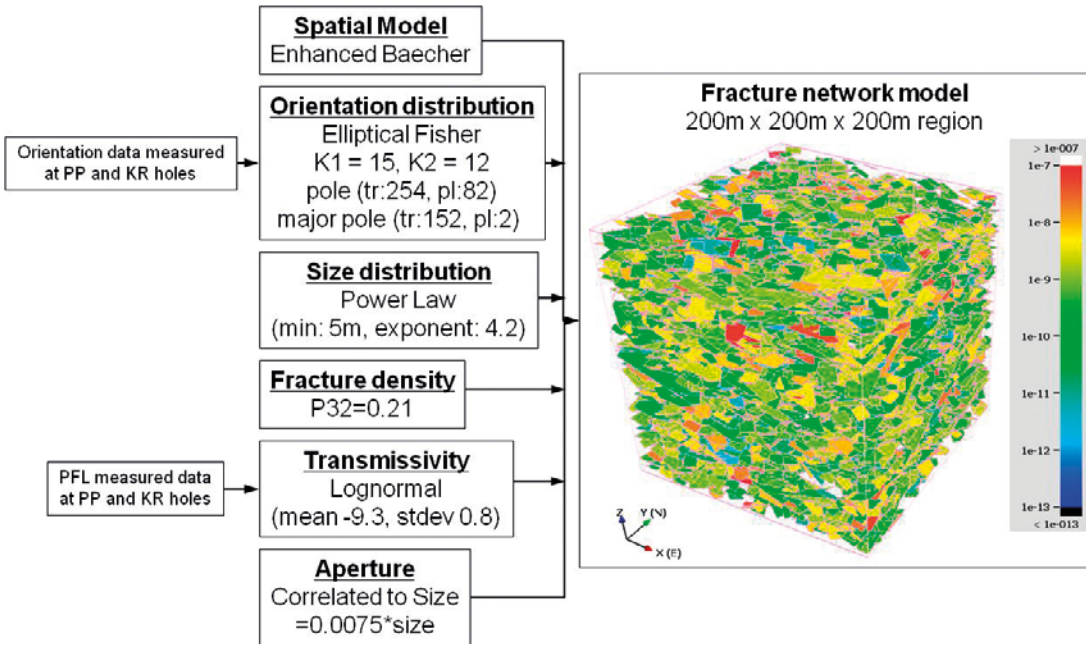

Figure 3-67. *Flow chart for estimating background fracture parameters.*

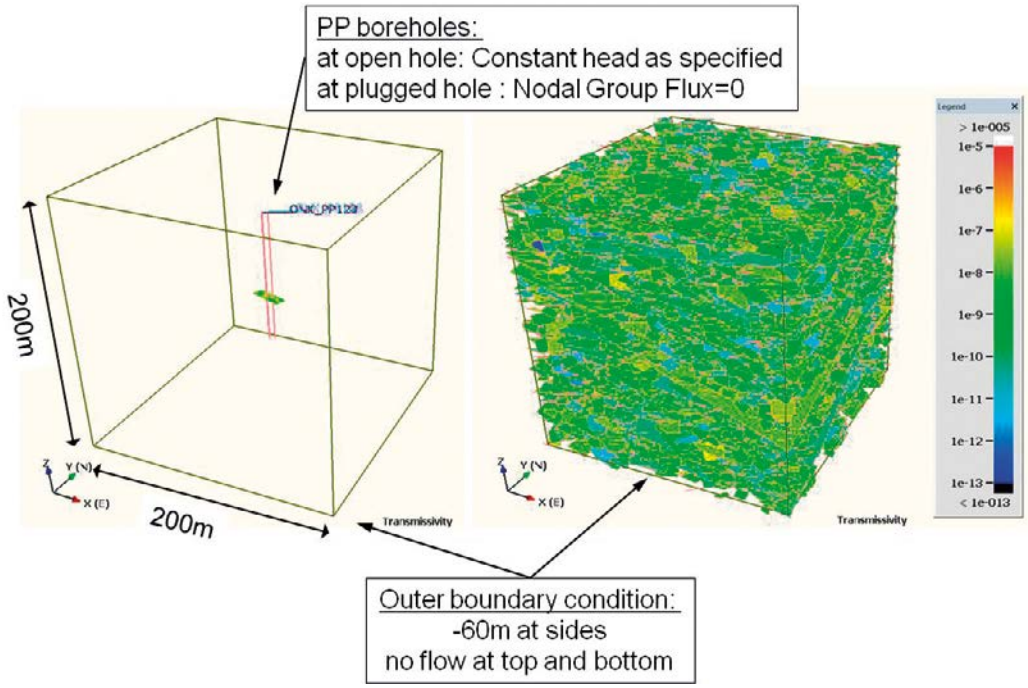

Figure 3-68. *The modelling region, 200 m × 200 m × 200 m block, for Task 7C studies.*

3.3.6 Numerical model

Modelling of Olkiluoto for Task 7C was also carried out using FracMan (Dershowitz et al. 2007, www.fracman.com).

3.3.7 Parameters

For the target fractures, the parameters in a single fracture heterogeneity model were generated based on the parameter list described in Figure 3-64. Also, stochastic parameters for the background fractures are listed in Figure 3-67.

3.3.8 Model conditioning and calibration

Table 3-9 shows the simulation cases specified by Vidstrand et al. (2012). In this study, ten realizations of the aperture spatial distribution models were examined. In addition, the simulation cases for KU2 and KU3 were focused, since only a few data were available for KU1 examinations.

Table 3-9. Task 7C simulations cases as specified in Vidstrand et al. (2012).

Shaft	borehole	Outer Boundary Head masl	Borehole head masl	PFL measure at FR1 mL/min.	condiliton at other boreholes	simulaton cases
KU2	PP122	-60	-181.09	996	other boreholes were plugged by packer	s-PP122
	PP123	-60	-181.09	961	other boreholes were plugged by packer	s-PP123
	PP124	-60	-181.09	2870	other boreholes were plugged by packer	s-PP124
	PP126	-60	-181.09	2930	other boreholes were plugged by packer	s-PP126
	PP128	-60	-181.09	761	other boreholes were plugged by packer	s-PP128
KU1	PP131	-60	-177.52	-	other boreholes were plugged by packer	s-PP131
	PP134	-60	-177.52	367	other boreholes were plugged by packer	s-PP134
	PP137	-60	-177.52	-	other boreholes were plugged by packer	s-PP137
KU3	PP125	-60	-176.81	38	PP127,PP129 close	s-PP125
		-60	-176.81	8	PP127,PP129 open	c-PP125-1
		-60	-176.81	11	PP127open (175mL/min.), PP129close	c-PP125-2
		-60	-176.81	17 or 16	PP127close, PP129open (330mL/min.)	c-PP125-3
	PP127	-60	-176.81	135	PP125, PP128 close	s-PP127
		-60	-176.81	21	PP125, PP128 open	c-PP127-1
		-60	-176.81	158	PP125open (90-110mL/min.), PP129close(overpressure +2bar)	c-PP127-2
	PP129	-60	-176.81	-	No data shown	s-PP129
		-60	-176.81	63	PP125,PP127 open	c-PP129-1

KU2 examinations

Figures 3-69 through 3-73 compare simulation results and measured values for a series of PFL measurements during pumping tests at each PP borehole around KU2. The left portion of each figure represents data from observation boreholes and the right portion of each figure represents pumping boreholes. Simulation results are shown as solid circles and measured values are shown as red open circles. Figure 3-74 shows the model plausibility by normalized RSS. During ten realizations of the distribution model for fracture aperture, simulation results were distributed close to (or near) the measured values, except for a realization number 04 for P122 pumping case. However, PP124 and PP126 show different behaviour from the measured value. The flow rate at the PP126 borehole is significantly smaller than measured values. Higher transmissivity around PP126 might be required to establish more flow connectivity between PP122 and PP126. In the same way, a higher flow rate at PP126 during pumping at PP123 and PP124 might be required. In addition, the flow rate at PP124 is lower than measured values when pumping the PP126 and PP128 boreholes. Figures 3-75 and 3-76 show sensitivity calculation results with increasing transmissivity by one order of magnitude, around PP124 and PP126 in a 1-meter-radius area, respectively. By increasing transmissivity around the PP124 and PP126 boreholes, flow rates at those boreholes slightly increased. Although it is hard to match simulation results to measured values at every measured point, the sensitivity calculations shows a possibility of being useful for calibrating the heterogeneous aperture distribution model.

Figures 3-77 through 3-80 show a comparison between simulation results and measured values for a series of PFL measurements during pumping tests at each PP borehole around KU3. Figures 3-77 through 3-79 are steady state pumping case, at PP125, PP127 and PP129, respectively. The left portion of each figure represents data from observation boreholes and the right portion of each figure represents pumping boreholes.

Figure 3-80 compares simulation results with measured value for the crosshole tests. The left figure shows the c-PP125-1,c-PP127-1 and c-PP-129-1 cases which are the inflow rate at each borehole during open condition of the three boreholes. The middle figure shows the c-PP125-2 case which is inflow at PP125 during open condition at PP127 and closed condition at PP129. The right figure shows the c-155-3 case which is inflow at PP125 during closed condition at PP127 and open condition at the PP129 pumping borehole.

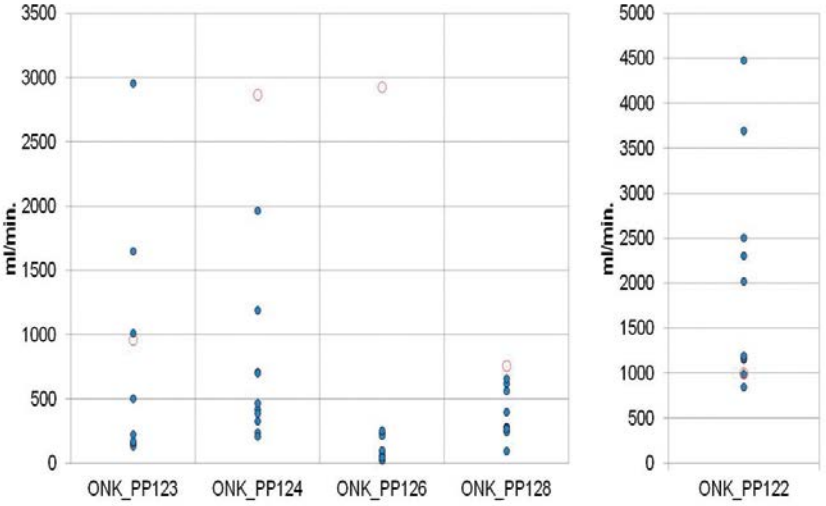

Figure 3-69. *PFL flow measurement during PP122 pumping, for the case s-PP122. Left figure = observation boreholes; right figure = pumping boreholes; solid circles = simulation results; red open circles = measured values.*

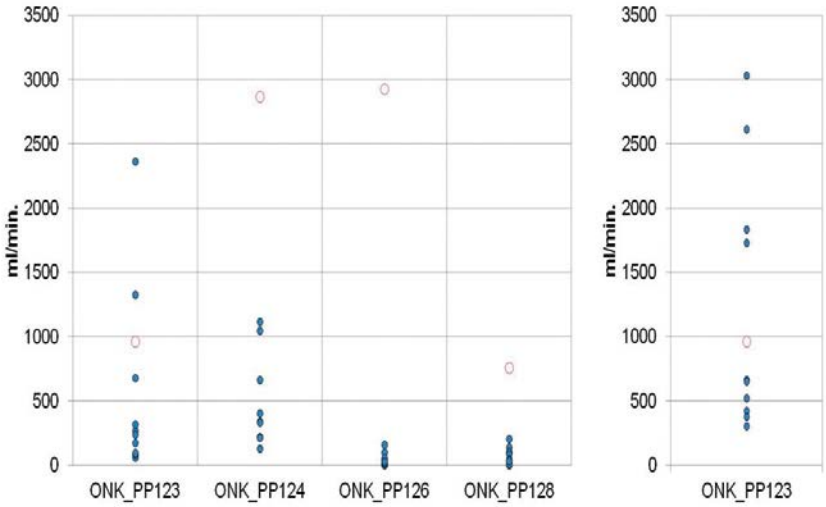

Figure 3-70. *PFL flow measurement during PP123 pumping, for the case s-PP123. Left figure = observation boreholes; right figure = pumping boreholes; solid circles = simulation results; red open circles = measured values.*

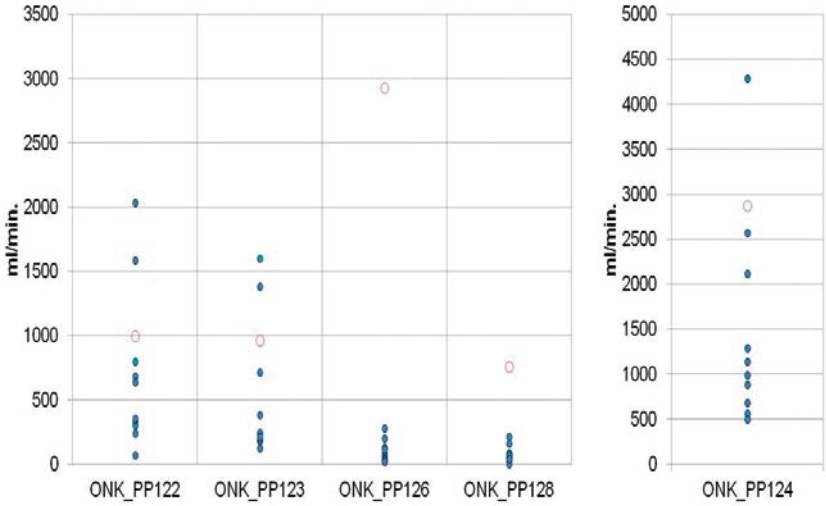

Figure 3-71. *PFL flow measurement during PP124 pumping, for the case s-PP124. Left figure = observation boreholes; right figure = pumping boreholes; solid circles = simulation results; red open circles = measured values.*

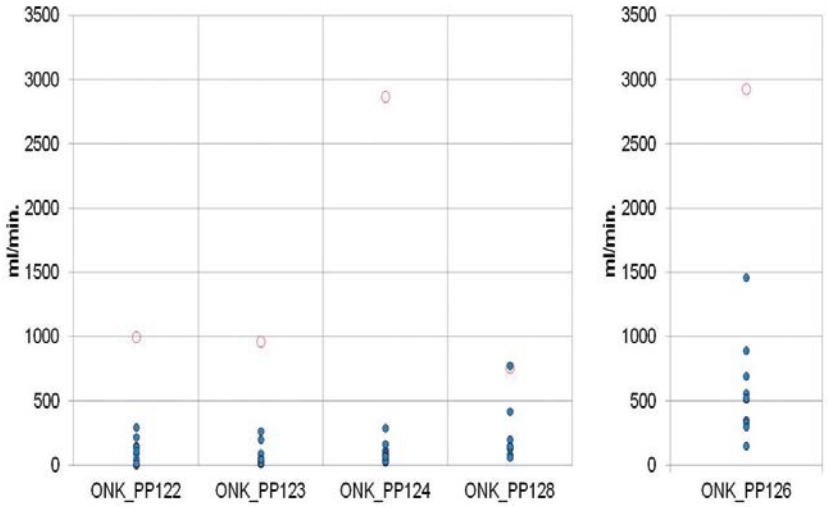

Figure 3-72. *PFL flow measurement during PP126 pumping, for the case s-PP126. Left figure = observation boreholes; right figure = pumping boreholes; solid circles = simulation results; red open circles = measured values.*

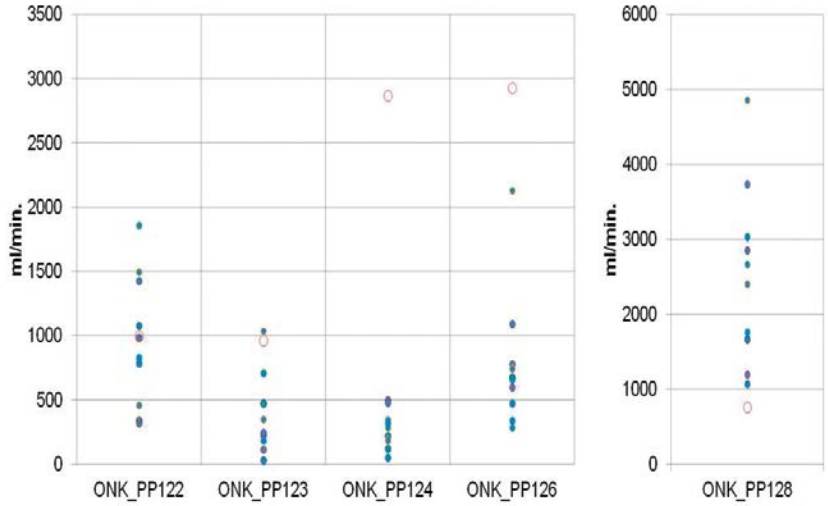

Figure 3-73. *PFL flow measurement during PP128 pumping, for the case s-PP128. Left figure = observation boreholes; right figure = pumping boreholes; solid circles = simulation results; red open circles = measured values.*

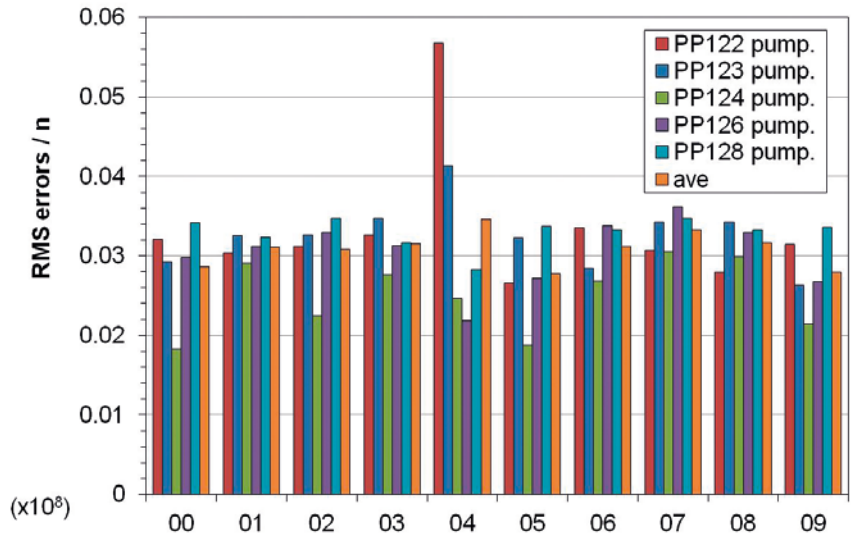

Figure 3-74. *Model plausibility evaluated by normalized RSS based on PFL flow simulations around KU2.*

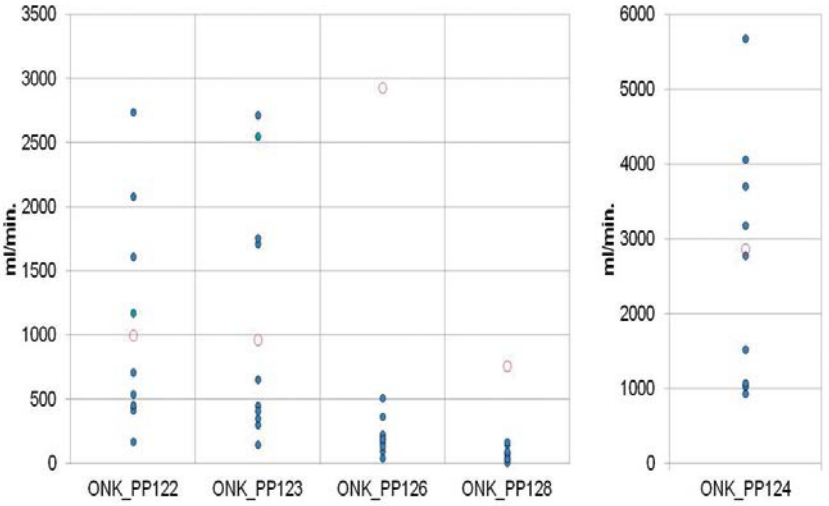

Figure 3-75. *Sensitivity calculation results with increasing transmissivity by one order around PP126 and PP124 in radius 1 m area. PFL flow measurement during PP124 pumping, for the case s-PP124.*

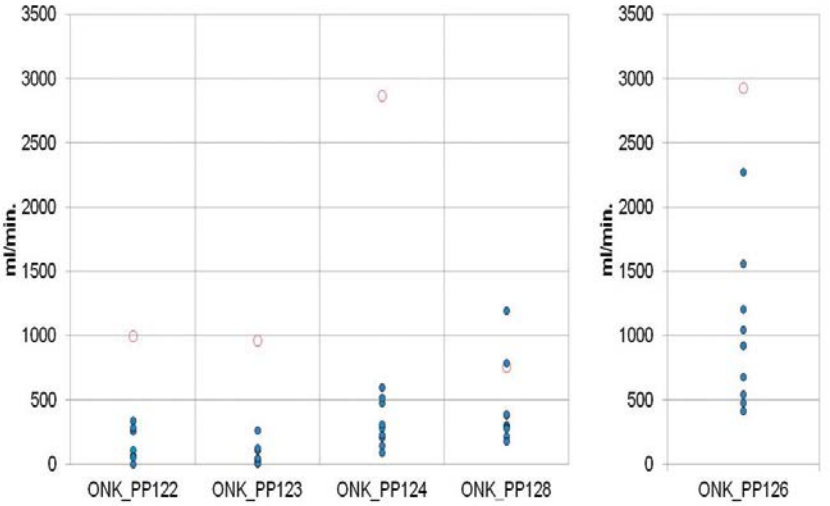

Figure 3-76. *Sensitivity calculation results with increasing transmissivity by one order around PP126 and PP124 in radius 1 m area. PFL flow measurement during PP126 pumping, for the case s-PP126.*

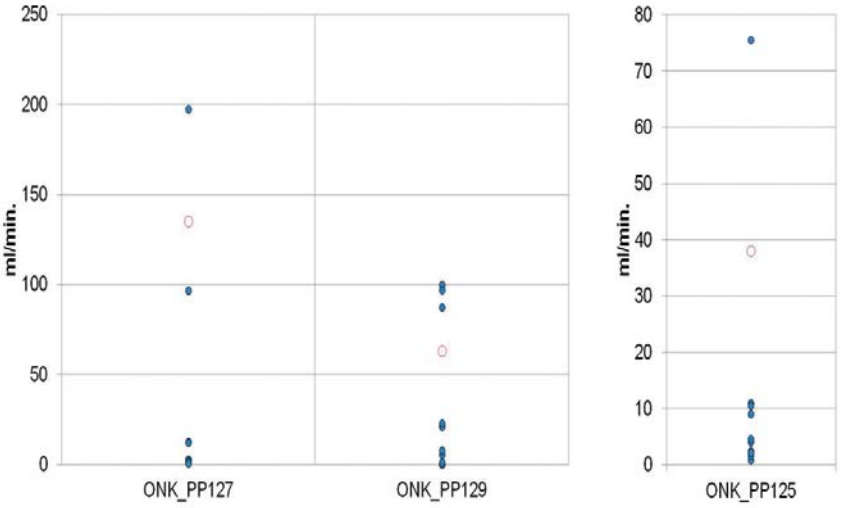

Figure 3-77. *PFL flow measurement during PP125 pumping, for the case s-PP125. Left figure = observation boreholes; right figure = pumping boreholes; solid circles = simulation results; red open circles = measured values.*

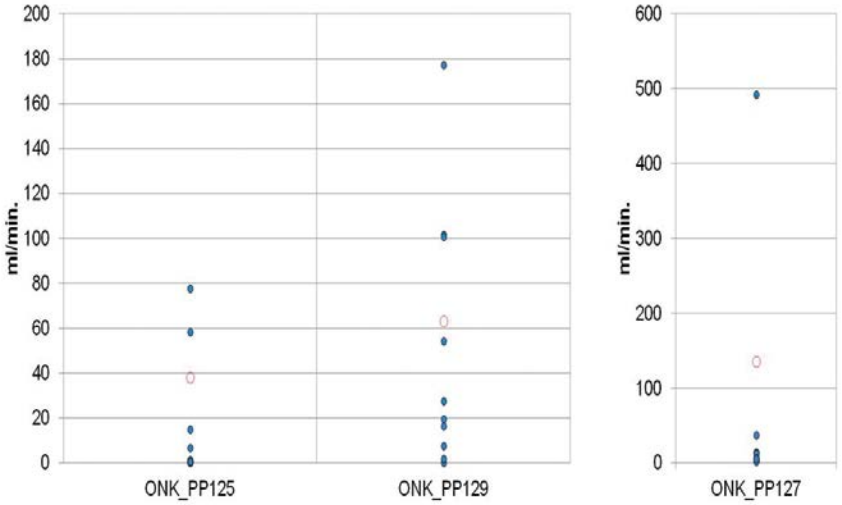

Figure 3-78. *PFL flow measurement during PP127 pumping, for the case s-PP127. Left figure = observation boreholes; right figure = pumping boreholes; solid circles = simulation results; red open circles = measured values.*

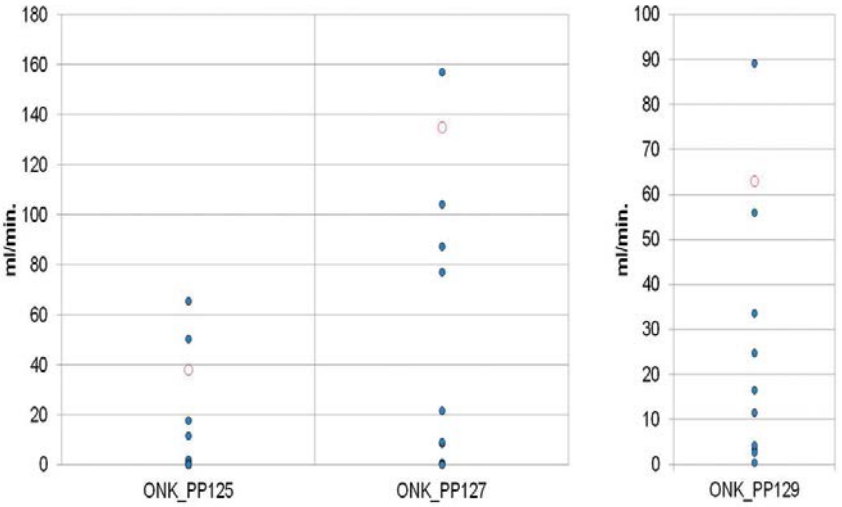

Figure 3-79. *PFL flow measurement during PP129 pumping, for the case s-PP129. Left figure = observation boreholes; right figure = pumping boreholes; solid circles = simulation results; red open circles = measured values.*

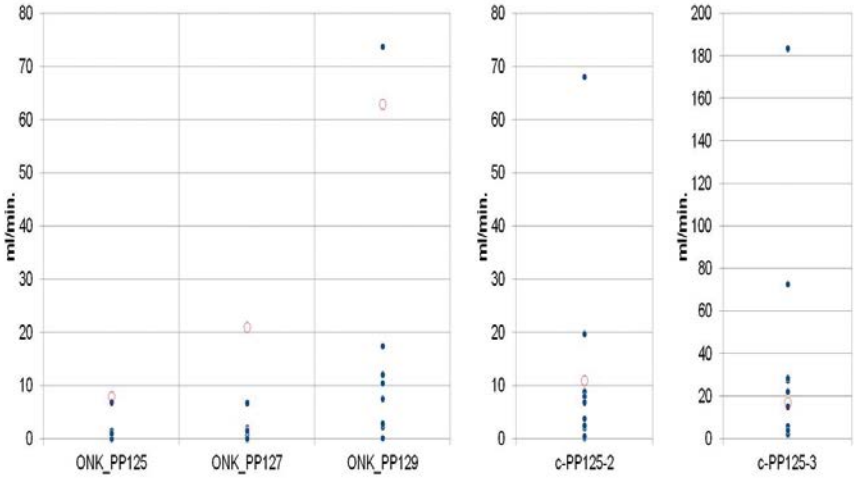

Figure 3-80. *The case c-PP125. Left figure = cases of inflow rate at each boreholes during open condition Middle figure = case of inflow at PP125 during open condition at PP127 and closed condition at PP129. Right figure = case of inflow at PP125 during closed condition at PP127 and open condition at PP129. Solid circles = simulation results. Red open circles = measured values.*

Figure 3-81 shows the model plausibility as measured by normalized RSS. Ten Monte Carlo realizations were used, and each realization utilized aperture values generated from the same distribution. Results distribute close to the measured value.

Figures 3-82 through 3-85 are f-factor distributions calculated by the particle tracking method through 20 m × 20 m heterogeneous fracture model, without considering background fractures. The particle tracking simulations were conducted under asteady state flow condition, with a constant head gradient in either north-south (NS) or east-west (EW) directions. For a NS gradient, a no flow boundary condition was fixed on the East and West faces of the model. For an EW gradient, a no flow boundary condition was fix on the North and South faces of the model

At the target fracture at KU2, f-factor is mainly on the order of 10^{13} s/m. No significant differences are shown between the NS and EW gradient simulations. At the target fracture around KU3, f-factor is mainly distributed at the order of 10^{15} s/m, which is two orders of magnitude smaller than the value for the fracture at KU2. The major difference between KU2 and KU3 is caused by the difference in average transmissivity. The average transmissivity at each target fracture was constrained by the geometrical mean of transmissivity measured at PP boreholes by PFL, $2.1 \cdot 10^{-9}$ m^2/s for KU2 and $1.0 \cdot 10^{-10}$ m^2/s for KU3.

In Task 7C, JAEA implemented the aperture spatial patterns using a multi-scale simulation approach. This approach has the potential to represent the results of the several geological process which determine the roughness structure of fracture walls. These include grooves (slicken line), slicken step structures, fracture intersections, and fracture branching. This approach uses nested correlation lengths ranging from a centimetre scale to a scale of several tens of meters

For the present study, the parameters of the multi-scale simulation were only loosely related to field measurements. However, the necessary model parameters can be derived from a new data collection program focused on characterizing fracture roughness and/or aperture distribution. The present study indicates that such data collection could be of value to support upscaling for flow calculations, and pathway based transport calculations such as f-factor.

Fracture data collection focused on characterizing roughness patterns might include programs for obtaining data on geological structures at a range of scales including grooves along slicken line, slicken step structures, branches of fracture, intersections of two fractures. The understanding of channelized roughness is particularly important for understanding groundwater residence time and f-factor.

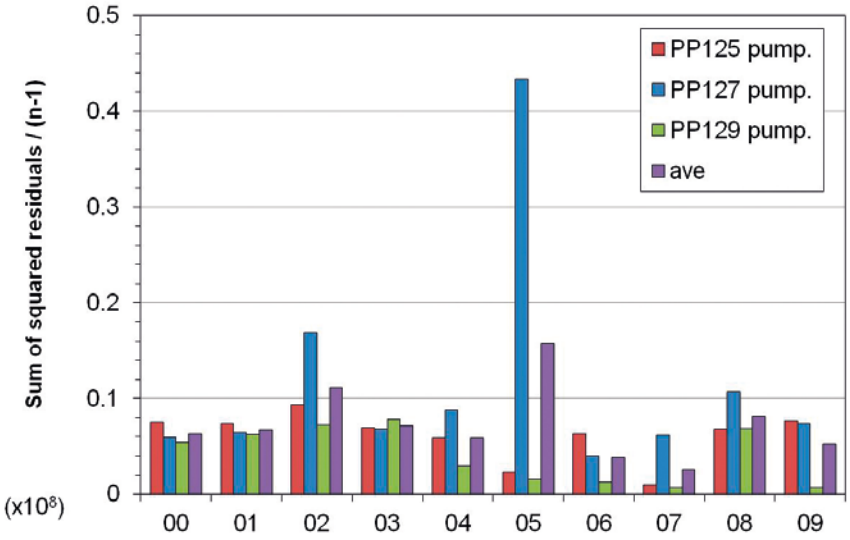

Figure 3-81. *Model plausibility evaluated by normalized RSS based on PFL flow simulations around KU3.*

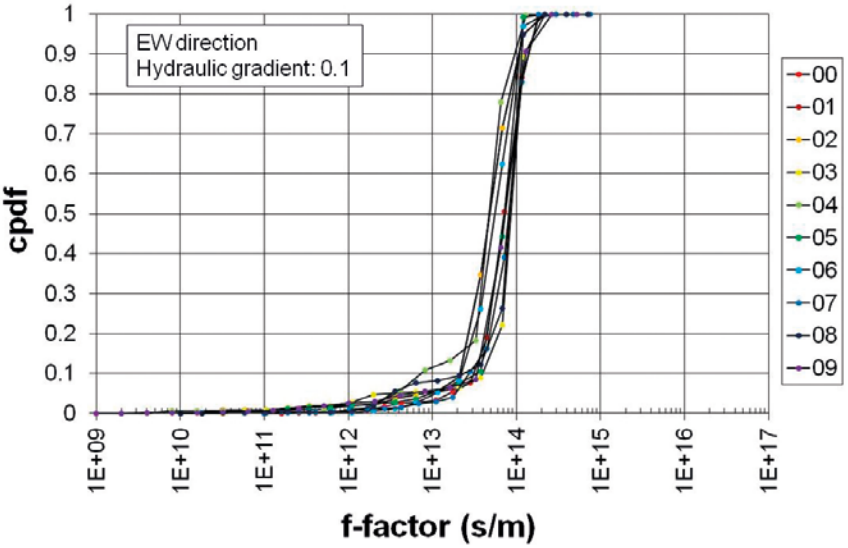

Figure 3-82. *F-factor calculated at KU2 model with 0.1 hydraulic gradient, EW direction.*

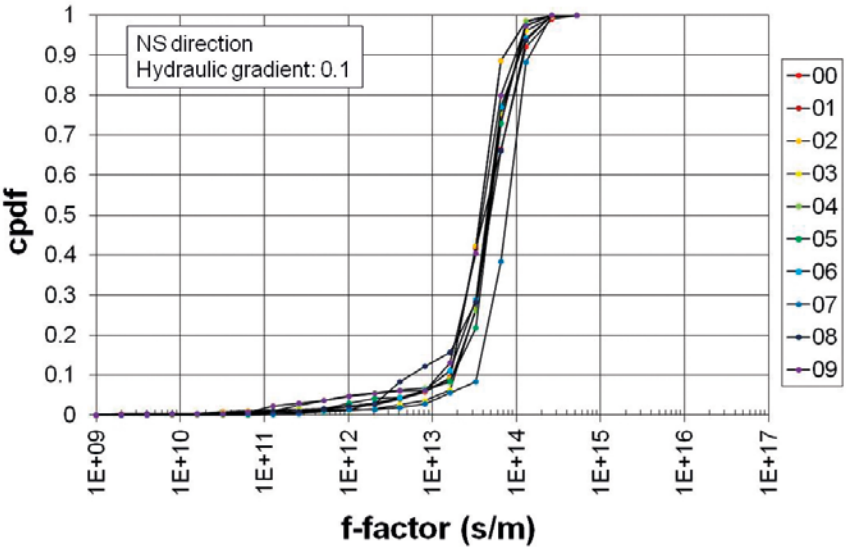

Figure 3-83. *F-factor calculated at KU2 model with 0.1 hydraulic gradient, NS direction.*

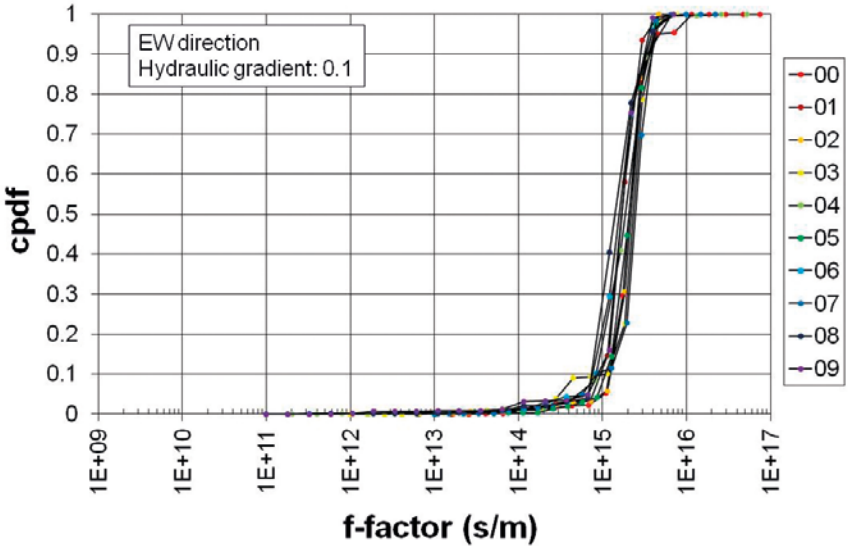

Figure 3-84. *F-factor calculated at KU3 model with 0.1 hydraulic gradient, EW direction.*

Figures 3-86 and 3-87 show the results of upscaling examinations. In these studies, the scale of spatial resolution in representing heterogeneous aperture distribution of 20 m × 20 m target fracture around KU3 was varied by changing discretisation size for upscaling transmissivity and representative transmissivity and f-factor were evaluated. The spatial resolution was changed from a finer scale (0.02 m) to a coarser scale (0.2 m). The 0.2 m scale is the same size used in the simulations to compare with measured values. Ten stochastic realizations were generated by SGeMS based on the same input parameters as shown in Figure 3-64. Figure 3-86 shows the representative transmissivity of the target fracture in north-south direction. For the comparison, the transmissivity is normalized by an average value in the 0.2 m resolution case. Figure 3-87 is f-factor value through the target fracture around KU3 normalized by one of 0.2 m resolution case. Simulated representative transmissivity is not significantly affected by changing the model resolution. However, transport behavior evaluated by f-factor is fully affected by spatial resolution of the heterogeneous aperture distribution model.

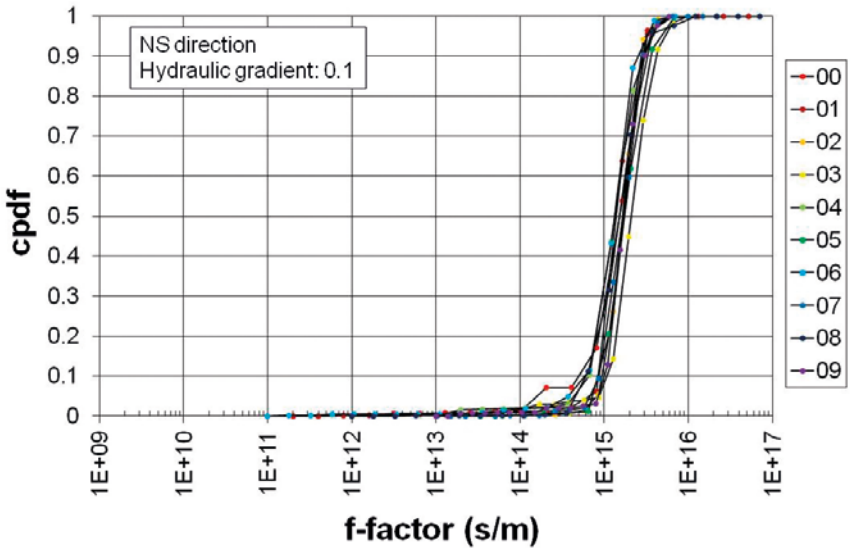

Figure 3-85. *F-factor calculated at KU3 model with 0.1 hydraulic gradient, NS direction.*

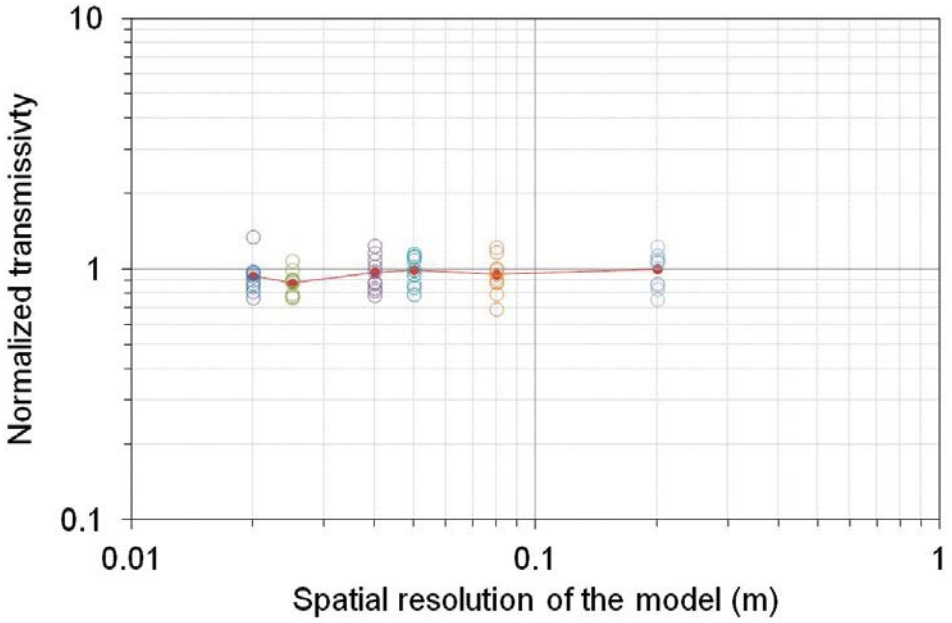

Figure 3-86. *Normalized representative transmissivity of target fracture around KU3. Open circle shows the results from ten realizations, and solid circle is an average value.*

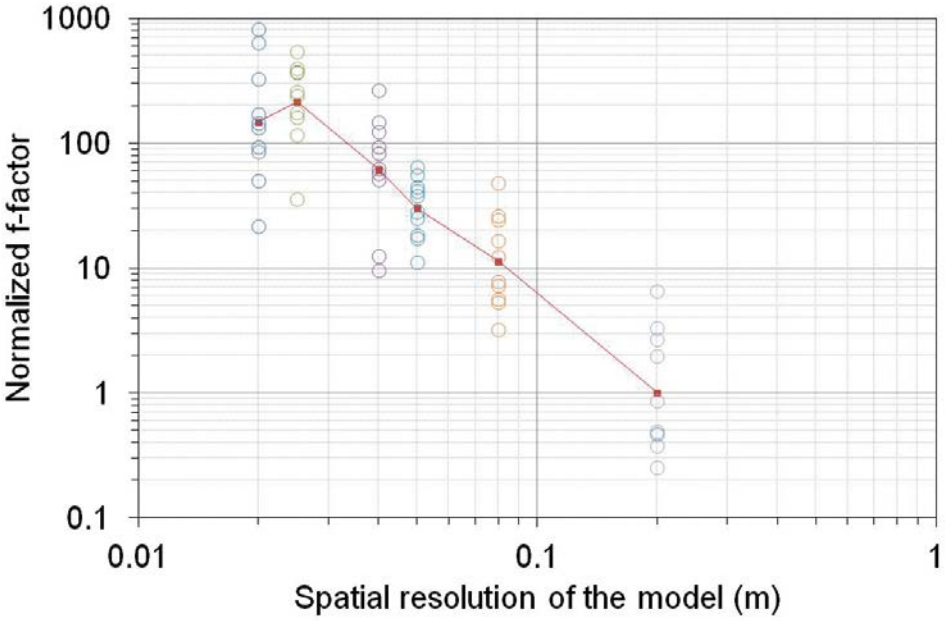

Figure 3-87. *Normalized f-factor through target fracture around KU. Open circle shows the results from ten realizations, and solid circle is an average value.*

4 Discussion and conclusions

4.1 Discussion of results

4.1.1 Task 7A

Task 7A has provided a very good platform for exploring important issues about the use of open holes and PFL to reduce uncertainty of site characterization, and the effect of this reduced uncertainty on the ability to assess safety. Although only a limited series of relatively simple simulations were carried out, the results indicate the following significant findings.

1. Implementation of assumed boundary conditions (including skin to represent the Baltic Sea floor and the fresh-saltwater interface) can have very significant effects on all aspects of flow and transport modelling, and needs to be considered carefully when deriving or calibrating material properties or interpreting sensitivity studies.
2. Within the limitations of the assumed hydrostructural model and boundary conditions, head measurements provided a significant constraint, which made it possible to derive a favoured case (T4) for fault transmissivities
3. Open holes significantly reduced the variability of the head distribution within the rock mass due to short-circuiting the heads. This makes it harder rather than easier to constrain the hydrostructural model.
4. In this study, due to the relatively larger scale of the model region, homogenised faults model and a surface layer continuum model, PFL results themselves did not appear to be particularly sensitive discriminators between the different case studies. In other words, the specified model scale might be relatively larger than PFL data resolutions, which shows heterogeneous inflow and outflow along the boreholes. It might be better to model at the more detailed scale of heterogeneity in the target area around KR24, using a nested coarser outer region to represent the boundary conditions.
5. Travel times and distances can be significantly influenced by transport path geometry, which is in turn controlled by the hydrostructural model, boundary conditions, and assigned material properties. For two of the three release points considered, a detailed knowledge of fault properties would significantly reduce uncertainty and variability of travel distance and/or travel time.
6. More study is needed to evaluate the applicability of these conclusions beyond the limited set of simulations and measures studied. In particular, it would be useful to evaluate whether the levels of uncertainty achieved in the study PA01 actually correspond to a significant effect in repository safety assessment.

4.1.2 Task 7B

One of the reasons that Task 7B was challenging is because PFL logs are strongly influenced both by borehole scale heterogeneities and by the larger scale connectivity and hydrogeologic boundary conditions of the hydrostructural model. Important lessons from Task 7B include the following:

1. The larger structures' hydrostructural model was the most important issue to understand to match pressure and flow responses from hydraulic interference tests. Development of an accurate and defensible hydrostructural model of larger structures (Major Water Conducting Features) should be a high priority. Derivative plot analysis of pressure interference tests is a very useful tool to conceptualise the major water-conducting features.
2. Based on the conceptualisation of major water-conducting features by the derivative plot analysis, it was possible to match the majority of pressure and flow responses based on effective fracture hydrogeologic properties, using a single, isotropic value of transmissivity per fracture, except for the minor flowing features.
3. In order to model minor flowing features, it is important to define the properties of the background fracture population from a dataset from which the larger structures have been removed. If possible, site investigation is also required to discriminate the effects of major water-conducting features when testing at minor zones.

4. Effective fracture hydrogeologic properties are sufficient for hydraulic interference tests; however, heterogeneous connectivity of minor flowing features and/or in-plane heterogeneity of the larger structures needs to be modelled with greater accuracy to match the minor flow responses measured by PFL.
5. There is a need to develop improved measures for comparing complex, heterogeneously connected fractured rock mass models to interference test results. The residual sum of squared errors was proposed as one of the performance indices; however, this single measure is not sufficient to fully understand the differences between models and measurements.

4.1.3 Task 7C

Task 7C aimed to model in-plane heterogeneous aperture distribution in a single fracture intersected by the shaft, based on data obtained at the pilot boreholes drilled before shaft excavation and fracture mapping at the excavated shaft walls. The key messages obtained from this challenging task examination are listed below:

1. The dataset provided was not enough to represent heterogeneous aperture distribution as shown in the existing studies (e.g., Winberg et al. 2003, Tetsu and Sawada 2010) which shows complex fracture surface topography and aperture distribution formed by the specific geological structures.
2. Multiple-scale nested variogram model was proposed, which might require an approach for investigating nested parameters, focusing on the characteristic geological structures, such as slickenside, slicken-step, fracture branch, fracture intersection etc.
3. Even though Task 7C used a multi-scale nested variogram model which was not supported by the dataset provided, most realizations produced results similar to measured values. The measurements that were not well reproduced were responses in PP124 and PP126. One possible explanation for the predictive power of the model despite these limitations is the constraining power of the point measurement from PP borehole PFL measurements, and the histogram aperture distribution derived from Nappy tests at KU2.
4. Simulations of PP124 and PP126 did not cluster near measured values. However, they could be calibrated by increasing transmissivity near boreholes, to increase the flow rate.
5. In addition, upscaling methodologies might be required for the multi-scale nested modelling approach, to make linkages between the millimetre-scale spatial resolution of the aperture distribution model and the model-applied scale. These methodologies should focus on representative transmissivity, aperture, f-factor, etc.
6. Task 7C included a simple examination to study the sensitivity spatial resolution of aperture distribution on representative transmissivity and f-factor. The results show that transport behaviour was fully affected by the spatial resolution of heterogonous aperture distribution.

4.2 Main conclusions

Task 7 has been very useful for advancing the concept of hydrostructural modelling, and in improving the understanding of the ability of hydraulic data to condition key hydrostructural features at each modelling scale. The key hydraulic data identified included the series of the PFL logs tests, during both steady state and transient (pumping interference tests) phases. Major conclusions of this study are as follows:

- Task 7A: Uncertainty of transmissivity values at the regional scale (several kilometres) of fault zones were examined by comparing these values with steady state PFL data and pressure/flow response during pumping phase. The results indicate that the major response can be reproduced by constrained by PFL data, although the opening borehole for measuring PFL has the significant disadvantage that it homogenises head values along the borehole. In order to constrain both major fault zones and minor water conducting features, an advanced method might be required that discriminates between the major pressure or flow response zone and other minor zones during the PFL investigations. This discrimination should be consistent with conceptualisation of the hydrogeological model of major fault zones at the study area.

- Task 7B: Major pressure and flow response could be reproduced by conceptualising major water-conducting features (e.g., fault zones at the several hundred metres scale) based on the derivative plot analysis of transient pressure interference test data. The unified value, RSS, for evaluating model plausibility in the comparison between measured and simulated values could be useful for checking whether major flowing zones (pressure and flow respond zone) can be reproduced, but the RSS will be limited in reproducing minor zone flow behaviour.
- Task 7C: The model of in-plane heterogeneous fracture roughness structure was examined by comparing with flow response measured by PFL at the pilot boreholes drilled along shaft walls before excavating the shafts. Average transmissivity evaluated by standard PFL data could constrain flow behaviour to reproduce most of PFL flow response data measured at pilot boreholes. However, PFL flow response data could not fully constrain small-scale structure in a single fracture affected by various scales of geological structures, varying from several millimetres to several metres. The small-scale structure might strongly control transport behaviour in a fracture, judging from a sensitivity study that varied spatial resolution of heterogeneous models in a single fracture.

4.3 Main assumptions and simplifications

- Task 7A: Homogenised tessellated planer models for the regional scale of major fault zones is assumed to reproduce major pressure and flow responses during the long-term pumping test. The surface layer is assumed to be homogeneous equivalent porous medium to contribute to the interface between precipitation and groundwater recharge.
- Task 7B: Transient pressure interference test data are available to map major water flowing features around the test area. In addition, the background fracture network structure estimated by hydrogeological data of water-conducting fractures measured by PFL, is assumed to be well connected. “Anti-fracture” conceptualisation is applied to calibrate the heterogeneous flow behaviour of the background fracture network.
- Task 7C: The multiple-scale nested model is assumed to represent a single fracture in-plane heterogeneity model, constructed by the various scales of geological structures, varying from scales of several millimetres to several metres.

4.4 Evaluation of conceptual models and modelling approach

- The hybrid DFN/EPM conceptual model was able to provide a good match at island/ repository scale.
- The background fracture approach needs refinement, particularly as evidenced by the over-connected background fracture models of Task 7B. One approach to address this could be to improve fracture intersection and in-plane roughness/heterogeneity models.
- Models for localization of flow to shafts worked well with the multi-scale conditioned approach. However, there are not sufficient site characterization data to justify the wide use of this approach.

4.5 Lessons learned and implications for Task 7 objectives

- Framework objectives to advance integration of fractured rock site characterization and modelling to support a safety assessment have been met, primarily through advances in technical approaches and in demonstration of need for additional research and characterization on fracture roughness scales.
- The major objective regarding open boreholes and PFL was met to a limited extent, since PFL log data were not found to be significantly more powerful than cross-hole hydraulic testing for constraining the hydrostructural model.

4.5.1 Influence of open boreholes

- Modelling of hydraulic tests shows that open boreholes can be the most significant hydraulic feature in the model, potentially reducing the resolution of characterization of hydrostructural model features.
- The hybrid DFN/EPM modelling approach was nevertheless able to constrain the hydraulic properties of these features, through a simple manual optimization approach.
- Concerns remain about geochemical cross-contamination due to open boreholes.

4.5.2 The use of PFL measurements to reduce uncertainty in models

- Single hole PFL measurements were very useful for deriving background fracture transmissivity distributions.
- The value of these distributions is limited where the resulting DFN model is over-connected.
- PFL measurements were very useful to help constrain the location and properties of deterministic elements of the hydrostructural model.
- Cross-hole PFL measurements were not as useful as had been hoped for constraining local in-plane fracture properties and heterogeneity.

4.5.3 Integrated view of Task 7

- The PFL is very useful for studying background fracture transmissivity, and constraining structural feature intersections with boreholes.
- Cross-hole PFL and PFL interference methods are potentially useful, but were less easy to use to constrain models.

References

SKB's (Svensk Kärnbränslehantering AB) publications can be found at www.skb.se/publications.

Bear J, 1972. Dynamics of fluids in porous media. New York: Elsevier.

Dershowitz, W, Doe T, Uchida U, Hermanson J, 2003. Correlations between fracture size, transmissivity, and aperture. In Culligan P, Einstein H, Whittle A (eds). Soil Rock America: Proceedings of the 39th US Rock Mechanics Symposium. VGE, Essen, 887–891.

Dershowitz W, Lee G, Josephson N, 2007. FracMan interactive discrete feature data analysis, geometric modeling,and exploration simulation. User Documentation, Version 7. Seattle: Golder Associates Inc.

Doe T W, 2002. Äspö Hard Rock Laboratory. TRUE Block Scale Project. Generalized dimension analysis of build-up and pressure interference tests. SKB IPR-02-70, Svensk Kärnbränslehantering AB.

Enachescu C, Frieg B, Wozniewicz J, 2004. A new visual synthesis tool for transient test data. In State of the science and measuring success in remediation: Proceedings U.S. EPA/NGWA Fractured Rock Conference, Portland, Maine, 13–15 September 2004, 173–184.

Hakami E, 1995. Aperture distribution of rock fractures. PhD thesis, Royal Institute of Technology, Division of Engineering Geology, Stockholm.

Hodgkinson D, 2007. Äspö Task Force on modelling of groundwater flow and transport of solutes, Review of Tasks 6D, 6E, 6F and 6F2, SKB TR-07-03, Svensk Kärnbränslehantering AB.

Klockars J, Vaittinen T, Ahokas H, 2006. Hydraulic crosshole interference tests at Olkiluoto, Eurajoki in 2004, boreholes KR14–KR18 and KR15B–KR18B. Posiva Working Report 2006-01, Posiva Oy, Finland.

Mazurek M, Lanyon W, Vomvoris S, Gautschi A, 1998. Derivation and application of a geologic dataset for flow modelling by discrete fracture networks in low-permeability argillaceous rocks. Journal of Contaminant Hydrology 35, 1–17.

Miller I, Lee G, Dershowitz W, 2001. MAFIC, Matrix / fracture interaction code with head and solute transport, User documentation, version 2.0, Redmond, WA: Golder Associates Inc.

Murata S, 2001. Characterization of the mechanical and hydrological properties of a rock joint by using a fractal model. PhD thesis. Kyoto University.

Remy N, Boucher A, Wu J, 2009. Applied geostatistics with SGeMS: a user's guide. Cambridge: Cambridge University Press.

Sato H, Sawada A, 2010. Measurement of a single fracture with heterogeneous aperture distribution by optical method and evaluation of flow characteristics. Doboku Gakkai Ronbushuu C 66, 487–497. (In Japanese.)

Sawada A, Sato H, 2010. A study of hydraulic properties in a single fracture with in-plane heterogeneity: an evaluation using optical measurements of a transparent replica. Nuclear Engineering and Technology 42, 9–16.

Sawada A, Uchida M, Shimo M, Yamamoto H, Takahara H, Doe T W, 2000. Non-sorbing tracer migration experiments in fractured rock at the Kamaishi Mine, Northeast Japan. Engineering Geology, 56, 75–96.

SKB, 2011. Long-term safety for the final repository for spent nuclear fuel at Forsmark, Main report of the SR-Site project. SKB TR-11-01, Svensk Kärnbränslehantering AB.

Tetsu K, Sawada A, 2010. Study of natural fracture topography and fracture aperture distribution in 50 cm scale granitic rock block measured by a precision grinder. JAEA-Research 2010-041, Japan Atomic Energy Agency. (In Japanese.)

Uchida M, Doe T, Dershowitz W, Thomas A, Wallmann P, Sawada A, 1994. Discrete-fracture modelling of the Äspö LPT-2. Large scale pumping and tracer test. SKB ICR-94-09, Svensk Kärnbränslehantering AB.

Vaittinen T, Ahokas H, 2005. Long-term pumping test in borehole KR24 and pressure observations at Olkiluoto, Eurajoki in 2004. Posiva Working Report 2005-40, Posiva Oy, Finland.

Vidstrand P, Ahokas H, Bockgård N, Dershowitz W, Holton D, Lanyon W, Poteri A, Koskinen L, 2012. Task Force GWFTS – Task 7. Descriptions for hydrogeological modelling of Olkiluoto, Finland. Compilation of all task descriptions assessed within the Task 7 of the SKB Task Force on modelling of groundwater flow and transport of solutes. SKB P-12-21, Svensk Kärnbränslehantering AB.

Wang X, 2005. Stereological interpretation of rock fracture traces on borehole walls and other cylindrical surfaces. PhD thesis. Virginia Polytechnic Institute and State University.

Winberg A, Andersson P, Byegård J, Poteri A, Cvetkovic V, Dershowitz B, Doe T, Hermanson J, Gómez-Hernández J J, Hautojärvi A, Billaux D, Tullborg E-L, Holton D, Meier P, Medina A, 2003. Final report of the TRUE Block Scale Project. 4. Synthesis of flow, transport and retention in the block scale. SKB TR-02-16, Svensk Kärnbränslehantering AB.

Öhberg A, Rouhiainen P, 2000. Posiva groundwater flow measuring techniques. Posiva 2000-12, Posiva Oy, Finland.